UNIVERSITA' DEGLI STUDI DI PADOVA

DIPARTIMENTO DI SCIENZE CHIMICHE

CORSO DI LAUREA MAGISTRALE IN CHIMICA

TESI DI LAUREA MAGISTRALE

Design, preparation, and optical characterization of plexcitonic nanohybrids based on gold nanorods and J-aggregates of organic dyes

Relatore: Prof.ssa Elisabetta Collini

Controrelatore: Prof. Andrea Tapparo

Laureando: Federico Toffoletti

ANNO ACCADEMICO 2021/2022

Index

Abstract

Nanomaterials able to efficiently promote strong light-matter coupling have long been investigated due to their potential disruptive applications. In fact, systems characterized by hybrid light-matter electronic states promise to unlock an unprecedented capability of directing the migration of excitation energy at the nanoscale, offering exciting prospects in the field of nanophotonics, quantum technologies, light-harvesting, and all those photonic applications that require strict control over the flow of energy in time and space. So far, the strong coupling between light and matter has been mainly promoted through optical cavities. While these systems now offer an efficient way of generating hybrid light-matter states, their preparation requires tedious and long procedures. The colloidal plexcitonic nanohybrids investigated in this Thesis represent an exciting, yet underexplored, alternative. Plexcitonic nanohybrids, a class of light-matter coupled nanosystems, are nanosystems characterized by strong plasmon-exciton couplings. They can be prepared by promoting the self-assembly of molecular J-aggregates on the surface of plasmonic colloidal nanoparticles (acting as nanocavities) under suitable experimental conditions. In this work, we synthesized and investigated the optical properties of different nanohybrids based on gold nanorods functionalized with J-aggregates of various molecules (cyanines and porphyrins). The linear optical properties have been characterized by UV-Vis absorption spectroscopy, which allowed the optimization of the experimental conditions necessary to achieve a strong coupling. Inspired by recent literature works, we also explored the optical activity of the nanosystems by circular dichroism, unveiling exciting and highly promising properties. Finally, the ultrafast relaxation dynamics of plexciton states were characterized by pump-probe spectroscopy, which highlighted the presence of complex and unexpected relaxation mechanisms involving energy redistribution among bright plexciton states and dark states.

List of abbreviations

CD	Circular Dichroism
CE	Condition of Existence (of polaritons)
CTAB	Cetyl Trimethyl Ammonium Bromide
DOS	Density Of States
DS	Dark State
ESA	Excited State Absorption
FWHM	Full Width at Half Maximum
GSB	Ground State Bleaching
JC	Jaynes–Cummings
JC-1	5,5′,6,6′-Tetrachloro-1,1′,3,3′-tetraethylbenzimidazolocarbocyanine iodide
LM	Longitudinal Mode (plasmon)
LP	Lower Polariton
LSP	Localized Surface Plasmon
NP	Nanoparticle
NR	Nanorod
PIC	Pseudoisocyanine (1,1'diethyl-2,2'-cyanine iodide)
QE	Quantum Emitter
RDD	Raise-Decay-Decay
SC	Strong Coupling
SE	Stimulated Emission
TA	Transient Absorption
TC	Tavis-Cummings
TEM	Transmission Electron Microscopy
TM	Transverse Mode (plasmon)
TPPS	5,10,15,20-tetrakis(4-sulfonatophenyl)porphyrin
UP	Upper Polariton

Introduction

Until the beginning of the 20th century, light and matter were treated as different entities with their own properties. The development of quantum mechanics has enabled the theoretical description of the interaction between light and matter down to subtle microscopic details. Then, in the last century, numerous phenomena originating from this interaction have been revealed. It was demonstrated that it is possible to modify the chemical and physical properties of molecules, not only through chemical modifications but also by coupling molecules with light.[1] In fact, depending on the coupling strength, one may run into the enhancement of the relaxation rate of the excited states of the matter,[2] the interference between light and matter states, or the generation of new hybrid states called polaritons.[3–5] In a general view, polaritons originate from the strong coupling between a cavity (a device in which the electromagnetic field is confined and enhanced) and a quantum emitter (which provides the matter states). The strong coupling regime is reached when the rate of coherent energy exchange between the cavity and the quantum emitter is faster than their decay rates. Because of the massive number of possible phenomena, the materials involved in the strong light-matter coupling have been indicated as highly promising in numerous technological fields such as solar cells,[6] low threshold lasers and parametric amplifier production,[7] sensing,[8] imaging,[9] quantum technologies,[10] chiral species sensing,[11] and others.

The definition of clear structure-to-properties relationships in these materials is thus of crucial importance for the realization of a new generation of smart functional devices. For this purpose, in recent years, we are seeing an ever-growing increase of the interest in using organic excitons and metallic nanostructures. Organic excitons, due to their large transition dipoles and low losses, provide large coupling strength, allowing the possibility of exploring the effects of strong coupling on the physical and chemical properties of organic molecules at room temperature. On the other hand, plasmonic nanoparticles are well-known systems capable of confining and enhancing the electromagnetic field on their surface, with an easily tunable plasmonic resonance.[12,13] Materials prepared by the assembly of plasmonic nanoparticles and molecules, or aggregates of molecules, are known as colloidal plexcitonic materials. The electronic properties of these nanohybrids are ruled by the presence of plexcitons, a particular

class of polariton states arising from the plasmon-exciton coupling.[5,7] Plexcitonic nanosystems have the significant advantage of being extremely easy and cheap to prepare.

Furthermore, plexcitonic systems promise a high control over the final optical properties, even at the nanoscale, because of the several chemical parameters that can be independently changed during their preparation. For example, different coupling strengths can be reached by adding different quantities of organic dye. Also, acting on the frequency of the plasmon, different matter states can be selected to couple with light. Obviously, strict control over the final properties, which plexcitonic nanosystems promise to unlock, is needed to engineer materials with the desired functionality. However, despite these promising prerogatives, the fundamental aspects of their design, as well as the knowledge of their dynamics and, mostly, the understanding of the relationships that exist between structure and dynamics are still scarce. Therefore, great experimental efforts on these nanosystems still must be made.

This Thesis fits precisely in this context and is focused in particular on the study of the photophysical and dynamic properties of plexcitonic materials. The theoretical basis of strong light-matter coupling can be used as the first approach for describing plexcitons. Therefore, the first part of this Thesis consists of a study of the fundamental theoretical aspects of polaritons. We start with the easy model of a single quantum emitter interacting with a cavity, including the conditions necessary to obtain hybrid states, and go towards ever more complex systems, which approach the plexcitonic nanosystems. Secondly, the analysis continues with the assembly of nanohybrids. This task requires identifying the metallic nanoparticles and organic dyes with the most suitable properties to fulfill the strong coupling conditions. For this purpose, we selected two classes of suitable dyes, porphyrins and cyanines, and synthesized gold nanorods with plasmons resonant to the J-band of the aggregated dyes.

Driven by the high interest that a porphyrin-based plexciton have, we first explored several supramolecular conditions to get a strong coupling between gold nanorods and tetra-sulfonato-phenyl porphyrin molecules. Secondly, we moved our attention to cyanines, particularly PIC and JC-1. Overall, it was possible to establish strong plasmon-exciton coupling with both cyanines. Furthermore, a more complex system, where JC-1 and PIC participate together in the same plexcitonic system, was obtained. The reason that led us to make a more complex mixed systems was to demonstrate if and to what extent it is possible to tune optical and dynamic properties acting on the nature of the dyes employed.

Finally, the optical and photophysical properties of the final plexcitonic nanosystems were characterized, with particular attention to the mixed system. Further in-depth studies are required to confirm these preliminary results, but the topic has been revealed to be particularly interesting and full of potential developments.

This Thesis is organized as follows. In the first Chapter, the theoretical aspects of strong light-matter interaction in cavities were explored. Then, in the second Chapter, the experimental methods used to prepare the plexcitonic nanosystems and the techniques employed to characterize their optical properties are described. Finally, in the third Chapter, all the experimental results and their discussion are systematically reported. We then conclude with a summary of the main findings and a comment on future perspectives.

Chapter 1
Fundamental principles

1.1 Description of light-matter interaction in cavities

The photophysical properties of matter significantly change when the matter is placed within optical cavities. Indeed, it is possible to couple "Quantum Emitters" (QEs), such as molecules, aggregates or inorganic excitonic materials, with "cavities", i.e., materials that enhance the field of the light. When the matter states are in resonance with the enhanced electromagnetic field of interacting radiations, coupling interactions can be established, which strongly affect the electronic and optical properties of the system.[1,3,4,14]

Depending on the coupling strength, different regimes and phenomena can occur.[15] Generally speaking, in the weak coupling regime the interaction with light can be considered as a perturbation of the material system, therefore, this interaction promotes the energy exchange between the states without significantly changing them. This energy exchange between weakly coupled light and matter states is incoherent and typically leads to an enhancement of the luminescence of the QEs. This phenomenon, also known as Purcell effect, can be explained by an increased density of states available to the emitted photon.[2] Instead, in the strong coupling (SC) regime, the energy exchange occurs faster than any other relaxation process, thus, back-and-forth oscillations of the excitation energy are established. In such a situation, the light and the matter states are mixed and give rise to two new hybrid states, called Upper and Lower Polaritons (UP and LP, respectively), with an energy separation proportional to the coupling strength. The frequency splitting of these states is called Rabi splitting Ω_{R} and it corresponds to the frequency of the energy exchange.[3,4,15,16]

This section aims to give a theoretical description of light-matter interaction in the SC regime.

1.1.1 Strong coupling between light and matter: a quantum description

In the simplest picture, the SC effect can be illustrated using a model of two coupled harmonic oscillators capable of exchanging energy. However, the effect of the hybridization of light–matter states and the corresponding splitting can be demonstrated using classical, semiclassical, or quantum approaches, as described in detail in ref [5]. The fully quantum approach for the simplest system consisting of a single emitter placed in a cavity is based on the Jaynes–Cummings model (JC).[3,5,17] In this case, the QE is treated as a two-level system with the ground $|g\rangle$ and excited $|e\rangle$ energy states separated by the transition energy $\hbar\omega_{\mathrm{QE}}$, with $\hbar$ being the reduced Planck constant. The Hamiltonian of such an emitter is:

$$\widehat{\mathcal{H}}_{QE} = \hbar\omega_{QE}\hat{\sigma}^{\dagger}\hat{\sigma} \tag{1.1}$$

with $\hat{\sigma} = |g\rangle\langle e|$ and $\hat{\sigma}^{\dagger} = |e\rangle\langle g|$ being the lowering and the raising operator, respectively. The QE is characterized by a transition dipole moment:

$$\boldsymbol{\mu}_{eg} = \langle g|q\hat{\boldsymbol{r}}|e\rangle \tag{1.2}$$

with q being the elementary charge. The single-mode cavity is described by the standard Hamiltonian:

$$\widehat{\mathcal{H}}_{c} = \hbar\omega_{c}\hat{a}^{\dagger}\hat{a} \tag{1.3}$$

with ω_c being the cavity mode frequency, $\hat{a}$ and $\hat{a}^{\dagger}$ the photon annihilation and photon creation operator, respectively. The emitter-cavity interaction is mediated via the electric dipole term:

$$\widehat{\mathcal{H}}_{int} = \widehat{\boldsymbol{\mu}} \cdot \widehat{\boldsymbol{E}}\left(\boldsymbol{r}_{QE}\right) \tag{1.4}$$

with $\widehat{\boldsymbol{\mu}}$ the QE dipole moment operator:

$$\widehat{\boldsymbol{\mu}} = \boldsymbol{\mu}_{eg}(\hat{\sigma}^{\dagger} + \hat{\sigma}) \tag{1.5}$$

$\widehat{\boldsymbol{E}}$ the electric field operator at the position of the QE:

$$\widehat{\boldsymbol{E}}\left(\boldsymbol{r}_{QE}\right) = \mathcal{E}(\hat{a}^{\dagger} + \hat{a}) \tag{1.6}$$

and $\mathcal{E}$ the vacuum electric field. Since

$$\widehat{\boldsymbol{\mu}}(t) \sim (e^{i\omega_{QE}t} + e^{-i\omega_{QE}t}); \tag{1.7a}$$

$$\widehat{\boldsymbol{E}}(t) \sim (e^{i\omega_c t} + e^{-i\omega_c t}); \tag{1.7b}$$

the product of both has terms oscillating with frequency $\omega_{\mathrm{QE}} - \omega_c$ and $\omega_{\mathrm{QE}} + \omega_c$. The terms oscillating with the difference frequency are those proportional to (i) $\hat{\sigma}^\dagger \hat{a}$ and (ii) $\hat{\sigma}\hat{a}^\dagger$. They describe (i) the molecular excitation by the absorption of a cavity photon and (ii) the molecular relaxation by the emission of a cavity photon. Thus, they conserve the number of excitation quanta in the system.[18] Instead, the terms oscillating with the sum frequency are those proportional to (iii) $\hat{a}^\dagger \hat{\sigma}^\dagger$ and (iv) $\hat{a}\hat{\sigma}$, which are related to the simultaneous (iii) creation and (iv) destruction of a molecular excitation and a photon.[18] If the spectral detuning between the cavity mode and the emitter, defined as:

$$\delta = \omega_{QE} - \omega_c \tag{1.8}$$

is small, the oscillations of $\widehat{\mathcal{H}}_{\mathrm{int}}$ with the sum frequency are on a much faster time scale, therefore they average to zero within an oscillation period of the difference frequency. Thus, under this circumstance, we can skip the counter-rotating terms $\hat{a}\hat{\sigma}$ and $\hat{a}^\dagger \hat{\sigma}^\dagger$. That is called the rotating wave approximation (RWA).[19] The resulting Hamiltonian in the JC model became:[3]

$$\widehat{\mathcal{H}}_{JC} = \hbar\omega_0 \hat{\sigma}^\dagger \hat{\sigma} + \hbar\omega_c \hat{a}^\dagger \hat{a} + \hbar g(\hat{\sigma}\hat{a}^\dagger + \hat{\sigma}^\dagger \hat{a}) \tag{1.9}$$

with g the coupling constant:

$$g = -\boldsymbol{\mu}_{eg}\mathcal{E}/\hbar \tag{1.10}$$

In the absence of coupling, $g = 0$, the eigenstates of the systems are the direct product of the QE eigenstates $|g\rangle, |e\rangle$ and the cavity Fock states $|n\rangle$, where n indicates the number of photons in the cavity $\{|g,n\rangle, |e,n\rangle\}$. By neglecting the counter-rotating terms in the interaction Hamiltonian, the total number of particles is conserved. Therefore, the light-matter Hamiltonian couples only states with the same number of excitations (either QE or photonic excitations), generating new eigenstates from their superposition. From this it can be immediately inferred that the global ground state is the state with no excitation, i.e., the state with the QE in the ground state and no cavity photons $|g,0\rangle$, and that it is not affected in the JC picture of interaction. Moreover, the "one-particle" excited states rise from the superposition of states with one excitation, which are (i) the state with the QE in the excited

state and no cavity photons $|e,0\rangle$, and (ii) the state with a single photon and no QE excitation $|g,1\rangle$. Analogously, it is possible to define "two-particle" and more in general "n-particle" states. For the moment we will consider only one-particle states, which are the most accessible states in conventional experiments. However, some non-linear phenomena observed in this Thesis will require invoking two-particle states, which will be introduced later in section 1.1.5.

Thus, using $\{|e,0\rangle, |g,1\rangle\}$ as base vectors, the diagonalization of the Hamiltonian (eq. 1.9) leads to the formation of two new eigenstates $|1,-\rangle$ and $|1,+\rangle$, called Lower Polariton (LP) and Upper Polariton (UP), respectively (figure 1.1). The new eigenfrequencies are:

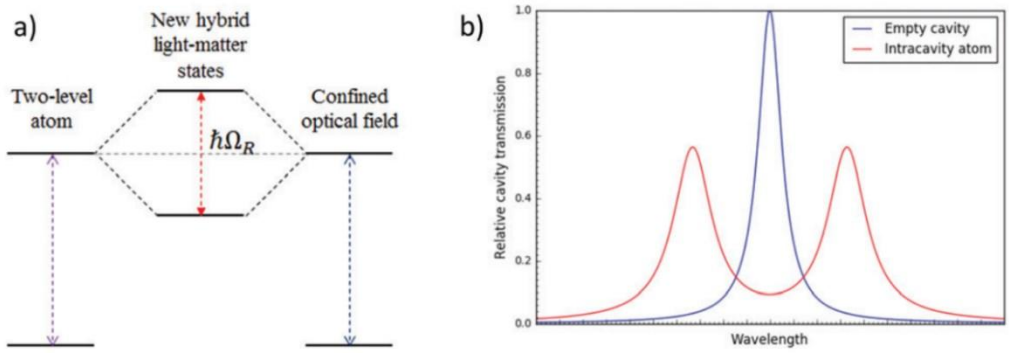

Figure 1.1 *a) The resonance interaction between a two-level atom (a QE) and a confined electromagnetic field (a cavity), resulting in two new hybrid states separated by the Rabi splitting energy $\hbar\Omega_R$. b) The red curve is the double-peaked transmission spectrum due to the splitting in the energy eigenstates. The blue curve is the relative transmission of a probe through an empty cavity. Reproduced from ref [4].*

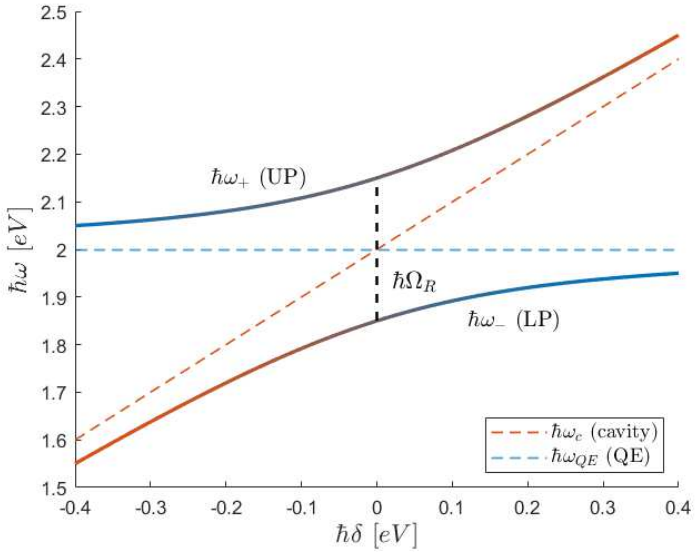

Figure 1.2 *Graphic representation of the "anticrossing" behavior of polaritonic states. The dotted lines represent the uncoupled system energies. The solid lines represent the UP and LP states energies, calculated from eq. 1.11, as a function of the energetic detuning.*

$$\omega_{\pm} = \frac{\omega_{QE} + \omega_c}{2} \pm \sqrt{\frac{\delta^2}{4} + g^2}. \tag{1.11}$$

In figure 1.2, the new eigenenergies are plotted as a function of $\hbar\delta$. The more $\hbar\delta$ is reduced, the more $\hbar\omega_+$ and $\hbar\omega_-$ move away from the energies of the uncoupled systems. This is the so called "anticrossing" behavior, which is typical for strongly coupled systems.

To write the eigenstates, we denote:

$$\sin(\theta_0) = \frac{2g}{\sqrt{(R_0 - \delta)^2 + 4g^2}}; \tag{1.12a}$$

$$\cos(\theta_0) = \frac{R_0 - \delta}{\sqrt{(R_0 - \delta)^2 + 4g^2}}; \tag{1.12b}$$

$$R_0 = \sqrt{\delta^2 + 4g^2}; \tag{1.12c}$$

with these definitions, the eigenstates are:

$$|1, -\rangle = \cos(\theta_0)\,|g, 1\rangle - \sin(\theta_0)\,|e, 0\rangle; \tag{1.13a}$$

$$|1, +\rangle = \sin(\theta_0)\,|g, 1\rangle + \cos(\theta_0)|e, 0\rangle; \tag{1.13b}$$

or inversely:

$$|g, 1\rangle = \cos(\theta_0)\,|1, -\rangle + \sin(\theta_0)\,|1, +\rangle; \tag{1.13c}$$

$$|e, 0\rangle = -\sin(\theta_0)\,|1, -\rangle + \cos(\theta_0)|1, +\rangle; \tag{1.13d}$$

Thus, the new eigenstates are a superposition of the initial states. In other words, treating the cavity and the QE independently is no longer possible, and $|1, -\rangle$, $|1, +\rangle$ became new states with new properties.

In the special case of $\delta = 0$, i.e., in resonance conditions, it is verified that:

$$|1, \pm\rangle = \frac{|g, 1\rangle \pm |e, 0\rangle}{\sqrt{2}}; \tag{1.14a}$$

$$\omega_{\pm} = \frac{\omega_c + \omega_{QE}}{2} \pm g; \tag{1.14b}$$

and the energy difference between the new eigenstates is called Rabi splitting:

$$\Omega_R = 2g \tag{1.15}$$

Let us now look at the temporal behavior of a coupled system. In the Schrödinger picture, the temporal evolution is recovered from $|\Psi(t)\rangle = e^{-\hat{\mathcal{H}}t/\hbar}|\Psi(0)\rangle$. Let us assume the cavity to be initially excited and the emitter to be in the ground state; this writes as:

$$|\Psi(0)\rangle = |g,1\rangle = \frac{|1,-\rangle + |1,+\rangle}{\sqrt{2}} \tag{1.16}$$

Thus, after a time t, the state has evolved to:[5]

$$|\Psi(t)\rangle = \frac{e^{-i\omega_- t}|1,-\rangle + e^{-\omega_+ t}|1,+\rangle}{\sqrt{2}}$$

$$= \cos(\Omega_R t/2)\,|g,1\rangle - i\sin(\Omega_R t/2)\,|e,0\rangle \tag{1.17}$$

This allows calculating directly the probability $P_e(t)$ to find the QE in the excited state $|e\rangle$, and the probability $P_g(t)$ to find the photon in the cavity:

$$P_e(t) = |\langle e,0|\Psi(t)\rangle|^2 = \frac{1-\cos(\Omega_R t)}{2}; \tag{1.18a}$$

$$P_g(t) = |\langle g,1|\Psi(t)\rangle|^2 = \frac{1+\cos(\Omega_R t)}{2}; \tag{1.18b}$$

From these results, plotted in figure 1.3a, it is clear that the cavity and the QE exchange the photon (coherence) with a frequency that is exactly the Rabi splitting frequency.

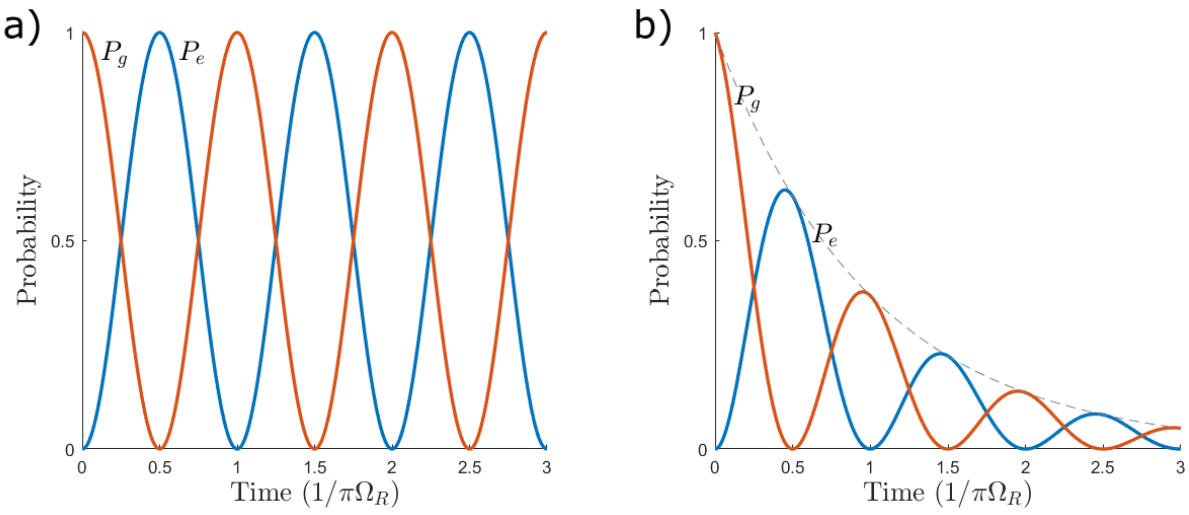

Figure 1.3 *Time evolution of the occupation probability P_g of the emitters' ground (orange line) and P_e excited (blue line) state. Both probabilities show Rabi oscillations at frequency Ω_R. In panel a) and b) the time evolutions are calculated from eq. 1.18 without considering damping effects and introducing an extra exponential decay, respectively.*

However, the Rabi splitting can be blurred out by spontaneous decay and dephasing in the system. In order to describe the crossover between the two scenarios, we need to introduce losses associated with incoherent processes. This can be done phenomenologically by introducing complex energies of the QE, $\omega_{QE} - i\gamma$, and the cavity, $\omega_c - ik$. The resulting eigenfrequencies in the single excitation subspace, $n = 1$, may be found by diagonalizing the following non-Hermitian Hamiltonian:[3]

$$\mathcal{H}_{loss} = \begin{pmatrix} \omega_{QE} - i\gamma & g \\ g & \omega_c - ik \end{pmatrix} \tag{1.19}$$

where γ and k are the phenomenologically QE and cavity dissipation rates, resulting in 2γ and $2k$ full widths at half-maximum of the QE and the cavity extinction spectra. The complex eigenfrequencies $\omega_{\pm}$ of the diagonalized Hamiltonian (1.19) are:

$$\omega'_{\pm} = \frac{\omega_{QE} + \omega_c}{2} - \frac{i}{2}(\gamma + k) \pm \frac{1}{2}\sqrt{4g^2 + \left(\delta - i(\gamma - k)\right)^2} \tag{1.20}$$

From this equation we calculate the Rabi splitting, i.e., the difference of the two eigenfrequencies in the condition of zero detuning:

$$\Omega_R = \sqrt{4g^2 - (\gamma - k)^2} \tag{1.21}$$

This result is rather different than what was previously stated: Ω_R is no more equal to $2g$ when losses are kept into account. These losses also concur to the dephasing of the coherence, for which equations (1.18a-b) can be rewritten by adding an extra exponential decay which damps the energy exchange until the probability reaches zero (figure 1.3b).

1.1.2 Condition of existence of the polaritons (CE) and strong coupling conditions (SC)

The condition of existence of the polaritons (CE) can be deducted by observing eq. 1.21. The Rabi splitting becomes real-valued only in the condition:

$$2g > |\gamma - k| \tag{1.22a}$$

However, this condition is necessary but not sufficient to reach SC. The new states need to be resolved one from other. This happens when: [1,3,5]

$$\Omega_R > \gamma + k \tag{1.22b}$$

which is the so-called SC condition. When both conditions are fulfilled, the QE and the cavity coherently exchange energy. Otherwise, we are in the intermediate or weak coupling regimes, which will not be treated in this Thesis. Finally, let's look at eq. 1.10, where the coupling strength between a single QE and a cavity is defined by the QE transition dipole moment and the cavity vacuum electric field. The latter can be expressed through the mode volume V_m as:[20–22]

$$\mathcal{E} = \sqrt{\hbar\omega/2\epsilon\epsilon_0 V_m} \tag{1.23}$$

with ϵ_0 the vacuum permittivity. From eq. 1.23 it can be inferred that the mode volume is a central parameter describing the coupling strength, as $g \propto 1/\sqrt{V_m}$. Thus, the smaller the mode volume is, the stronger the coupling.

1.1.3 Strong coupling between a photon cavity and N interacting QEs: dark states

The light-matter coupling can occur not only at the single QE level, but also when many QEs are coupled to the same cavity.[23] Actually, this is the most common experimental case since the effective volume of the cavities, even the smallest ones, is large enough to host more than one QE.[24] In this framework, the Hamiltonian must be generalized to consider all the possible interactions among N QEs and the cavity. The Dicke or Tavis-Cummings (TC) Hamiltonian is thus defined:[18,23,25]

$$\widehat{\mathcal{H}}_{TC} = \hbar\omega_c \hat{a}^\dagger \hat{a} + \hbar \sum_{i=1}^{N} \omega_{QE} \hat{\sigma}_i^\dagger \hat{\sigma}_i + \hbar \sum_{i=1}^{N} g_i (\hat{\sigma}_i^\dagger + \hat{\sigma}_i)(\hat{a}^\dagger + \hat{a}) \tag{1.24}$$

Considering N identical QEs, thus $g_i \equiv g$, and assuming the RWA approximation, the Hamiltonian becomes:

$$\widehat{\mathcal{H}}_{TC} = \hbar\omega_c \hat{a}^\dagger \hat{a} + \hbar \sum_{i=1}^{N} \omega_{QE} \hat{\sigma}_i^\dagger \hat{\sigma}_i + \hbar g \sum_{i=1}^{N} (\hat{\sigma}_i^\dagger \hat{a} + \hat{\sigma}_i \hat{a}^\dagger) \tag{1.25}$$

As seen for the JC model, the total number of excitations remains a constant of motion:[18]

$$\widehat{N}_{exc} = \sum_{i=1}^{N} \hat{\sigma}_i^\dagger \hat{\sigma}_i + \hat{a}^\dagger \hat{a}; \tag{1.26}$$

$$\left[\widehat{\mathcal{H}}_{TC}, \widehat{N}_{exc}\right] = 0 \tag{1.27}$$

thus, TC model only allows hybrid states in which components share the same N_{exc}. For $N_{exc} = 0$ there is only one state that is the global ground state of the system $|g_1, \dots, g_N, 0\rangle = |G, 0\rangle$ and is not affected by the interaction. Then, $N + 1$ basis states with $N_{exc} = 1$ are defined: a single state with all QEs in the ground states and a cavity photon $|g_1, \dots, g_N, 1\rangle = |G, 1\rangle$, and N states where a single QE is excited and no cavity photons $|g_1, \dots, e_i, \dots, g_N, 0\rangle = |e_i, 0\rangle$. The diagonalization of the TC Hamiltonian leads to two bright states, the UP and LP:

$$|1, \pm\rangle = \frac{1}{\sqrt{2}}|G, 1\rangle \pm \frac{1}{\sqrt{2N}} \sum_{i=1}^{N} |e_i, 0\rangle \tag{1.28}$$

where we have assumed resonance conditions. The respective eigenfrequencies are:

$$\omega_\pm = \frac{\omega_c + \omega_{QE}}{2} \pm g\sqrt{N}; \tag{1.29}$$

$$\Omega_R = 2g\sqrt{N} \tag{1.30}$$

Equations 1.29 and 1.30 show that the coupling strength is now increased by a factor $\sqrt{N}$, implying that the excitation is shared among the cavity and all the N coupled QEs. In this situation, the overall coupling strength, and thus the Rabi splitting, strongly depends on N. Putting together equations 1.30 and 1.23, the overall coupling strength results proportional to:

$$g \propto \sqrt{N/V_m} \tag{1.31}$$

Thus, the SC can be increased by reducing the mode volume or by increasing the number of interacting QEs.

In addition to two bright states, the single excitation subspace also gives rise to $N - 1$ "dark states" (DS) of the form:[26,27]

$$|DS\rangle = \sum_{i=1}^{N} c_i |e_i, 0\rangle \quad with \quad \sum_{i=1}^{N} c_i = 0 \tag{1.32}$$

As one can see, these states do not couple to the photonic component, and their energies are identical to the energy of uncoupled QEs. These states are referred as dark states since the transition dipole moment between the global ground state and any of these states is zero. As a result, they cannot be populated by an external photoexcitation. However, because of their high density, DSs can act as a sink of excitation from polaritons, strongly affecting the relaxation dynamics of the coupled system.[18,28]

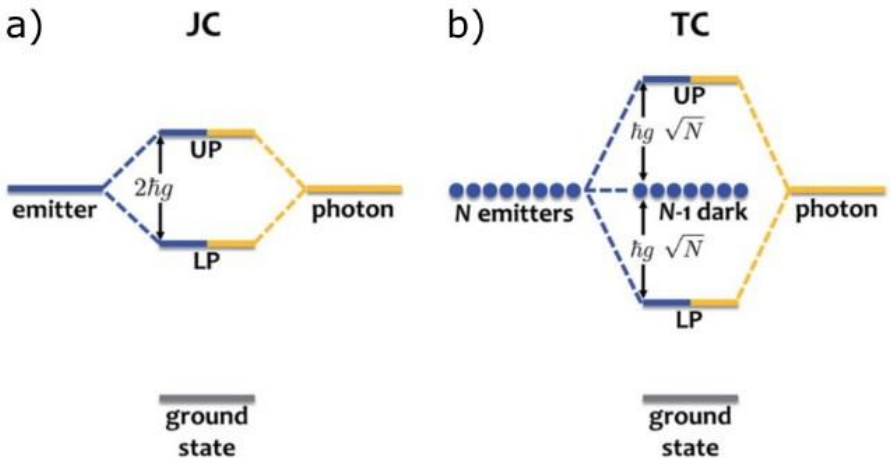

Figure 1.4 *a) Jaynes–Cummings (JC) model: the emitter and the photon strongly couple to form hybridized states, termed lower and upper polaritons, separated in energy by* $2\hbar g$*. b) Tavis–Cummings (TC) model:* N *emitters interact strongly with a photon to yield polaritons (LP, UP) and* $N-1$ *DSs. The latter do not couple to light and thus maintain the original emitter energy. Reproduced from ref* [23].

1.1.4 The role of energetic disorder

The TC model clearly illustrates the remarkable delocalization of polariton states. However, from the theory of molecular excitons it is well-known that energetic disorder can cause the localization of the excited state. Thus, it is of interest to determine how robust polariton states are with respect to disorder. In a recent work, the interplay of disorder and light-matter coupling was explored.[29] It was found that disorder broadens the high density of DSs centered at the energy of the bare QEs (figure 1.5). However, even under relatively high energetic

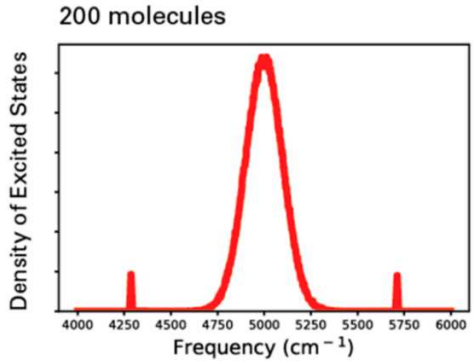

Figure 1.5 *Spectrum of the ensemble one-particle states calculated for 200 molecules coupled to a resonant cavity, with g = 50 cm^{-1}. The transition energies of the molecules are randomly disordered with a standard deviation of 100 cm^{-1}. Reproduced from ref* [18].

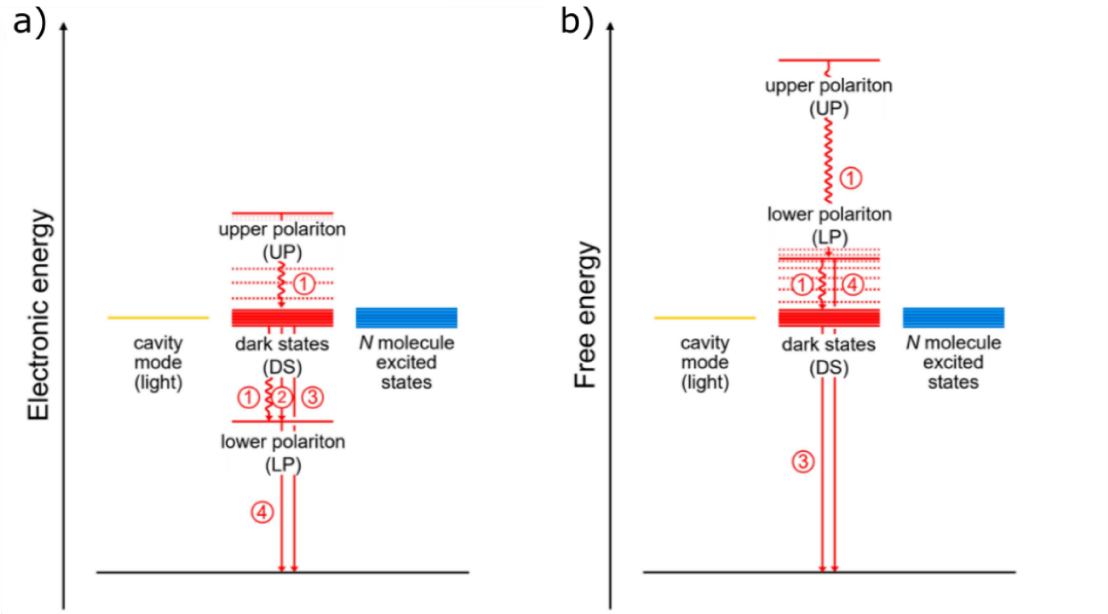

Figure 1.6 *a) Electronic energy and b) free energy levels of a cavity mode (yellow line), excited states of molecules (blue lines), and polariton manifold (red lines) as a result of SC. Nonradiative vibrational relaxation (wavy arrows, process 1) effectively redistributes population from and to DS, which act as a trap. In a conventional view of the electronic energy landscape, DS population either directly decays to the ground state (process 3) quenching the emission or decays to the lower polariton (LP) state via radiative pumping (process 2) and nonradiative vibrational relaxation (process 1). LP relaxes to the ground state by emitting a photon (process 4). In the free energy landscape, LP can decay to DS (process 1), while other decay pathways remain unchanged. Reproduced from ref* [18].

disorder compared to the light-matter coupling strength, polariton bands remain strongly delocalized. This happens because the LP state is significantly split away from the other states (figure 1.5), which hampers the usual mechanism for decoherence and localization. Furthermore, the polariton bands are not broadened commensurate to the disorder (e.g., compared to the DS density of states). This band shape narrowing is attributed to exchange narrowing.[30]

In addition to these aspects, energetic disorder introduces the concept of entropy and free energy, which can also induce a reordering of the states (figure 1.6).[18] Therefore, it is clear that energetic disorder must be considered to get a more comprehensive picture as it strongly affects how states interact with each other, and so the overall dynamics.

1.1.5 Two-particle states

So far, we discussed only about one-particle states, i.e., eigenstates originated by a superposition of states with $N_{exc} = 1$. However, in order to wholly understand the excited states dynamics, eigenstates generated from states with $N_{exc} = 2$ must be taken into consideration.

The starting states with two excitations are: (i) the state with two excitons and no photon $|e_i e_j, 0\rangle$, (ii) the state with one exciton and one photon $|e_1, 1\rangle$, and (iii) the state with no exciton and two photons $|G, 2\rangle$. In the resonance condition, all these states have the energy $E = 2\hbar\omega$. The highest and lowest eigenstates of the TC Hamiltonian (eq. 1.25) in the two-particle subspace are given by the upper (2UP) and lower (2LP) two-particle polaritons:[28]

$$|2, \pm\rangle = \frac{1}{\sqrt{2}}\sqrt{\frac{N}{(2N-1)}}|G, 2\rangle \pm \frac{1}{\sqrt{N2}}\sum_{i=1}^{N}|e_i, 1\rangle + \frac{1}{\sqrt{N(2N-1)}}\sum_{i=1, j>i}^{N}|e_i e_j, 0\rangle \quad (1.33)$$

with eigenfrequencies:

$$\omega_{\pm}^{(2)} = 2\omega \pm 2g\sqrt{N - 1/2} \quad (1.34)$$

Note that for finite N, $E_{2UP} < 2E_{UP}$ and $E_{2LP} > 2E_{LP}$. In other words, the two-particle Rabi splitting $\Omega_R^{(2)} = E_{2UP} - E_{LP}$ is smaller than twice the one-particle Rabi splitting Ω_R. Only in the limit of infinite N, $\Omega_R^{(2)} = 2\Omega_R$.

The two-particle polariton 2UP (2LP) is optically allowed from the one-particle polariton UP (LP) with a transition dipole moment given by:[28]

$$|\langle UP|\hat{\boldsymbol{\mu}}|2UP\rangle| = |\langle LP|\hat{\boldsymbol{\mu}}|2LP\rangle| = \boldsymbol{\mu_{eg}}\left(\frac{\sqrt{N}}{2} + \frac{(N-1)}{\sqrt{2(2N-1)}}\right) \quad (1.35)$$

$$with \quad \hat{\boldsymbol{\mu}} = \boldsymbol{\mu}_{eg} \sum_{i=1}^{N} (\hat{\sigma}_i^{\dagger} + \hat{\sigma}_i) \tag{1.36}$$

In addition to the 2UP and 2LP, there is another polariton state in the two-particle manifold that is optically accessible from the LP and UP. This is a state located at twice the energy of the cavity mode 2ω:[28]

$$|2\omega\rangle = \sqrt{\frac{N-1}{(2N-1)}}|G,2\rangle - \sqrt{\frac{2}{(N-1)(2N-1)}} \sum_{i=1,j>i}^{N} |e_i e_j, 0\rangle \tag{1.37}$$

The strength of the transition dipole moment from LP and UP is:

$$|\langle UP|\hat{\boldsymbol{\mu}}|2\omega\rangle| = |\langle LP|\hat{\boldsymbol{\mu}}|2\omega\rangle| = \boldsymbol{\mu_{eg}} \sqrt{\frac{2(N-1)N}{2N-1}} \tag{1.38}$$

The model also predicts a collection of degenerate dark states at energy 2ω (2DS). These are given by the (un-normalized) expression:[28]

$$|2DS\rangle = \sum_{i=1,j>i}^{N} c_{ij} \big| e_i, e_j, 0 \big\rangle \quad with \quad \sum_{i \neq j}^{N} c_{ij} = 0 \tag{1.39}$$

These states are optically forbidden from the one-particle states.

Finally, the model also predicts additional states between the 2LP and 2ω and 2ω and 2UP states, which are given by the (un-normalized) expression:[28]

$$|DUP/DLP\rangle = \sum_{i=1}^{N} c_i' |e_i, 1\rangle \pm \sqrt{\frac{1}{N-2}} \sum_{i=1,j>i}^{N} \left(c_i' + c_j'\right) |e_i e_j, 0\rangle \tag{1.40}$$

$$with \quad \sum_{i=1}^{N} c_i' = 0 \tag{1.41}$$

and with eigenfrequencies:

$$\omega_{DUP/DLP} = 2\omega \pm g\sqrt{N-2} \tag{1.42}$$

These states are optically dark from LP and UP, but optically allowed from the dark states $|DS\rangle$ at energy $\hbar\omega$.

These states are schematized in figure 1.7, which shows how two-particles states can be populated through excited state absorption from the one-particle states.

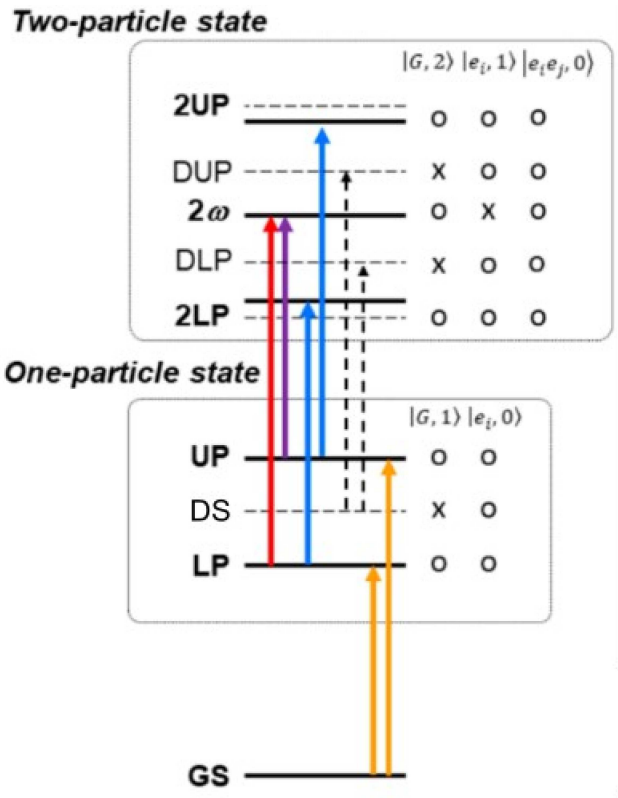

Figure 1.7 *Spectral features assignments for polaritonic states. Ladder of states predicted using the TC model including two-particle states. Terms contributing to each state are marked with an O, while absent terms are marked with an X. Optically allowed transitions between the GS and one-particle states and between one- to two-particle states are indicated by arrows. Note that transitions from the one-particle DSs at energy $\hbar\omega$ to optically bright DUP and DLP states are allowed and indicated with black dashed arrows. Other two-particle states without predicted optical transitions are omitted for clarity. Adapted from ref* [28].

1.2 Plexcitons: hybrid states generated from plasmon-exciton strong coupling

In this section an important class of hybrid states emerging from the SC between light and matter is outlined: plexcitons. Plexcitons are a particular example of polaritons emerging from the SC between plasmons of metal nanostructures (acting as cavities) and molecular excitons.[2,3,5,7,15] But first, to better understand the photophysical properties of plexcitons, a fundamental description of the uncoupled constituents, molecular excitons, and metal plasmons, is necessary.

1.2.1 Molecular excitons

Excitons refer to electronic excited states delocalized over more than one molecule. This is the result of the strong interaction between excited states of strongly coupled monomer units in molecular crystals or aggregate systems.[31,32] As a consequence of the SC, the initial states of the monomers mix, and the excitation is delocalized all over the participating monomers.

The simple model of Kasha,[33] which describes the coupling between only two molecules (excitonic dimer), helps to understand the fundamental principles. Let's consider two identical molecules. Each of them has a ground $|g\rangle$ and an excited $|e\rangle$ states, with transition energy $\hbar\omega$, and transition dipole moment $\boldsymbol{\mu_{eg}}$. In the absence of coupling, the full system can be described by specifying the electronic state of each molecule, leading to four possible states: (i) the state with both molecules in the ground state $|G\rangle$, with energy equal to zero; (ii) the states with the excitation in the first $|1\rangle$ or in the second $|2\rangle$ molecule, with energy $\hbar\omega$; and (iii) the state with both molecules excited $|12\rangle$, with energy $2\hbar\omega$.

As a result of the coupling, the excited states $|1\rangle$ and $|2\rangle$ are mixed, giving rise to two new states $|-\rangle$ and $|+\rangle$, called excitons:

$$|\pm\rangle = \frac{1}{\sqrt{2}}(|1\rangle \pm |2\rangle) \tag{1.43a}$$

$$\hbar\omega_{\pm} = \hbar\omega \pm J + \Delta W \tag{1.43b}$$

with J being the exciton splitting term, or Coulomb coupling, and ΔW is the difference in the Van der Waals stabilization energies of the ground and excited state in the dimer, typically negligible.[32,33] In the point-dipole approximation, J can be expressed as:

$$J = \frac{\left|\boldsymbol{\mu_{eg}}\right|^2}{|\boldsymbol{r_{12}}|^3}\kappa \tag{1.44a}$$

$$\kappa = \left(\hat{\boldsymbol{u}}_{\boldsymbol{eg,1}} \cdot \hat{\boldsymbol{u}}_{\boldsymbol{eg,2}}\right) - 3\left(\hat{\boldsymbol{u}}_{\boldsymbol{eg,1}} \cdot \hat{\boldsymbol{z}}_{\boldsymbol{12}}\right)\left(\hat{\boldsymbol{u}}_{\boldsymbol{eg,2}} \cdot \hat{\boldsymbol{z}}_{\boldsymbol{12}}\right) \tag{1.44b}$$

where κ is the orientational factor, $\boldsymbol{r_{12}}$ is the vector defining the distance between the two molecules, and $\hat{\boldsymbol{u}}_{\boldsymbol{eg}}$ and $\hat{\boldsymbol{z}}_{\boldsymbol{12}}$ are the normalized vectors of $\boldsymbol{\mu_{eg}}$and $\boldsymbol{r_{12}}$, respectively. Physically, the SC accounts for the delocalization of the excitation energy among the two molecules, and the splitting energy $2J$ quantifies the strength of the interaction between them. The two

eigenstates $|\pm\rangle$ are a superposition of states in which the excitation is located in the first or the second molecule. Thus, when the system is described by excitonic states, the energy is coherently exchanged between the two molecules.

It is worth noting the dependency of J on the geometry of the system. The simplest form for J is obtained when the two monomers have parallel dipole moments, thus:

$$J = \frac{\left|\boldsymbol{\mu_{eg}}\right|^2}{|\boldsymbol{r_{12}}|^3}(1 - 3\cos^2\theta) \tag{1.45}$$

where θ is the angle formed by the dipole moments and the ideal line joining the centers of the monomer molecules. When θ matches the value of a critical angle $\theta_M = \arccos\left(\frac{1}{\sqrt{3}}\right) = 54.75°$, then $J = 0$. When $\theta < \theta_M, J < 0$ and the dipoles maintain a "head-to-tail" orientation: the dimer is defined as J-dimer. In this case, one founds that $\hbar\omega_+ < \hbar\omega_-$. H-dimers, in which the monomers assume a "face-to-face" orientation, are instead obtained when $\theta_M < \theta < \pi/2$. In this case $J > 0$ and $\hbar\omega_+ > \hbar\omega_-$.

Furthermore, the model also predicts the transition dipole moment from the ground to the two excitonic states:

$$\widehat{\boldsymbol{M}} = \widehat{\boldsymbol{\mu}}_{\boldsymbol{1}} + \widehat{\boldsymbol{\mu}}_{\boldsymbol{2}}$$

$$\boldsymbol{M}^{\pm} = \langle \pm|\widehat{\boldsymbol{M}}|G\rangle = \frac{1}{\sqrt{2}}\left(\boldsymbol{\mu_{eg,1}} \pm \boldsymbol{\mu_{eg,2}}\right) \tag{1.46b}$$

$$|\boldsymbol{M}^{+}| = \sqrt{2}\left|\boldsymbol{\mu_{eg}}\right| cos\beta \tag{1.46c}$$

$$|\boldsymbol{M}^{-}| = \sqrt{2}\left|\boldsymbol{\mu_{eg}}\right| sin\beta \tag{1.46d}$$

with β the angle between $\boldsymbol{\mu_{eg,1}}$ and $\boldsymbol{\mu_{eg,2}}$. Thus, the respective oscillator strength results:

$$|\boldsymbol{M}^{+}|^2 = 2\left|\boldsymbol{\mu_{eg}}\right|^2 \cos^2\beta \tag{1.47a}$$

$$|\boldsymbol{M}^{-}|^2 = 2\left|\boldsymbol{\mu_{eg}}\right|^2 \sin^2\beta \tag{1.47b}$$

From these equations, it is clear that the intensity of these bands depends on the geometry of the dimer. In J-dimers the oscillator strength is concentrated on the lower energy state. This leads to a lower transition energy compared to the individual monomers and a redshifted absorption band. In H-dimers, the bright transition results at higher energy than the isolated monomers, and a hypsochromic shift of the absorption band occurs. Figure 1.8 shows the energies trend of the exciton states as a function of θ, with $\beta = 0$.

The approach described for the homodimer can be generalized to aggregates involving a higher number of molecules. In this case the Frenkel excitons model is adopted,[34] which starts from an aggregate made of a linear array of N-coupled two-level chromophores. In the Frenkel

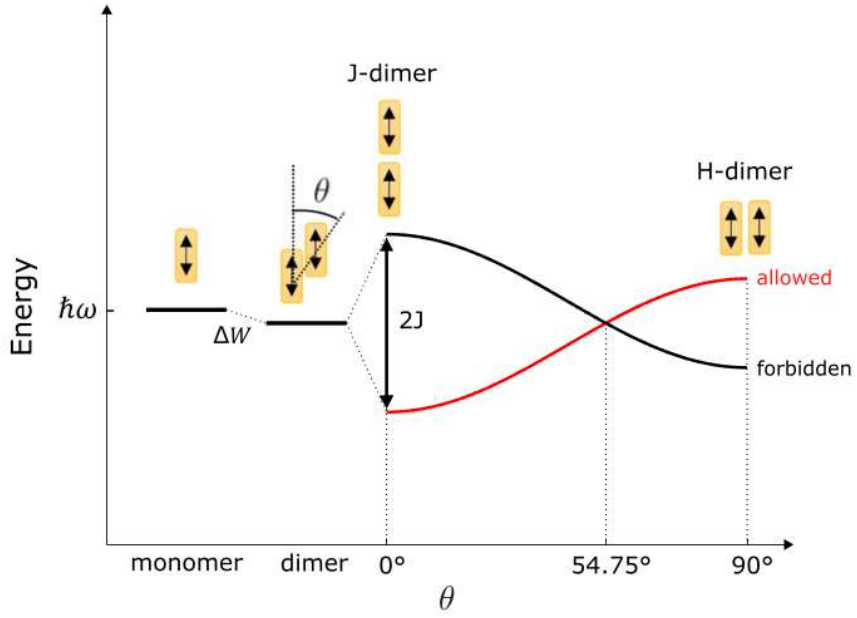

Figure 1.8 *Energy diagram of an excitonic dimer with different geometrical arrangements. The two contributions, the energy stabilization due to the Van der Waals interaction* ΔW*, and the Coulomb splitting* $2J$ *are separately identified. In the case of parallel dipoles (*$\beta = 0$*), the state* $|+\rangle$ *(in red) is optically active with* $|\boldsymbol{M}^{+}| = \sqrt{2}|\boldsymbol{\mu}_{eg}|$*, while the state* $|-\rangle$ *is optically inactive as* $|\boldsymbol{M}^{-}| = 0$*. Adapted from ref* [43].

exciton, the delocalization is extended over N molecules and, for the bright state, the transition dipole is enhanced by a $\sqrt{N}$ factor, analogously to what already found for the dimer. Furthermore, the delocalization over a large number of monomers causes a linewidth narrowing, due to averaging over local inhomogeneities, proportional to $1/\sqrt{N}$, where N is the number of monomer units.[35] This phenomenon is known as the exchange narrowing mechanism.[36] Another feature that distinguishes J- and H-aggregates is the difference in their radiative decay rate. In the first case, the lowest exciton state is radiatively coupled to the

ground state with a transition dipole enhanced by a $\sqrt{N}$ factor relative to the monomer, while in the second, there is no direct radiative coupling between the lowest exciton state and the ground state because the transition is forbidden by symmetry. Since the radiative decay rate scales as the second power of the transition dipole moment, under certain condition the decay rate in J-aggregates can be N-times that of the monomer. This phenomenon is known as superradiance.[37,38]

These features, such as high transition dipole moments, extended energy delocalization and narrow bandwidths, are ideal for reaching the SC conditions with a plasmon resonance to form plexcitons efficiently. Thus, in this Thesis we focused our attention on porphyrins and cyanines, which are two classes of organic dyes well-known to easily form J-aggregates.[39–41]

1.2.2 Localized plasmon resonance of metallic nanoparticles

Plasmons are collective oscillations of free electrons in metals. Since these oscillations occur at a well-defined frequency, a plasmon is classified as a bosonic quasiparticle excitation and corresponds to a quantum of plasma oscillation. Alternatively, a plasmon can be described as a negatively charged electron cloud that is coherently displaced from its equilibrium position around a lattice of positively charged ions.[13,42] The direct excitation of plasmons by the electric field is not allowed in bulk materials. On the other hand, the presence of a surface in real materials enables the existence of specific plasmon modes, which can be excited by the electric field. In the case of metallic nanoparticles (NPs), the electric field of an incident electromagnetic wave can penetrate the metal and polarize its conduction electrons. Since NPs typically have a size much smaller than the photon wavelength, the originated plasmon excitation does not propagate, resulting distributed on the whole NP volume, so it is defined as Localized Surface Plasmon (LSP). Moreover, in NPs, the plasmon can be described as a harmonic oscillator driven by the resonant electric field. Plasmons can be considered as the “light” states that take part in the light-matter coupling. In fact, plasmon resonances also have the effect of confining the electromagnetic field in the proximity of the particle surface. Thus, plasmonic substrates act like a cavity with a very small mode volume V_m.[20] In addition, the plasmon resonance strongly depends on the shape and the size of the NP.[12,13]

1.2.2.1 Linear optical properties of metallic nanoparticles.

The absorption spectra of spherical particles can be modeled by using the Mie theory, given that the dielectric constant of the particle and the environment are known. In the quasi-static limit approximation, i.e., when the particles are much smaller than the wavelength of the light, it gives:[12]

$$\sigma_{abs} = \frac{9V\omega}{c}\varepsilon_m^{3/2}\frac{\varepsilon_2}{(\varepsilon_1 + 2\varepsilon_m)^2 + \varepsilon_2^2} \tag{1.48}$$

Where σ_{abs} defines the absorption coefficient, V is the volume of the particle, ε_m is the dielectric constant of the medium and $\varepsilon(\omega) = \varepsilon_1(\omega) + i\varepsilon_2(\omega)$ is the dielectric constant of the metal which can be obtained from the Drude Sommerfeld model for the free electron gas:[12]

$$\varepsilon = 1 - \frac{\omega_p^2}{\omega^2 + i\Gamma\omega} \tag{1.49}$$

where ω is the frequency of the electromagnetic field, and Γ the damping caused by electron scattering; $\omega_p = \sqrt{ne^2 / \varepsilon_0 m_{eff}}$ is the bulk plasma frequency where n is the carrier density and m_{eff} the effective carrier mass. Combining equations 1.48 and 1.49, the absorption coefficient can be approximated with a Lorentz profile:[43]

$$\sigma_{abs} \approx \frac{\sigma_0}{\left(\omega - \omega_{pl}\right)^2 + (\Gamma/2)^2} \tag{1.50}$$

with σ_0 a constant that encloses all the constant terms of eq. 1.48 and $\omega_{pl} = \omega_p / (\sqrt{1 + 2\varepsilon_m})$ the localized surface plasmon resonance. Thus, the absorption profile is centered at ω_{pl} and the full width at half maximum (FWHM) is equivalent to the damping factor Γ. If the quasi-static limit is not achieved, an increase in the particle size involves a red-shift and broadening of the plasmon resonance (figure 1.9). The red-shift is a retardation effect; it occurs because the electric field is not uniform across the particle, while the broadening comes from radiation damping.[44] However, not only the size of a metal particle can change the plasmon resonance but also its shape. For ellipsoidal NPs, the respective local field depends on the polarization of the incident wave along the three principal axes *a*, *b*, and *c*. Therefore, plasmon resonances can occur along each of them. For spheroidal particles, such as nanorods (NRs), the transverse dimensions are identical: $a = b < c$. Depending on the polarization vector of the incident electric

field, either the transverse or longitudinal plasmon resonances can be excited (figure 1.10).[45] The aspect ratio *c*:*a* defines their spectral position. The longitudinal plasmon shifts to lower frequencies with increasing aspect ratios.[46] Since gold NRs with different aspect ratios are easily synthesizable, the longitudinal plasmon resonance of these nanosystems is easily tunable. In this Thesis we label longitudinal and transverse plasmons with the acronyms LM and TM, which stand for longitudinal mode and transverse mode, respectively.

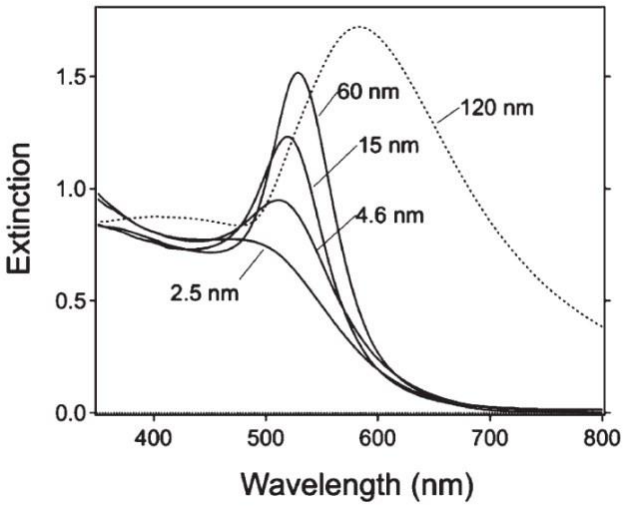

Figure 1.9 *Extinction spectra of different sized Au NPs recorded in aqueous solution (diameters are given in the figure). Reproduced from ref* [12].

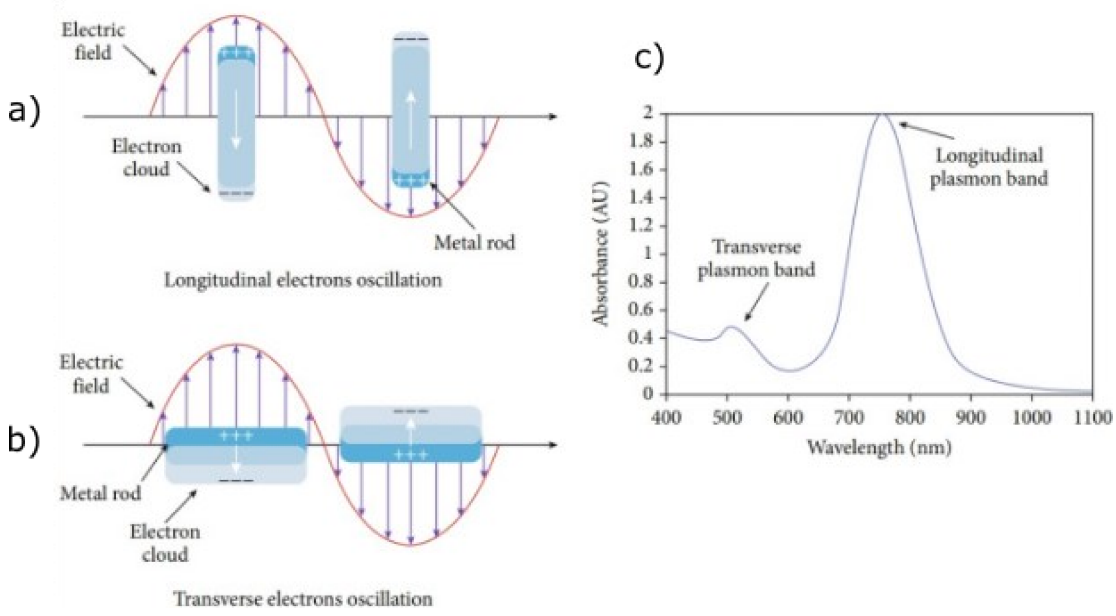

Figure 1.10 *Schematic illustration of a) Longitudinal and b) Transverse plasmon resonances in ellipsoidal NPs. c) A typical extinction spectrum of a gold NRs solution. Reproduced from ref* [45].

1.2.2.2 Damping mechanisms of plasmons.

The bandwidth of a single NP is associated with the dephasing time of the coherent electron oscillation, with a larger bandwidth corresponding to a faster loss of coherence.[46–48] Typical electron dephasing times in Au NRs are in the order of 6-50fs,[13] and this value sets the plasmon bandwidth. The total line width Γ (FWHM) is contributed by a radiative (Γ_r) and a non-radiative (Γ_{nr}) term and can be expressed as:[49]

$$\Gamma = \Gamma_{nr} + \omega^2 \Gamma_r \tag{1.51}$$

The radiative term is associated with the far-field radiation emitted by accelerating and decelerating charged particles. It becomes more important for increasing NP size; however, for 20 nm Au NPs it accounts for only a few percent.[13]

The non-radiative decay includes several dephasing mechanisms collectively identified as Landau damping, in which the energy is transferred into lower-energy electron-hole pair excitations in a timescale of 1-100 fs.[48,50,51] The electron-hole pair's excitation can be either intraband or interband.[13] After electron-hole formation by Landau damping, electron-electron scattering takes place on a time scale of 0.5 ps leading to electron thermalization. In this way,

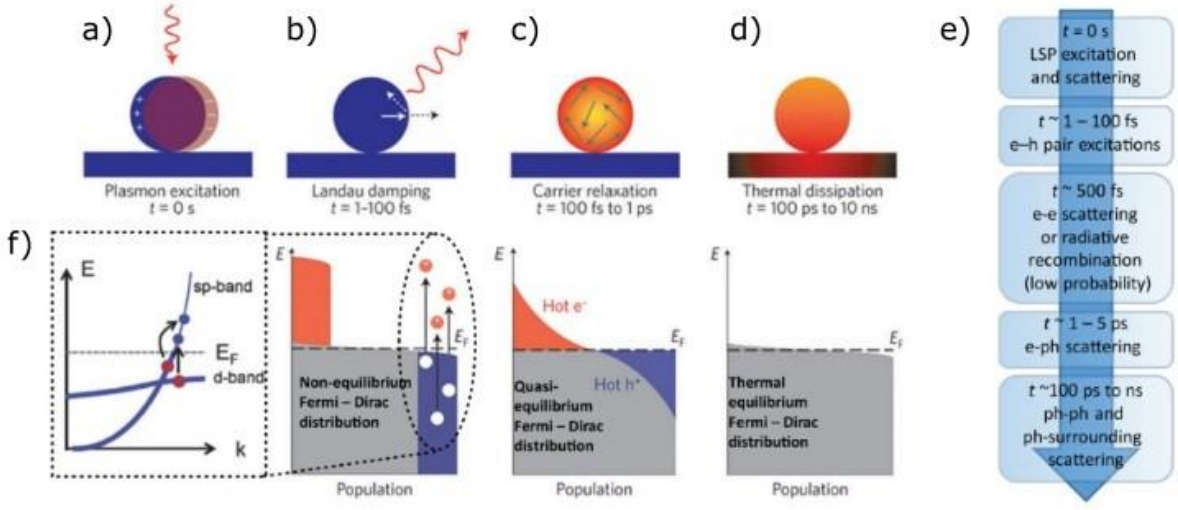

Figure 1.11 *After LSP excitation a), the athermal distribution of electron–hole pairs decays in 1–100 fs by photon emission (radiatively) or through b) Landau damping and the formation of hot carriers (non-radiatively). c) Hot carriers redistribute their energy by electron–electron scattering on a timescale ranging from 100 fs to 1ps. Then, heat is transferred inside the NP by electron–phonon (e–ph) scattering on a timescale of a few picoseconds, and d) from the NP to the surroundings on a timescale of several picoseconds to nanoseconds. e) The complete timeline of SPR relaxation. f) The formation of electron–hole pairs in Au can be either interband or interband. The Fermi electron population is reported in grey, hot electrons are represented by the red areas above the Fermi energy (E_F), and hot-hole distributions are represented by the blue area below E_F. Adapted from ref* [13].

electron energies rearrange from a non-equilibrium to the quasi-equilibrium Fermi-Dirac distribution, corresponding to the system thermal energy plus the energy of the absorbed photon.[48] This means that for times <500 fs after plasmon excitation, the electronic gas temperature is still higher than the lattice temperature.[47,48] Then, in 1-5 ps, electron-phonon scattering leads to the thermalization of the electrons with the lattice.[47,48] The last process involves phonon–phonon interaction between the lattice and the surrounding medium, with a time scale ranging from hundreds of picoseconds to nanoseconds.[47,48] In general, one should consider that all these relaxation mechanisms are partially overlapping in time. Besides, their precise time scale depends on the intensity of the light and the external temperature.[52] Figure 1.11 schematizes the dynamics of plasmon upon photoexcitation.

1.2.3 Plexcitons

In the previous sections, we described the fundamental characteristics of excitons and plasmons. Plexcitons are polaritonic modes that essentially describe the interaction of plasmons and excitons.[7] Most commonly, plexcitons are observed when a J-aggregate of an organic dye is templated on the surface of a metal NP. In this way, the excitonic states of the aggregate can strongly interact with the strong electric field confined on the NP surface generated by the plasmonic resonance.

Recalling the SC conditions (section 1.1.2), it is easy to understand why J-aggregates of organic dye and plasmonic substrates are suitable for strong light-matter interaction. In fact, J-aggregates are characterized by a high transition dipole moment (eq. 1.46) that contributes to the coupling strength g (eq. 1.10), and a narrow bandwidth, which reflects a low dephasing rate γ. Then, despite the huge losses of plasmons (note that k of eq. 1.22 is equal to $\Gamma/2$), their effective volume is orders of magnitude smaller than in optical cavities.[2,24] And the effective volume V_m also contributes to the coupling strength (eq. 1.31). In addition to this, the plasmon resonances of gold NRs are easily tunable, allowing to easily achieve the resonance conditions with different aggregates of organic dye.

Building on these observations, in this Thesis we prepared and characterized plexcitonic nanohybrids based on gold NRs and J-aggregates of organic dyes.

1.2.3.1 Plexcitons and polaritons dynamic: a brief overview

Because of their complexity, optical nonlinearities of plexcitons are very challenging to describe and understand, and the debate about the interpretation of the various dynamic phenomena is still particularly vibrant. In fact, while the energy levels of the emerging plasmon-exciton systems can be predicted by theoretical models with reasonable success,[3,4,15,16] how plexcitons interact among themselves and with other states is much less clear, making it difficult to predict how plexcitons formation might ultimately be used to control excited-state processes.

One of the most interesting features in plexcitonic, or generally, polaritonic systems, is their coherent dynamic properties, i.e., the Rabi oscillations. Resolving coherence among plexcitonic states is a challenging task as it requires a very demanding time resolution, below 10 fs. One of the few experimental characterizations of this phenomenon has been provided by Vasa et al., who have reported evidence of plexcitonic coherence by using pump and probe spectroscopy.[53] The polaritonic dynamics for timescale above the 100fs are much more studied. Generally, according to the intuitive downhill relaxation model, it is expected that UP relaxes fast to DSs, which in turn populate LP.[23] However, the exceptions to this picture are numerous because of the vast variability of polaritonic systems. Moreover, recent literature works tried to explain polaritons nonlinearities by invoking complex energy redistribution processes between different states (including polaritons, DSs and plasmon states) in the picosecond timescale.[18,54] In addition to this, the energetic disorder of these states also seems to play a fundamental role in the dynamic processes.[55] Thus, the easy picture of the UP, DS and LP states connected by a downhill sequential energy relaxation has been overcome.

Another interesting feature is the Rabi contraction observed at high enough fluences. This phenomenon has already been characterized and well rationalized.[56] The contraction is the consequence of the photoinduced reduction of the number of ground state molecules effectively coupled to the cavity.[28] In fact, when plexcitons are excited by the pump pulse, an (incoherent) exciton population remains in the dye molecules within the exciton lifetime, consequently fewer molecules can couple with the plasmonic mode. Then, the Rabi splitting, which is proportional to the root square of the number of interacting molecules (eq. 1.31), decreases.

Chapter 2
Experimental methodologies

In this Chapter the experimental techniques employed in this Thesis, with a particular focus on the pump and probe technique, are described. Then, the synthetic methodologies adopted for the preparation of gold NRs and nanohybrids are illustrated. Finally, the software used for the data analysis is defined.

2.1 Stationary linear spectroscopy

2.1.1 UV-Visible Spectroscopy

UV-Vis spectroscopy is a technique that exploits the linear response of the matter to light, to measure the extinction spectra in the UV-Visible range. There are two contributions to the extinction: the absorption and the scattering of light (the latter becomes relevant only for particles whose size is comparable to the wavelength of the light source, such as metallic NPs). This technique is sensitive to the transmittance T:

$$T = \frac{I}{I_0} = 10^{-\varepsilon C r} \tag{2.1}$$

with I the transmitted intensity, I_0 the incident intensity, ε the extinction coefficient ($[\varepsilon] = M^{-1}cm^{-1}$), C the molar concentration of the sample and r the optical path of the light in the sample. The absorbance A is defined as $-\log_{10} T$, then the Beer-Lambert law is obtained:[57]

$$A = \varepsilon C r \tag{2.2}$$

In this Thesis, extinction spectra were recorded with a Cary 5000 spectrophotometer.

2.1.2 Circular Dichroism (CD) Spectroscopy

Circular Dichroism (CD) spectroscopy is based on the measure of the differential absorption of left and right circularly polarized light (LCP and RCP, respectively). Optically active systems will preferentially absorb one direction of the circularly polarized light. Thus, the CD signal is proportional to the differential absorption:[58]

$$\Delta A = A_L - A_R \tag{2.3}$$

with A_L and A_R the absorbance of left and right circularly polarized light, respectively. This directly derives from a difference in the extinction coefficients:

$$\Delta\varepsilon = \varepsilon_L - \varepsilon_R \tag{2.4}$$

A linearly polarized light can be expressed as a superposition of LCP and RCP of the same amplitude. When such a linearly polarized light interacts with a chiral medium, since the molar absorptivities of LCP and RCP light are different, they will be absorbed in different amounts. This differential absorption results in the LCP and RCP components having different amplitudes, which means that the outcoming light is no longer linearly polarized. The resulting wave is elliptically polarized. Thus, the CD spectrum is often reported in degrees of ellipticity, θ, which is the measure of the ellipticity of the polarization given by:

$$tan\theta = \frac{E_L - E_R}{E_L + E_R} \tag{2.5}$$

with E_L and E_R the amplitude of LCP and RCP components, respectively. The change in polarization is usually small and the signal is often measured in degrees, giving:

$$\theta = 32.98\Delta A \tag{2.6}$$

In this Thesis, the CD spectra were collected with a JASCO 715 CD spectrophotometer.

2.2 Time-resolved nonlinear spectroscopy

2.2.1 Introduction to Optical Nonlinearities

Nonlinear optical properties appear as a response of a medium to a strong electromagnetic field. Optical observables are proportional to the polarization $\boldsymbol{P}$, which is the macroscopic response of the matter to an electric field. In a first approximation, the polarization depends linearly on the electric field $\boldsymbol{E}$:[59]

$$\boldsymbol{P}(t) = \epsilon_0 \, \boldsymbol{\chi}^{(1)}\mathbf{E}(t) \tag{2.7}$$

with ϵ_0 the vacuum permittivity and $\boldsymbol{\chi}^{(1)}$ the linear susceptibility. However, for a high enough electric field, this is no longer true. In a perturbative approach, the nonlinear polarization can be expressed in powers of the electric field:

$$\boldsymbol{P}(t) = \epsilon_0 \left[\boldsymbol{\chi}^{(1)}\mathbf{E}(t) + \boldsymbol{\chi}^{(2)}\boldsymbol{E}^2(t) + \boldsymbol{\chi}^{(3)}\boldsymbol{E}^3(t) + \ \ldots \right] = \boldsymbol{P}^{L}(t) + \boldsymbol{P}^{NL}(t) \tag{2.8}$$

with $\boldsymbol{\chi}^{(n)}$ the *n*-th order electric susceptibility, $\boldsymbol{P}^{L}(t)$ and $\boldsymbol{P}^{NL}(t)$ the linear and nonlinear polarization, respectively. The $\boldsymbol{P}^{NL}$ can be described as a sum of *n*-th order contributions:[59]

$$\boldsymbol{P}^{NL}(t) = \epsilon_0 \left[\boldsymbol{\chi}^{(2)}\boldsymbol{E}^2(t) + \boldsymbol{\chi}^{(3)}\boldsymbol{E}^3(t) + \ \ldots \right] = \boldsymbol{P}^{(2)}(t) + \boldsymbol{P}^{(3)}(t) + \ \ldots \tag{2.9}$$

Thus, nonlinear effects can be classified based on their order. We are particularly interested in third-order optical properties, which are informative about excited states and their dynamics. The third-order polarization $\boldsymbol{P}^{(3)}$, which is in turn proportional to the experimental third order signal $\boldsymbol{S}^{(3)}$, can be expressed as the convolution of the nonlinear response function $\boldsymbol{R}^{(3)}(t_1, t_2, t_3)$ with the pulse fields $\boldsymbol{E}_j(k_j, t)$:[60,61]

$$\boldsymbol{E}_j\big(k_j, t\big) = A_j\big(t - \tau_j\big)e^{-i\omega(t-\tau_j)+i\boldsymbol{k}_j\cdot\boldsymbol{r}+i\phi_j} + complex\ conjugate \tag{2.10}$$

$$S^{(3)}(t_1, t_2, t_3) \propto \boldsymbol{P}^{(3)}(t_1, t_2, t_3) \propto \int_0^\infty dt_3 \int_0^\infty dt_2 \int_0^\infty dt_1 \, \boldsymbol{R}^{(3)}(t_1, t_2, t_3) \tag{2.11}$$

$$\boldsymbol{E}(t - t_3)\boldsymbol{E}(t - t_3 - t_2)\boldsymbol{E}(t - t_3 - t_2 - t_1)$$

where the j-th laser pulse is centered at τ_j and $\boldsymbol{k}_j, \omega, A_j(t)$, and ϕ_i are wavevector, carrier frequency, temporal envelope, and phase of the field. t_1, t_2 and t_3 are the time intervals between interactions.

Therefore, studying these properties requires deploying a spectroscopy sensitive to the third-order nonlinear polarization. There are different advanced spectroscopies with this characteristic, one of which is the pump-probe spectroscopy.

2.2.2 Pump-Probe Spectroscopy

The pump-probe technique can give information on the dynamics of the electronic states in the time domain between about 100 fs and 1 ns. This technique employs the interaction with two laser pulses, the pump and the probe, with the pump intensity typically noticeably stronger than the probe one. In this experiment, the pump and probe beams are spatially overlapped on the sample, and what is measured is the variation of the probe intensity after the sample at different probe delays to the pump. It is also important to notice that the signal is detected in exactly the same direction as the probe (figure 2.1).[62] The pump and the probe pulses can be monochromatic pulses at the same wavelength ("one-color" pump-probe) or they can have different wavelengths ("two-colors" pump-probe). As in our case, the probe is often a white light continuum containing all the spectral components in the Vis range. The measured signal is given by the differential absorption $\Delta A(T,\lambda)$ as a function of the time delay (T) and the probe wavelength (λ):[63]

$$\Delta A(T,\lambda) = -log_{10}\left(\frac{I_P(T,\lambda)}{I_{NP}(-\infty,\lambda)}\right) = A_P(T,\lambda) - A_{NP}(-\infty,\lambda) \qquad (2.12)$$

with I_P and I_{NP} the intensity of the signal with or without the pump pulse. Analogously, A_P and A_{NP} are the absorbance values in the presence and absence of the pump, respectively.

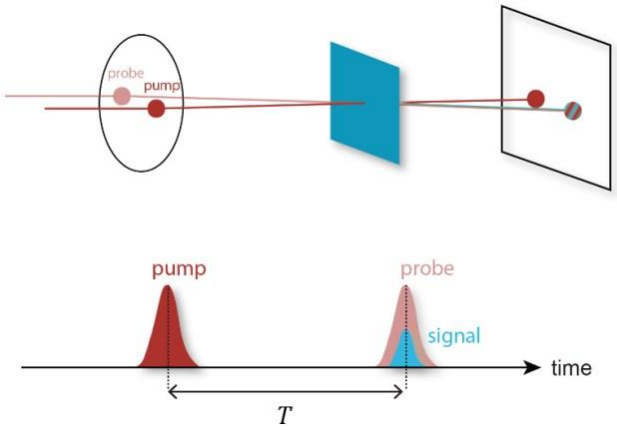

Figure 2.1 *Excitation geometry (upper line) and pulse sequence (lower line) for a pump-probe experiment. Adapted from ref* [62].

Overall, as seen in eq. 2.12, in a pump-probe experiment, the signal is plotted as a function of a delay time T and the probe wavelength λ (figure 2.2a). To compare the experimental outcome ($\Delta A(T,\lambda)$) with the third-order signal $\boldsymbol{S}^{(3)}$and the polarization $\boldsymbol{P}^{(3)}$ appearing in eq. 2.11: (i) the first pulse must be seen as carrying two interactions centered at the same time ($\tau_1 = \tau_0$ and $\tau_2 = \tau_0$, thus $t_1 = 0$); (ii) the delay time experimentally scanned must be seen as the time between the pump and probe pulses ($T = \tau_0 - \tau_3 = t_2$); and the probe frequency (or wavelength) is related to t_3 through a Fourier transform ($2\pi/\lambda = \omega = FT(t_3)$).

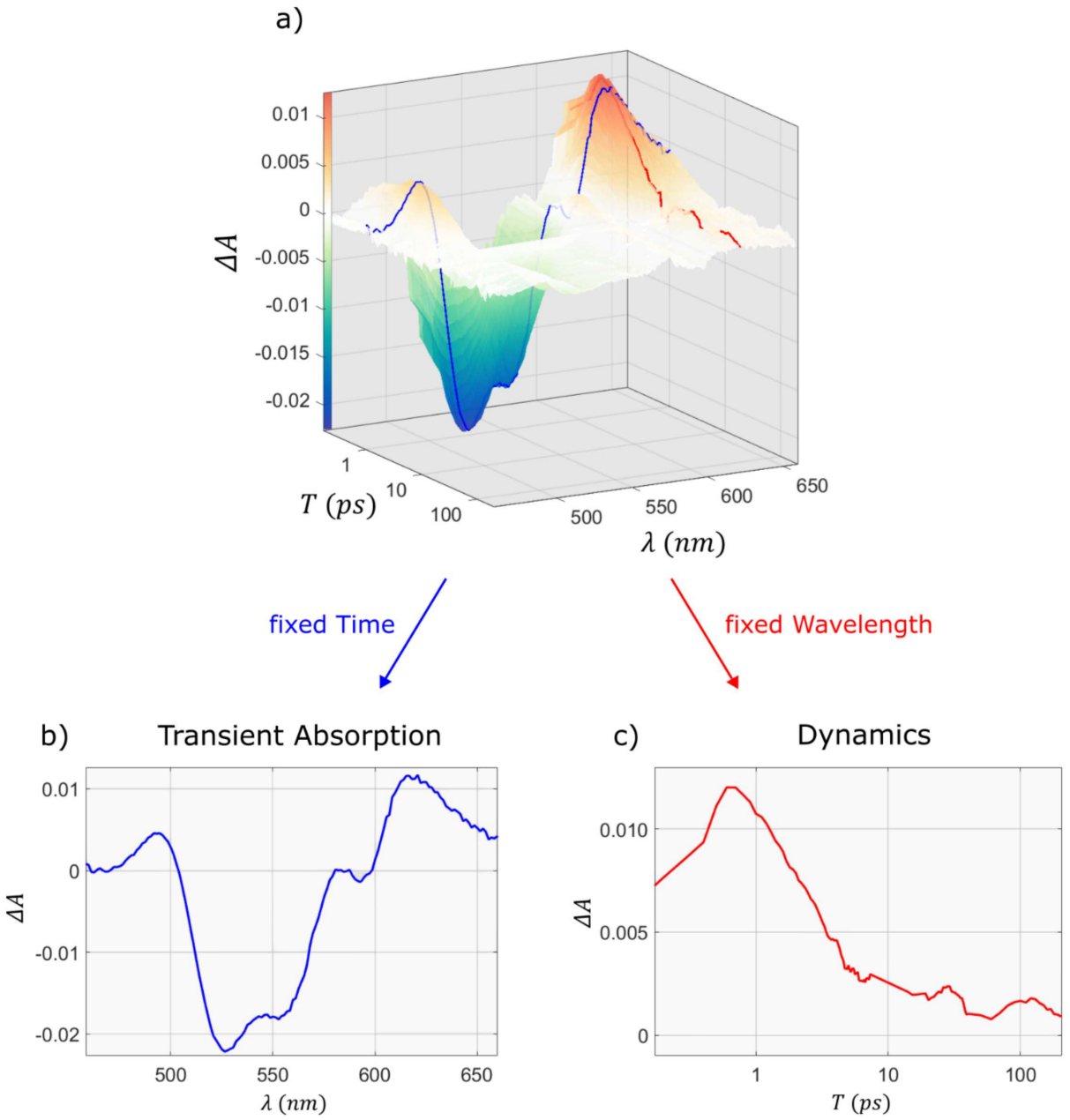

Figure 2.2 *a) Example of a pump-probe signal collected in this Thesis (PI_hy_3_1, see section 3.2.1, table 3.1). The differential absorbance* ΔA *is plotted as a function of the delay time* T *and the probe wavelength* λ*, and visualized through a 2D colormap. b) Transient Absorption spectrum extracted at* $T = 2\ ps$*. c) Dynamics of the signal extracted at* $\lambda = 622\ nm$ *(note the log scale on the x-axis).*

From the overall signal, two different kinds of information can be extracted (figure 2.2). By fixing the delay time T at a specific value, one obtains the Transient Absorption (TA) spectrum, at that delay time, as a function of the probe wavelengths (figure 2.2b). Alternatively, the observation at a fixed wavelength λ allows following the dynamics of the signal as a function of the delay time (figure 2.2c).

To understand the nature of the signals in a pump-probe experiment, it is helpful to consider the simple case of a sample with two energy levels (ground state, $|g\rangle$ and excited state, $|e\rangle$). We also assume that the pump pulse is resonant with the transition $|g\rangle \rightarrow |e\rangle$, and that the probe pulse is a white light supercontinuum. At the time $\tau_0 = 0$, the pump pulse excites the sample, thus some molecules are promoted from the ground to the excited state. If the probe arrives at $T \geq \tau_0$, the system will absorb less photons than in the absence of the pump pulse. This produces a negative ΔA, which, increasing the delay time, recovers to the zero value with a time equal to the characteristic time of the relaxation $|e\rangle \rightarrow |g\rangle$ of the sample considered. This phenomenon is called Ground State Bleaching (GSB, figure 2.3).

Alternatively, the probe pulse can stimulate the relaxation from $|e\rangle \rightarrow |g\rangle$ giving rise also in this case, to a negative ΔA; this phenomenon is called Stimulated Emission (SE, figure 2.4a). Eventually, in samples with a more complex level structure, the probe can excite the sample from $|e\rangle$ to a generic higher energy state $|f\rangle$. This phenomenon is named Excited State Absorption (ESA, figure 2.4b) and contributes with a positive ΔA at the wavelength corresponding to the transition $|e\rangle \rightarrow |f\rangle$. These contributions, like GSB, will decay to zero as the system relaxes back to the ground state.

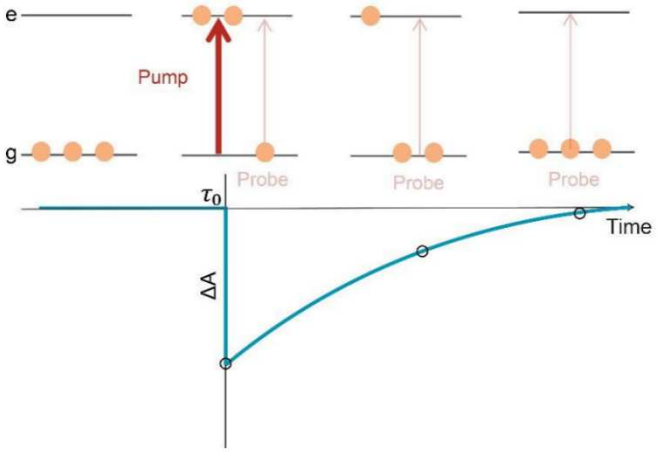

Figure 2.3 *Time evolution of a two-level system addressed in a pump-probe experiment (upper line) and the resulting signal output measured as a function of the delay time between pump and probe pulses (lower line).*

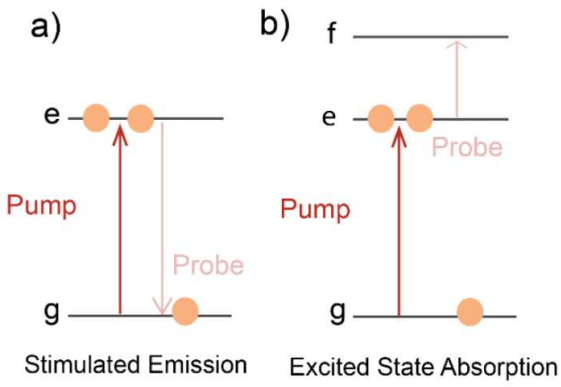

Figure 2.4 *Sketch of a) stimulated emission and b) excited state absorption.*

2.2.2.1 Optical setup

Our laboratory is equipped with the home-built pump-probe setup described in figure 2.5. The pump and probe beams are generated by an amplified Ti:Sapphire laser (Spitfire, Spectra Physics) seeded by a femtosecond pulsed Ti:Sapphire oscillator (Mai-Tai, Spectra Physics). The laser pulses are emitted at 800 nm, with an energy of 0.8 mJ per pulse, a repetition rate of 1 kHz, and a 160 fs pulse duration. The output laser beam is split by a 4% beam splitter into two paths. The weaker one generates a supercontinuum white light in a thin sapphire plate and is used as the probe. The stronger portion is instead used to generate the pump pulse at 400 nm *via* second harmonic generation in a BBO thin crystal. The pump fluence is tuned from 170 to 730 µJ/cm^2 using OD filters and its repetition rate is halved to 500Hz through an optical chopper.

The collimated pump pulse and the focused probe pulse hit the samples in an overlapping region within the sample. In this region, the pump beam diameter is about 60-80 µm and the probe 20-30 µm. The delay between pump and probe pulses is controlled with a motorized linear stage. The transmitted light is dispersed and directed to a linear CMOS diode array. The quality of the TA signal, i.e., ΔA values (differential absorption), is improved through repeated measurements and averaging (150-200 measurements were averaged to obtain a sufficient signal-to-noise ratio). The obtained spectra are numerically processed to minimize white light chirping effects, by using a homemade Matlab routine. Each measure is repeated at least twice to verify the reproducibility of the phenomena.

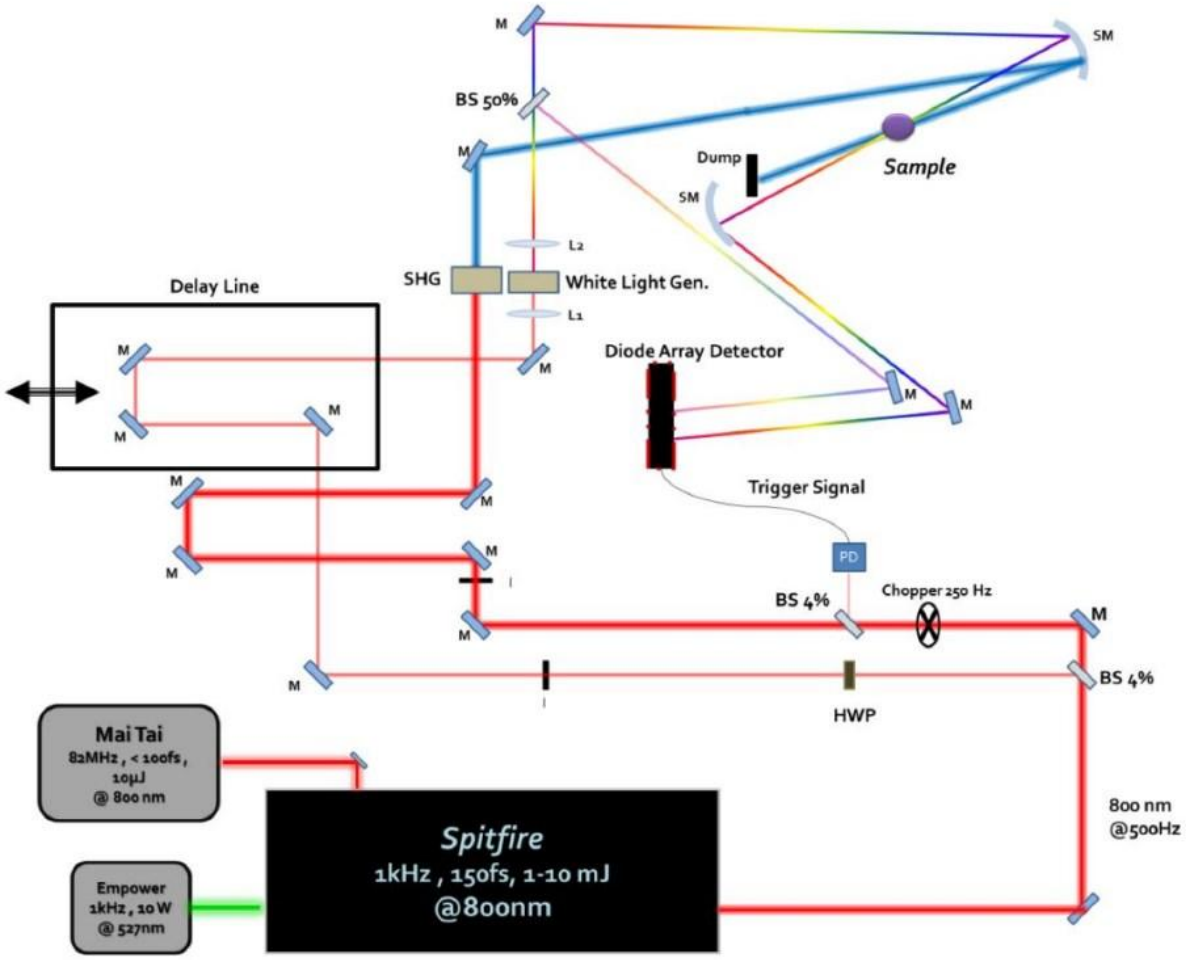

Figure 2.5 *Pump-probe set up built in our laboratory.*

2.3 Preparation of the nanomaterials

All the solvents, reactants and dyes were obtained from Sigma-Aldrich (Merck KGaA, Darmstadt, Germany) and used as received without further purification.

2.3.1 Synthesis of gold nanorods

The Au NRs synthesis was performed adopting the method proposed by L. Liz-Marzán et al.[64] This synthesis involves three main steps, performed separately. These steps are: (i) preparation of the seeds (nucleation), (ii) growth, and (iii) oxidation.

Preparation of the seeds. In a water bath at 27-30 °C, 4.92 µL of a gold (III) chloride solution ($HAuCl_4$, 253.9 mM) and 4.7 mL of a solution of cetyl trimethyl ammonium bromide (CTAB, 100mM) were added to 20 µL of MilliQ water. The mixture was slowly stirred (350 rpm) until complete dissolution of Au salt. Then, 300 µL of a sodium borohydride solution ($NaBH_4$, 10 mM) was rapidly injected under vigorous stirring (1200 rpm): the solution color changed almost immediately from a deep yellow to a light brown, indicating the reduction of gold. After 10-20 seconds the solution was mildly stirred (500 rpm) and stored at 27-30 °C for two hours before it was used.

Growth. In a water bath at 27-30 °C, 190 µL of hydrochloric acid (HCl, 1M), 19.7 µL of $HAuCl_4$ (253.9 mM) and 80 µL of MilliQ water were added to 10 mL of CTAB solution (100mM). The mixture was gently stirred until complete dissolution of the Au salt. Subsequently, 120 µL of a solution of silver nitrate ($AgNO_3$, 10 mM) were added to the mixture. Finally, 100 µL of ascorbic acid solution (100 mM) were added to the mixture, which was gently shaken for a few seconds. The color of the solution changes from pale yellow to colorless. At this point, 24 µL of the seed solution were added to the mixture; the growth solution was shaken (500 rpm) for 30 minutes and then left undisturbed overnight. The following day the solutions of as-prepared NRs were centrifuged at 8000 rpm for 30 minutes, redispersed in 1.5 mL of MilliQ water, centrifuged again at 14000 rpm for 6 minutes and redispersed in 1.5 mL of MilliQ water.

Oxidation. Oxidation of NRs was performed to decrease the aspect ratio, thus to blue shift the longitudinal plasmon peak. The oxidizing solution consists of a water solution containing $HAuCl_4$ (1 mM) and CTAB (100 mM). This solution was added dropwise (0.1 mL/min ca.), under magnetic stirring, into a vial containing the as-prepared gold NRs ([Au]=0.5 mM, estimated through the absorbance value at 400 nm)[64] and CTAB (100 mM). The solution was allowed to react at 27-30 °C for 1 hour, under stirring for the first 30 minutes. Then, the solution was centrifuged twice (9000 rpm for 40 minutes) to remove the excess gold salt and redispersed in 1.5 mL of MilliQ water the first time and in 1 mL of CTAB (15 mM) the second one. The quantity of oxidizing solution was estimated depending on the position of the longitudinal plasmon peak desired. This was done assuming roughly a linear dependence between the peak shift (ΔmeV) and the final concentration of the oxidizing agent (Au^{3+}).

2.3.2 Synthesis of the nanohybrids

The general way adopted to obtain hybrid structures of Au NRs and J-aggregates was the following: different amounts of dye solution were added to 500 µL of an aqueous dispersion of the gold NRs. Since the quantitative determination of the exact concentration of NRs in solution is difficult, in order to make reproducible synthesis, the extinction spectra were exploited. Indeed, we took care that the extinction of the LM in the initial NRs solution before the dye addition was about 0.2 in a 2mm optical path cell. In some cases, the solutions were centrifuged to remove the excess of free dye molecules, and the precipitates were redispersed in MilliQ water. Several samples have been prepared by adding different amounts of dye to the NRs solution in order to check the dependence of the plexcitonic coupling on the concentration of the molecules. For each sample, the resulting concentration of the dye in the final volume was determined. The experimental details relative to the preparation of each sample are reported in Chapter 3 (see in particular table 3.1)

2.4 Data analysis

The raw data obtained from UV-Vis, CD and pump-probe spectroscopy were visualized, analyzed, and elaborated with the software Matlab R2020b. Instead, the fitting of the signal decay dynamics, discussed in section 3.3, was done using the nonlinear fitting app of the software OriginPro 2022. The errors estimated and reported in the tables of Chapter 3 are the errors resulting from the fitting analysis. However, from repeated measurement we could also estimate an error on the time constants in the order of 10-15%.

Chapter 3
Results and discussion

In this section, two families of plexcitonic nanohybrids are discussed, both based on gold NRs coated with J-aggregates of organic dyes. The difference lies in the nature of the organic dyes, which are porphyrins and cyanines. In the first case, we did not manage to get the SC conditions. On the other hand, however, we obtained three different plexcitonic nanohybrids with two distinct cyanines. For these samples, linear and nonlinear optical characterization was performed, and the results are discussed in this section.

3.1 Porphyrin-based nanohybrids

3.1.1 Motivations

As already discussed, plasmonic substrates can act as a cavity with a low volume mode (section 1.2). Furthermore, gold NRs are easy to prepare and their plasmonic resonances are easily tunable (section 2.3.1). Thereby, they are ideal for our purposes.

About the choice of the dyes to be coupled with the NRs, porphyrin molecules have been selected in the first instance. Porphyrins are a class of heterocyclic macrocycle organic compounds composed of four modified pyrrole subunits interconnected at their α carbon atoms via methine bridges. With 18 π-electrons forming a planar, continuous cycle, porphyrins exhibit a large conjugated system responsible for a strong absorption in the visible region of the electromagnetic spectrum.[65,66] Their absorption band can be theoretically explained by the four-orbital model introduced by Gouterman.[66,67] Moreover, porphyrins have a remarkable ability to form molecular aggregates.[39,40] These features make them a class of organic dyes suitable for producing plexcitonic samples. In fact, the narrow and intense absorption band typical of J-aggregates is ideal for reaching strong light-matter coupled systems (section 1.2).

Furthermore, due to its complex optical properties, a porphyrin-based plexciton would ensure a trickier but wider control of the final optical properties. For example, it has already been demonstrated that the doubly protonated form of the anionic dye 5,10,15,20-tetrakis(4-sulfonatophenyl)porphyrin (H_2-$TPPS^{2-}$) associated with gold nanospheres can form a responsive system where two sets of plexcitonic resonances in different coupling regimes can be selectively switched on and off, acting on external conditions such as concentration and presence of anions.[68] Obviously, the simultaneous involvement of multiple states can strongly influence the overall dynamics, and a deep understanding of that could have fundamental implications for achieving control over energy flow at the nanoscale. In addition, porphyrins are strongly related to biologically relevant compounds such as chlorophylls. Therefore, porphyrin-based nanohybrids could have a noticeable relevance in the field of quantum biology.[69]

3.1.2 Sample preparation and optical characterization

Based on the abovementioned motivations, we started with 5,10,15,20-tetrakis(4-sulfonatophenyl)porphyrin (TPPS) and CTAB-capped gold NRs. Figure 3.1 shows the three different forms that TPPS can assume in water solution. H_2-$TPPS^{2-}$ in the monomeric form features two main groups of absorption bands. At higher energies, the so-called B-band at 434 nm can be identified, while at lower energies, the weaker Q-bands are found at 592 and 645 nm. In high ionic strength conditions (obtained for example lowering the pH at ~ 2), H_2-$TPPS^{2-}$ forms J-aggregates. This is evidenced by the presence of two red-shifted bands at 490 and 706 nm, corresponding to the B-band and Q-band of the aggregate, respectively.[70–73] $TPPS^{4-}$ exists in basic conditions as a monomer and shows an intense B-band at 413 nm.

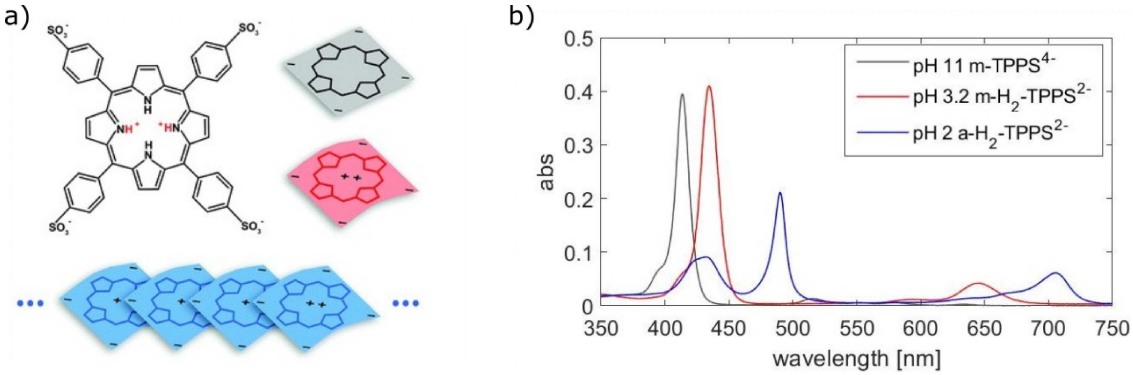

Figure 3.1 *a) Molecular structure of H_2-$TPPS^{2-}$ and the pictorial sketch of the different species possibly present in water solution: free base monomer (m-$TPPS^{4-}$, black), double protonated monomer (m-H_2-$TPPS^{2-}$, red) and aggregate (a-H_2-$TPPS^{2-}$, blue). Reprinted from ref [72]. b) Extinction spectra of the three species in water solution, obtained changing the pH conditions.*

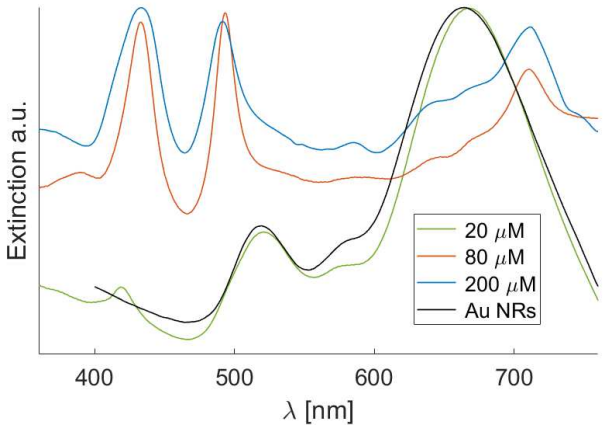

Figure 3.2 *Extinction spectra of an aqueous (pH ~ 2) solution of bare Au NRs (black) and Au NRs in presence of different concentrations of TPPS. The spectra are normalized at their maximum value.*

The target was to couple the J-band of the aggregate (706 nm) with the longitudinal plasmon of gold NRs. Thus, we mixed a water solution (pH ~ 2) of gold NRs (LM peak at 666 nm) with varying concentrations of TPPS dye. Figure 3.2 shows some of the extinction spectra collected. At low concentrations, there is no evidence of plexciton formation; however, a slight red shift of LM peak suggests that the TPPS is interacting with the particle's surface. In fact, the plasmonic resonance depends on the dielectric constant of the medium ε_m (section 1.2.2), so a change in the near surrounding of the particle can induce a variation of the ε_m experienced, thus, a shift of the plasmonic band. At high concentrations, the NRs suspension becomes unstable and starts to precipitate. That is probably because the TPPS molecules are capable of cross-linking; thus, high concentrations of TPPS induce NRs aggregation and precipitation. The signals observed are related to the residual monomer and aggregate dye in solution.

To overcome this problem, we intended to reduce the TPPS-induced aggregation of NRs. Particularly, we acted on three parameters: (i) pH (indeed, by increasing the pH, the aggregate/monomer ratio of TPPS decreases); (ii) concentration of competitor anions (in fact, these can electrostatically interact with the cationic groups $-NH_3^+$ exposed by the particle's surface, hampering their interaction with the anionic porphyrin); (iii) length of NRs (shorter particles have less tendency to aggregate and precipitate). With this in mind, we performed several tests varying the pH (from 2 to 3), the concentration of counterions such as Cl^-, SO_4^{2-}, NO_3^-, and the aspect ratio of gold NRs. The results are summarized in figure 3.3.

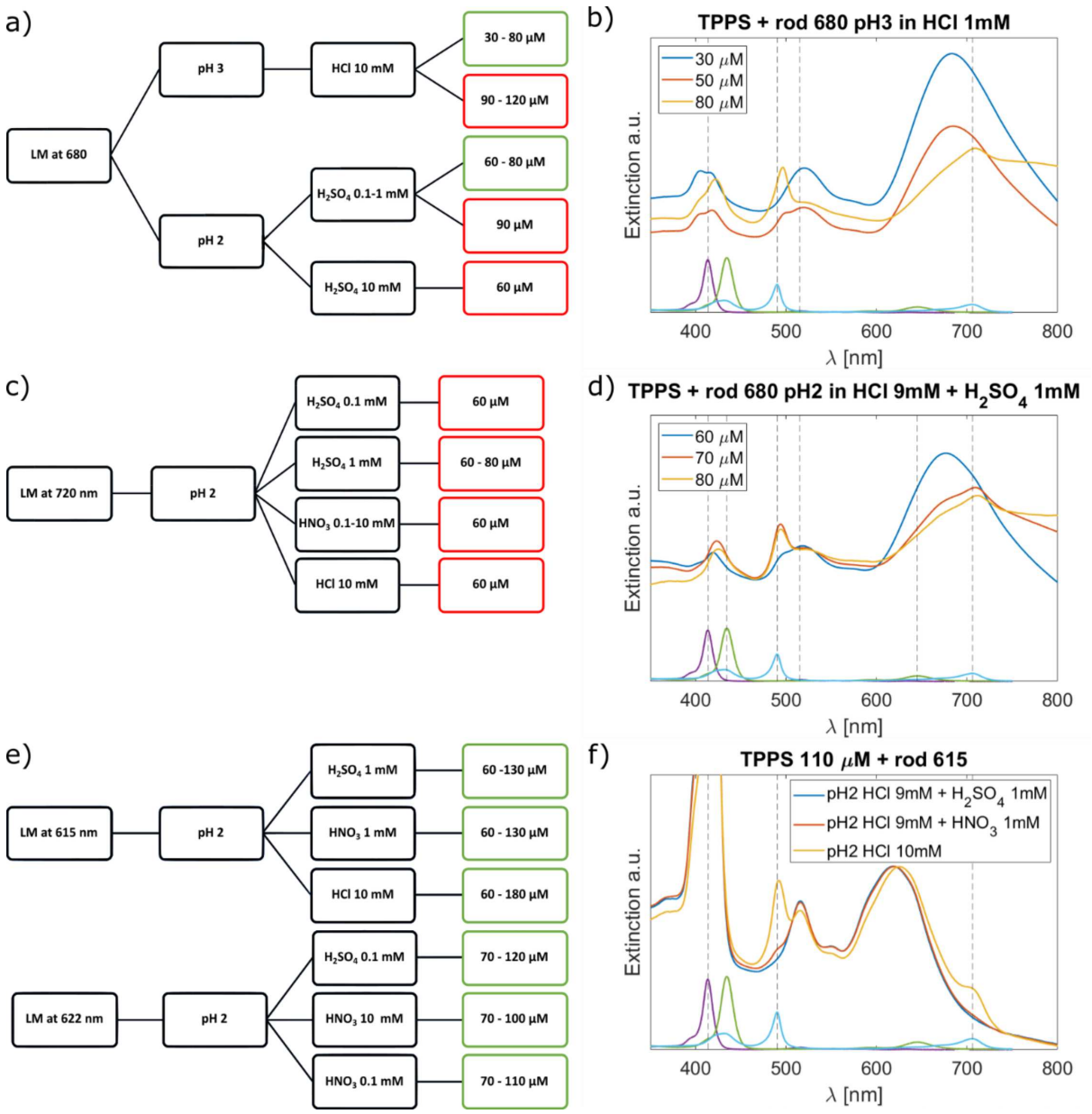

Figure 3.3 *a), c), e) Schemes summarizing some of the tests made with TPPS and gold NRs. In each scheme, the first cell indicates the peak position of the LM of NRs, the second cell indicates the pH, the third group of cells indicates the concentration of anions (Cl^-, SO_4^{2-}, NO_3^-), and the last group of cells indicate the range of concentration of TPPS explored. The red (green) color indicates the precipitation (stability) of NRs. b), d), f) Extinction spectra of some relevant samples, compared with the spectra of m-$TPPS^{4-}$, m-H_2-$TPPS^{2-}$ and a-H_2-$TPPS^{2-}$ (purple, green and light blue, respectively).*

As stated, we found that lower acidity (pH ~ 3), as well as the presence of competitor anions, hampers the NRs aggregation. In these conditions, NRs are stable until a TPPS concentration of about 80 µM (figures 3.3b and d). However, also in these cases, there is no clear evidence of SC between TPPS and the LM of the particle. Nevertheless, it is worth noting that, in the TM region (500-550 nm, figures 3.3b and d), there is a feature that resembles the concentration

trend of a plexcitonic system (UP and LP peaks which move away from each other as the dye concentration increases). However, it is difficult to unequivocally establish if these signals effectively originate from an interaction between the TM and the J-band at 490 nm or if they consist of a mere sum of the spectra of the non-interacting species. A plexciton formed by the coupling with the transverse mode of metallic NRs has not been observed yet. Thus, this aspect could be of great interest and further investigation will be done.

As we expected, we also noticed that the aspect ratio has a major influence on NRs aggregation. In fact, NRs with LM peak at 720 nm aggregate and precipitate at low concentrations of TPPS, despite the presence of counterions (figure 3.3c). Instead, shorter NRs are stable also at high TPPS concentrations (figures 3.3e and f). However, no SC was observed again. The strong signal at 417 nm (figure 3.3f) is the same signal observed in a water solution of only TPPS and CTAB. In fact, that batch of NRs was obtained through the oxidation step of longer NRs (section 2.3.1), thus they were dispersed in a water solution of CTAB 15mM. This suggests that the CTAB concentration also plays a fundamental role as it can interact with the porphyrin molecules. Not only the concentration, but also the nature of the capping layer affects the supramolecular interactions between the NPs and the porphyrin molecules.[74] Thus, further tests should be done using different capping layers.

3.1.3 Final remarks about porphyrin-based nanohybrids

In conclusion, while with gold spherical NPs, SC with TPPS can be easily reached,[68] no plexcitons formation was observed with gold NRs. It is obvious that in our experiments we explored a very limited space of all the possible supramolecular conditions. However, we learned that hybrid systems based on TPPS and gold NRs require a high control over the chemical parameters to grant their stability, thus more efforts are needed to reach the SC condition. It is important to mention that the coupling may also be hampered by an unfavorable relative orientation of dipoles. The transverse and longitudinal plasmons oscillate along the transverse and longitudinal directions (section 1.2.2, figure 1.10). If the porphyrin molecules aggregate on the surface so that their dipole transitions are orthogonal to the plasmon oscillations, there is no way to achieve a coupling. Therefore, morphological studies of porphyrins aggregated on metallic NPs could also be helpful to drive new attempts.

3.2 Cyanine-based nanohybrids

On a second attempt, we shifted our focus to cyanines. Compared to porphyrins, cyanines have less complex absorption spectra that consist of one main band and, in some cases, its vibronic progression. This class of dyes easily forms J-aggregates with very narrow and intense bands, and there is plenty of examples of cyanine-based plexcitons in the literature.[7,56,74–77] Thus, two different cyanines (5,5′,6,6′-Tetrachloro-1,1′,3,3′-tetraethylbenzimidazolocarbocyanine iodide (JC-1) and 1,1-diethyl-2,2-cyanine iodide (PIC)) were selected for the realization of the nanohybrids.

3.2.1 Sample preparation and UV-Vis characterization

3.2.1.1 Bare gold nanorods and J-aggregates

PIC (figure 3.4a) is a cationic cyanine that exists as a monomer in ethanol (ε_{max} estimated to $8.0 \cdot 10^4$ $cm^{-1}\,M^{-1}$ at 524 nm) and forms J-aggregates in water solution upon addition of sodium chloride salt and heating. The resulting J-band is very intense and narrow and centered at 574 nm (figure 3.4c). Through analysis of extinction spectra, the FWHM was estimated to be about 18 meV. Similarly, JC-1 (figure 3.4b) is a cationic carbocyanine dye that exists as a monomer at low concentrations in ethanol with a very high molar extinction coefficient (ε_{max} estimated to

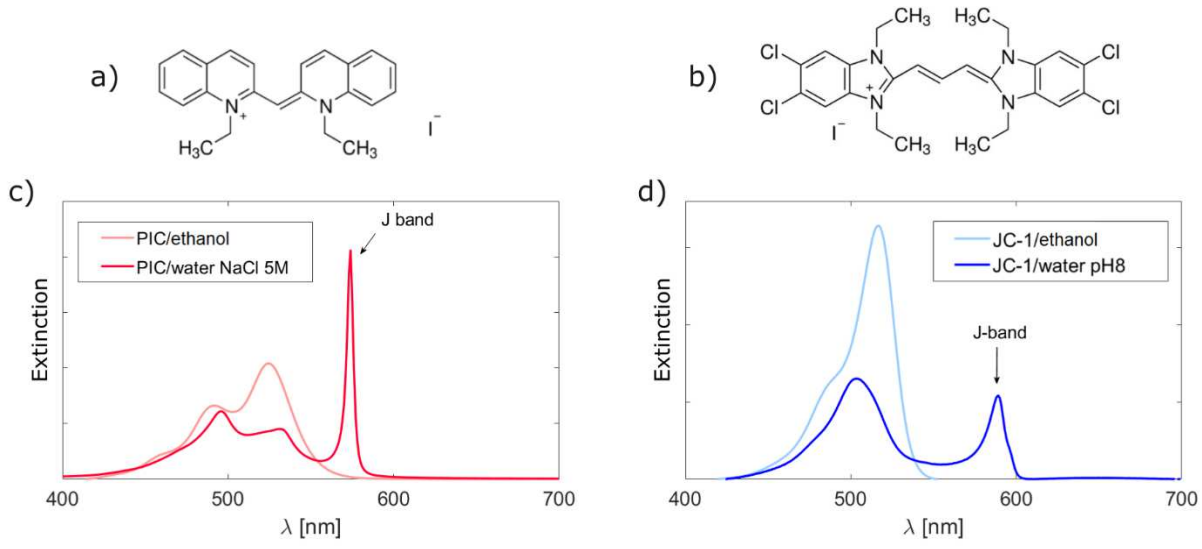

Figure 3.4 *Molecular structure of a) PIC and b) JC-1. Extinction spectra of monomer and aggregate forms of c) PIC and d) JC-1.*

$2.4 \cdot 10^5$ cm^{-1} M^{-1} at 517 nm). In water solution, the dye is less soluble and, upon addition of an ammonium salt, it forms J-aggregates that exhibit a narrow band at 590 nm (figure 3.4d). Through analysis of extinction spectra, the FWHM was estimated to be about 46 meV.

To achieve SC, gold NRs with the LM nearly resonant with the J-band of the dyes were prepared as described in section 2.3.1. The extinction spectra of the obtained NRs are shown in figure 3.5. The longitudinal plasmon of the NRs synthesized is centered at 585 nm with a FHWM estimated to be about 222 meV.

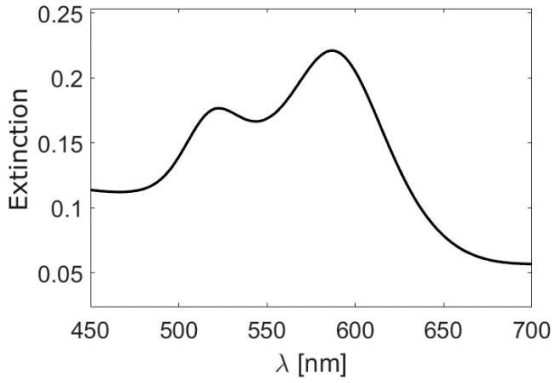

Figure 3.5 *Extinction spectra of bare gold NRs utilized for the hybrids' synthesis.*

3.2.1.2 Plexcitonic nanohybrids

Several samples have been prepared slightly changing the experimental conditions. These samples have been labeled as **_hy_n, where the first letters indicate the dye (PI for PIC, JC for JC-1 and MIX for the mix of the two dyes) and the final number n indicates the progressive sample number. All the samples and the associated experimental conditions are summarized in table 3.1. The first two samples were prepared as follows: small volumes of the dye solution were progressively added to an aqueous solution containing gold NRs (in the presence of ammonium for JC-1). The spectra were recorded after 20-30 min after each addition (figure 3.6). Others plexcitonic nanohybrids were prepared by simply adding the final volume of dye solution to the NRs solutions. The formation of strongly coupled plexcitonic nanohybrids is proven by the formation of two new hybrid plexcitonic states (LP and UP) manifested by the appearance of a dip in the broad plasmon resonance (section 1.1). This dip is the clear manifestation of an avoided crossing point (section 1.1.1, figure 1.2), whose position in

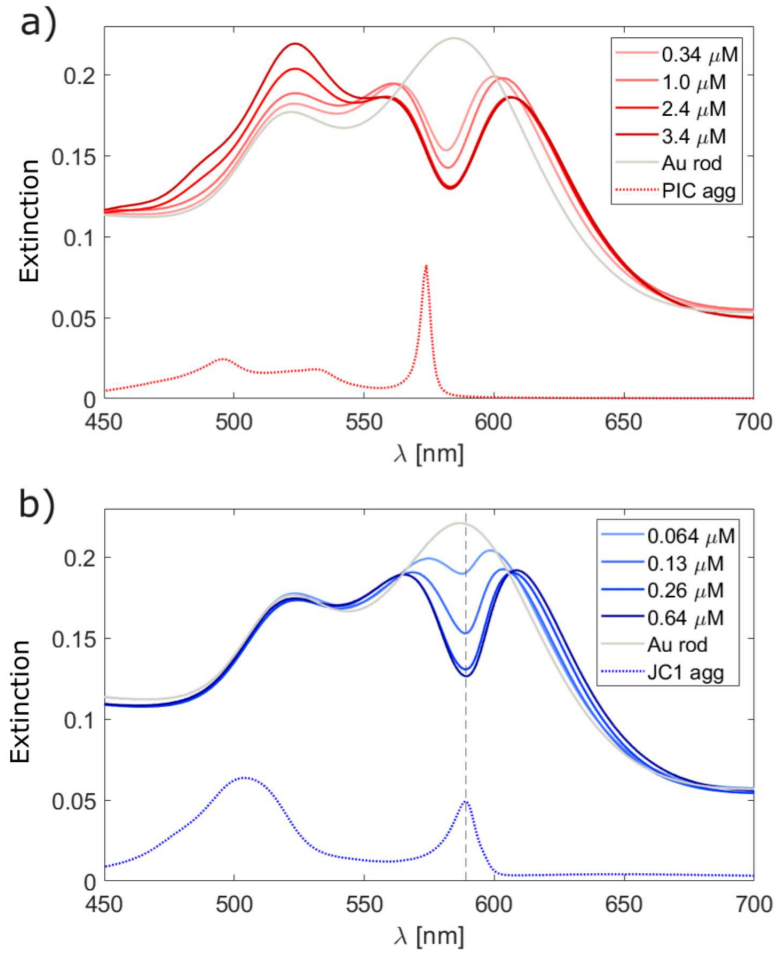

Figure 3.6 *Extinction spectra of aqueous gold NRs before (grey) and after the addition of different amounts of a) PIC (red) and b) JC-1 (blue). The legend reports the final concentration of the dye added to the water solution of gold NRs. The spectra are compared with the respective spectra of the aggregated dyes (dotted lines). These sample are named PI_hy_1 and JC_hy_1, respectively.*

wavelength corresponds with the J-aggregate excitonic resonance (some deviations are a consequence of the detuning δ between plasmon and excitonic resonances). The distance in energy between the two newly formed peaks can be used to estimate the Rabi splitting Ω_R (Chapter 1). From the collected spectra of JC_hy_1 and PI_hy_1, it is clear that the Rabi splitting, and thus the coupling strength, can be easily tuned by changing the concentration of the dye. In fact, as described in section 1.1.3, the coupling strength is proportional to the square root of the number of molecules. Actually, the coupling strength does not increase indefinitely, but it reaches a maximum. This can be physically interpreted as the saturation of the NPs' mode volume by the molecules. The signal at 524 nm in the PI_hy_1 spectrum indicates the presence of PIC also in the monomeric form; this is also observed before reaching the maximum Rabi splitting. This is because the PIC in water still exists as monomer and would aggregate only in the presence of high concentrations of salt after heating. This suggests that there is a dynamic

equilibrium between the monomeric PIC and the PIC aggregated on the particle's surface. On the other hand, the same equilibrium for the JC-1 seems to be entirely dominated by the dye aggregated on the particle surface as no signal of monomer is observed.

Table 3.1 *List of all the plexcitonic nanohybrids prepared and characterized in this Thesis. These samples are named JC_hy_n, PI_hy_n and MIX_hy_n, where PI, JC and MIX indicate the dyes (PIC, JC-1 and a mixture of both, respectively) and n the number of the sample. The table reports relevant parameters for solutions of the uncoupled components (Au NRs and dyes) and the resulting plexciton nanohybrids.*

NAME	Au rod		Dye		Plexcitons		
	LM [a] [nm (eV)]	LM ext. [b] (l = 2mm)	PIC [c] [μM]	JC-1 [c] [μM]	UP [d] [nm (eV)]	LP [d] [nm (eV)]	Ω_R [e] [meV]
JC_hy_1	585 (2.11)	0.22	–	0.64	564 (2.20)	611 (2.03)	169
JC_hy_2	585 (2.11)	0.22	–	0.64	562 (2.21)	609 (2.04)	170
JC_hy_3	585 (2.11)	0.58	–	2.3	561 (2.21)	609 (2.04)	174
PI_hy_1	585 (2.11)	0.22	3.4	–	558 (2.22)	608 (2.04)	181
PI_hy_2	585 (2.11)	0.22	1.7	–	561 (2.21)	604 (2.05)	156
PI_hy_3 [f]	573 (2.16)	0.64	8.7	–	550 (2.25)	592 (2.09)	160
PI_hy_4 [f]	573 (2.16)	0.67	5.4	–	553 (2.24)	587 (2.11)	130
MIX_hy_1	585 (2.11)	0.22	2	0.38	563 (2.20)	610 (2.03)	170
MIX_hy_2	585 (2.11)	0.22	1.4	0.45	557 (2.21)	607 (2.04)	183
MIX_hy_3	585 (2.11)	0.58	3.3	1.2	561 (2.21)	608 (2.04)	171

[a] wavelength (energy) of the longitudinal plasmon (LM) of the rods; [b] extinction value of the LM (in an optical path l=2mm), used as a parameter to quantify the concentration of NPs; [c] final concentration of the dyes in solution; [d] wavelength (energy) of the resulting upper plexciton (UP) and lower plexciton (LP); [e] Rabi splitting, obtained from $\Omega_R = 2g$ with g obtained through eq. 1.11 (the Rabi splitting for the MIX_hy_n samples was estimated simply as the energy difference between UP and LP). [f] PI_hy_3 and PI_hy_4 were prepared using a different solution of gold NRs with the LM resonant with the J-band of PIC aggregates.

The SC condition of plasmon-exciton coupling can be estimated through the FHWMs. In fact, neglecting the contribution of inhomogeneous broadening, it is verified that (section 1.1.1):

$$FWHM = 2\gamma \ \ (2k) \tag{3.1}$$

While this assumption is almost valid for the J-bands,[35,36] the inhomogeneous broadening could not be neglected in the extinction spectra of metallic NPs. In these conditions, eq. 3.1 leads to

an overestimated plasmon dissipation rate k, and then an overestimation of the SC condition (right side of eq. 1.22b). This implies that we are applying more restrictive conditions to decide if the prepared nanohybrids fulfill or not the SC regime. Under these premises, putting together equations 1.22b and 3.1, the SC conditions for PIC (JC-1)-based plexcitons are: $\Omega_R > 120\ (134)\ meV$. The values estimated for Ω_R and reported in table 3.1 confirm that even using an overestimated value of k, SC conditions are largely fulfilled for all the plexcitonic nanohybrids.

3.2.1.3 "MIX" plexcitonic nanohybrids

After the realization of PIC and JC-1 based plexcitons, we prepared "MIX" hybrid plexcitons by adding a mixture of PIC and JC-1 to an aqueous solution containing gold NRs. We wanted to determine if the optical properties of the mixed plexcitons are different from those of PIC and JC-1 plexcitons or if the behavior is just additive. The motivation was to understand if it is possible to modulate the optical properties with multi-dye systems and prove how versatile and tunable a plexcitonic nanomaterial could be. The extinction spectrum of a mixed plexciton sample, compared to those of PIC and JC-1 plexcitons, is shown in figure 3.7. Firstly, we confirmed the plexcitons formation, as evidenced by the splitting of the longitudinal plasmon into two new bands due to hybrid states. The maximum splitting observed in mixed plexcitons is comparable to that observed for the other plexcitons (table 3.1). Moreover, it can be observed that the dip of the mixed plexciton is located in an intermediate position with respect

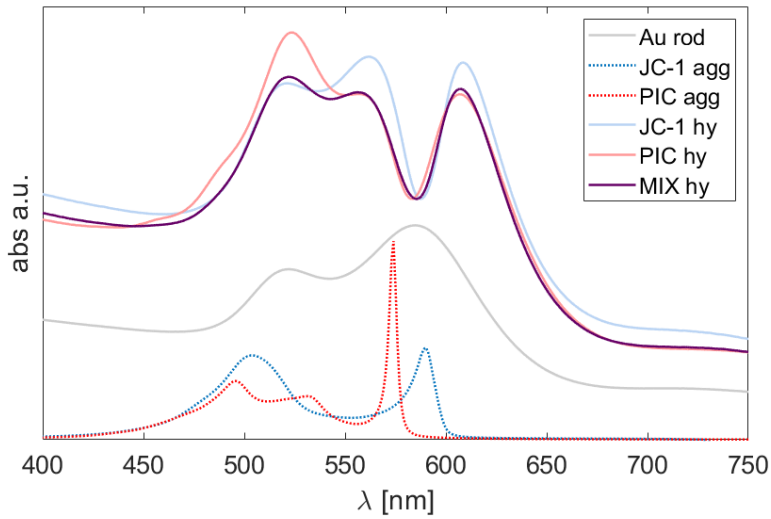

Figure 3.7 *Extinction spectra of the mixed plexciton MIX_hy_2 (purple), compared with JC_hy_2 (blue solid line) and PI_hy_1 (red solid), the bare gold NRs (grey), and JC-1 (blue dotted) and PIC (red dotted) aggregates.*

to the dip of PIC and JC-1 plexcitons. However, we verified that this feature is kinetically unstable since the dip tends to move towards the JC-1 dip position, reaching the same value in a few days. Another interesting observation is that the signal relative to the monomeric PIC decreases. This observation suggests that the JC-1 may facilitate the aggregation of the PIC on the particle's surface. In fact, we believe that the MIX plexciton originated from the interaction of the plasmon with a mixed aggregate, where PIC and JC-1 molecules are blended and interact together. Therefore, we think that this MIX plexciton is in all respects different from the other two plexcitons, with its own spectral features, not originated from the simple coexistence of different domains of non-interacting PIC and JC-1 plexcitons. This hypothesis is also supported by nonlinear measurements reported in section 3.3.

3.2.2 Circular Dichroism

Optically active plexcitons have recently been reported in the literature and investigated experimentally and theoretically.[78–85] It was observed that when chiral aggregates are placed near an achiral metal nanostructure, the plasmon-exciton interactions have a profound impact on the CD response of the hybrid system. This impact is reflected mainly in the following two aspects: (i) generation of a CD response termed as induced plasmonic CD at the achiral metal nanostructure resonance and (ii) enhancement of the CD of the chiral J-aggregate. The induced plasmonic CD phenomenon has aroused greater interest because it indicates that the plasmon-exciton interaction provides an effective mechanism for achiral plasmonic structures to obtain optical activity. Thus, also the formation of chiral plexcitons in suitable conditions is expected to induce new interesting optical behaviors. Therefore, systematic research on the optical chirality of plexcitonic systems in the SC regime is very promising, also in view of interesting new practical applications.

Thus, with the aim of obtaining more information about possible chiral properties of our systems, we performed CD measurements of PIC, JC-1 and MIX plexcitons and the aggregated dyes as reference.

The investigation of the chiral properties of J-aggregates of organic dyes is *per se* a highly debated and still not fully understood matter.[86,87] Although both PIC and JC-1 are non-chiral molecules, it is known that they can give rise to supramolecular chiral arrangements under

certain experimental conditions, for example by adding a chiral templating agent.[88–91] Indeed, the J-aggregates have been proposed to assume a helicoidal cylindrical structure.[92] The CD spectrum results from the chiral arrangement of the transition dipoles and not from an intrinsic chirality of the molecules. This type of CD effect is described in the literature as excitonic chirality.[93,94] The CD spectra of the J-aggregates of PIC and JC-1 are shown in figures 3.8a and b, respectively. A non-negligible CD signal was measured in both cases, despite no chiral templating agents being added.

This is a known feature for helical aggregates of cyanines explained by the assumption that the enantiomeric symmetry is broken. Indeed, when achiral molecules aggregate in chiral supramolecular helicoidal structures, right- and left-handed aggregates are present in approximately identical fractions. For example, for PIC J-aggregates, cryo-TEM images and electron diffraction[92] confirmed that these molecules form thread-like aggregates with a diameter of 2.3 nm. The molecules are arranged in a 1:1 ratio of left-and right-handed twist giving a symmetric racemic mixture. Therefore, one must assume that the CD signal is caused by a slight excess of one of the enantiomers. The large statistical fluctuations of sign and magnitude of the CD signal for different samples of aggregates (two examples are reported in figures 3.8a and b) strongly support the assumption of an unspecified enantiomeric excess. This behavior was also observed for other cyanine aggregates.[95] Up to date, the reason for the symmetry break is not understood, but it seems to be a typical feature of the tubular aggregates. One explanation could be given based on nucleation and growth kinetics of the aggregates.[86,88]

Figures 3.8c and d show the CD spectra of the plexcitonic species. We did not observe the effect of enhancement of the CD signal of the original J-aggregates, but completely different features were recorded. A weak signal, in correspondence of LP and UP wavelength, was observed, and its bisignate line shape agrees with the few available literature works.[78,79] Indeed, mode splitting and anticrossing behavior were found in CD spectra, which are a clear signature of optical chirality hybridization. In both PIC and JC-1 plexcitons, the CD response exhibited a smaller mode splitting than the corresponding extinction response, also in this case, in agreement with previous evidence.[79] It has been suggested that the mode splitting in the CD spectrum can be attributed to the strong plasmon–exciton coupling. Moreover, since the bisignate line shape of the CD response makes it easier to distinguish the hybrid modes, this

splitting could be used for more reliable quantification of the SC conditions, similarly to the procedure used for excitonic systems.[79]

In the plexcitonic samples, we did not observe fluctuations in sign and magnitude of the CD signal, which is weak but reproducible among different samples. This might suggest that the aggregates assume well-defined geometries around the surface of the NRs. This agrees with the recent observation that the chirality of nanohybrids is related to the specific distribution of

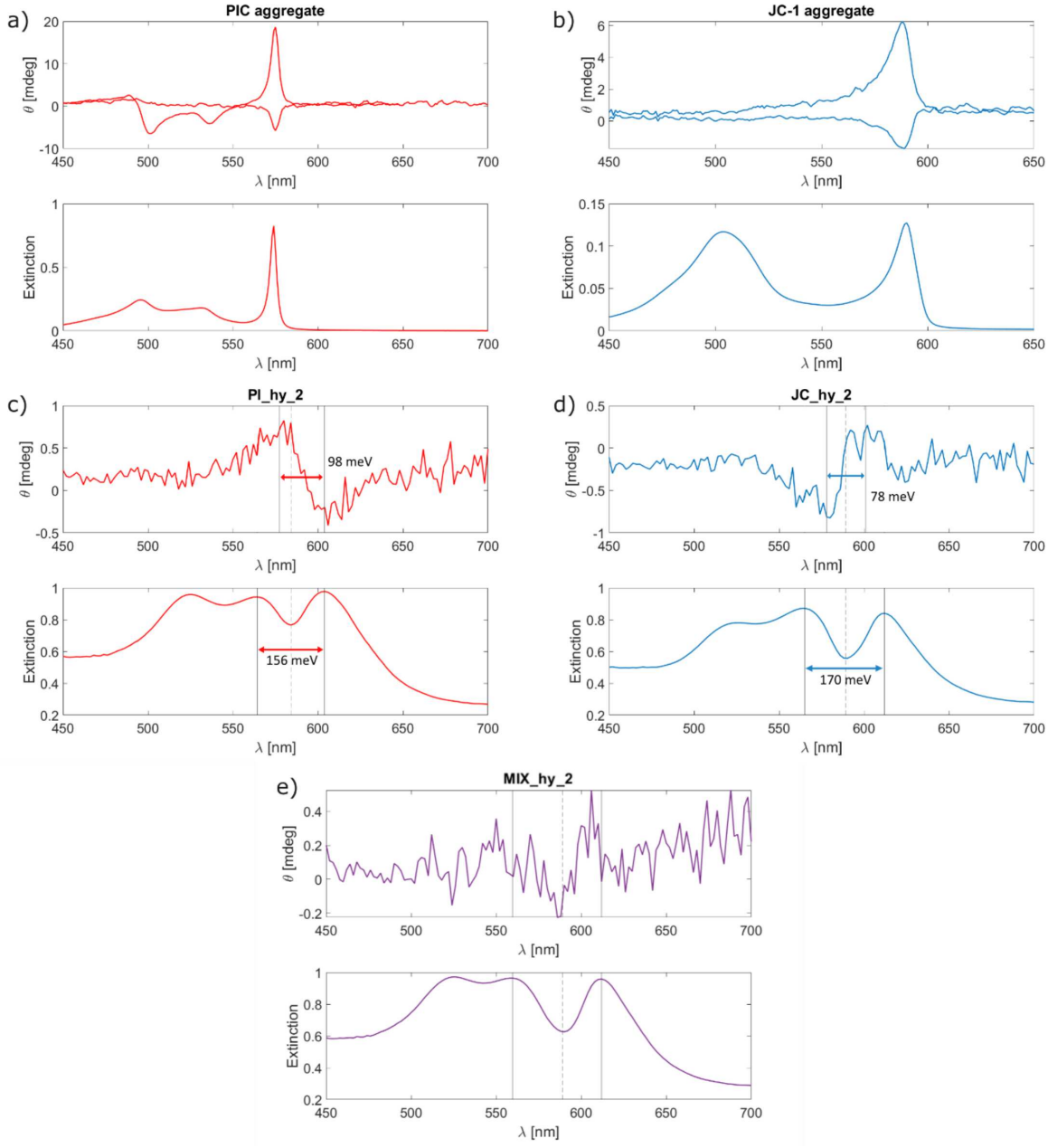

Figure 3.8 *Extinction and CD spectra of a) PIC J-aggregate, b) JC-1 J-aggregate, c) PI_hy_2, d) JC_hy_2 and e) MIX_hy_2.*

the dye aggregates in different positions of the NRs (the J-aggregates assembled on both ends and both sides of the NRs had opposite chirality).[78]

Finally, comparing the spectral features of the PIC, JC-1 and MIX plexcitonic nanohybrids, it can be noticed that the MIX shows a weaker signal and most likely a different pattern. Although the signal is too weak to make more quantitative considerations, this finding seems to support our hypothesis that the MIX plexciton is a new plexciton with different proprieties than the PIC and JC-1 plexcitons.

3.2.3 Final remarks about linear characterization

In this section, we employed linear spectroscopies to confirm the strong plasmon-exciton coupling formation between Au NRs and J-aggregates of PIC and JC-1. Plexciton formation was confirmed by the splitting of the longitudinal plasmon resonance into two new hybrid states, and by the concentration dependence of the energy separation between these states. In addition, we investigated the nature of the new MIX plexciton. UV-Vis and CD spectra suggest that the mixed plexciton is a new plexciton with different properties than the PIC and JC-1 plexcitons, and that this could be a consequence of the distribution of the dyes on the surface of the NRs. In fact, we think that the MIX plexciton originates from the interaction of the plasmon with a mixed J-aggregate, where PIC and JC-1 molecules interact together. However, these preliminary analyses are insufficient to discriminate this hypothesis from the coexistence of different domains of non-interacting PIC and JC-1 plexcitons. Thus, more advanced characterizations, such as nonlinear spectroscopy, are needed to give more consistent evidence. Furthermore, we also checked the chiral response of the plexcitons by CD spectroscopy, inspired by recent studies that suggested a broader range of exciting applications for optical chirality in plexciton nanohybrids. While further investigations must be performed to achieve better spectra, our preliminary results are very promising and indicate optical chirality as a new powerful tool for further exploitation of the SC regime.

3.3 Nonlinear optical characterization of cyanine-based nanohybrids

A brief overview on plexcitons and polaritons dynamic was made on section 1.2.3. In an attempt to provide additional information to the still puzzling issue of plexciton dynamics, one of the aims of this Thesis is to characterize and compare the dynamics of the plexcitonic nanohybrids obtained with different cyanines. This was achieved by measuring the TA spectra by pump-probe spectroscopy. However, to properly understand the plexcitons dynamic behavior and to identify the features emerging only upon the establishment of SC between the NRs and the molecular dyes, the preliminary study of the dynamic behavior of the uncoupled species (NRs and molecular J-aggregates) in the same experimental conditions was necessary. These data were taken as a reference for the investigation on plexciton systems.

3.3.1 Optical nonlinearities of PIC and JC-1 J-aggregates

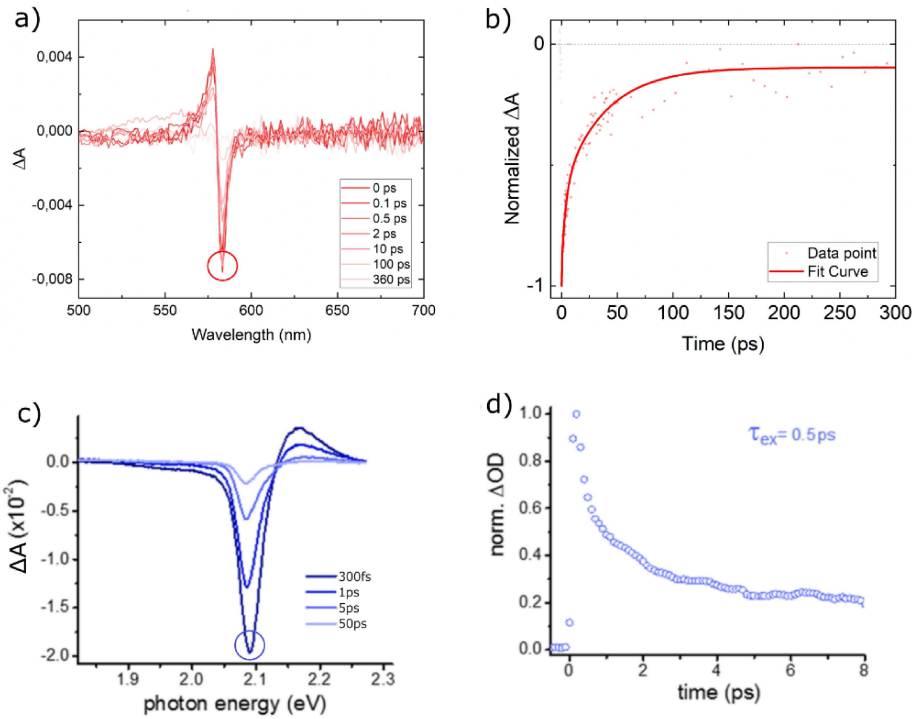

Figure 3.9 *Characterization of the ultrafast dynamics of the J-aggregates of the considered molecules. Panels a and b depict the experimental results obtained in this Thesis on PIC J-aggregates, while panels c and d reports literature results measured on JC-1 aggregates (adapted from ref [56]). a) TA spectra of PIC J-aggregates at different values of delay times. b) Signal decay extracted at a probe wavelength of 583 nm, pinpointed by the circle in panel a. c) TA spectra of JC-1 J-aggregates at different values of delay times. d) Signal decay extracted at a probe wavelength of 590 nm, pinpointed by the circle in panel b. Notice that signal is normalized at a positive value*.

TA spectra of the PIC J-aggregated were collected and the results are shown in figure 3.9a, while figure 3.9b shows the signal decay extracted at 583 nm, corresponding to the position pinpointed by the circle in panel a. The pump pulse was centered at 400 nm with a fluence of 169 μJ/cm^2. The TA spectra of the JC-1 J-aggregated could not be collected in this work because of photostability problems of the dye in our experimental conditions. Therefore, we show in figures 3.9c and d the data found in literature.[56] In that work the authors performed pump-probe measurements with a pump pulse at 2.1 eV (590 nm, resonant to the J-band) with a fluence of ca. 17 μJ/cm^2, which is ten times smaller than that in our experiments.

Both PIC and JC-1 J-aggregates show the same nonlinear features: a strong GSB in proximity of the J-band (583 nm / 2.13 eV for PIC and 590 nm / 2.10 eV for JC-1), and a blue shifted ESA (578 nm / 2.15 eV for PIC and 571 nm / 2.17 eV for JC-1). These phenomena can be easily rationalized as follows:

(i) The excitation pulse populates the one-exciton state, therefore, within the one-exciton lifetime, the transition probability to this state reduces and the transmission in the corresponding spectral region increase (GSB).

(ii) Additionally, a two-exciton state can be reached from the one-exciton state upon interaction with the probe pulse, thus the differential absorption is enhanced (ESA). Typically, ESA in J-aggregates lies at higher energies than the GSB energy.[96]

The study of the differential absorption as a function of the delay time allows investigating the relaxation kinetics of the exciton states. The dynamics of the GSB of the PIC has been fitted using a three-exponential decay model, neglecting the first 100 fs to exclude pulse overlap effects:

$$\Delta A = \Delta A_0 + A_1 e^{-\frac{t}{\tau_1}} + A_2 e^{-\frac{t}{\tau_2}} + A_1 e^{-\frac{t}{\tau_3}} \qquad (3.2)$$

with ΔA_0 the background value at $t \to \infty$, A_i the pre-exponential factors and τ_i the time constants. The time constants obtained are shown in table 3.2.

Table 3.2 *Time constants resulting from the data fitting (figure 3.1b), with the associated errors.*

	τ_1 (ps)	τ_2 (ps)	τ_3 (ps)
PIC	$\leq 0{,}150$ *	$3{,}9 \pm 0{,}7$	38 ± 4

**Non quantifiable because comparable to the pump pulse duration.*

The first fast decay time is not quantifiable in our experimental conditions because in many measurements it falls at times comparable to or shorter than the pump pulse duration (< 150 fs). The associated process can be identified and ascribed to the ultrafast relaxation of two-exciton states following the photoexcitation at 400 nm.[97,98] The second time constant of a few picoseconds is attributed to the exciton-exciton annihilation process [97–99] and the third one can be ascribed to the exciton lifetime of the PIC J-aggregated.[96,100–102]

According to the data published in ref [56] and reported in figures 3.9c and d, the dynamics of JC-1 J-aggregates is similar to the other cyanine. The decay of the GSB signal has been fitted with a two-exponential model, but only the value of the first fast decay was reported (estimated at about 0.5 ps (figure 3.9d)). The lack of more precise information in the literature about JC-1 aggregates nonlinearities did not allow us to rationalize this fast decay and to say more about the others contributes. In any case, a thorough interpretation of the relaxation dynamics of JC-1 aggregates goes beyond the scope of this Thesis. Here, we are just interested in knowing their qualitative time-dependent behavior for a comparison with the plexciton dynamics.

3.3.2 Optical nonlinearities of gold nanorods

The nonlinear response of gold NPs is governed by the damping mechanisms of plasmons (section 1.2.2). Dephasing of the plasmon resonance deposits energy into the electron distribution, creating excited electrons, that are spread over different levels in the conduction band. These excited electrons dissipate energy into the electron gas increasing its temperature. This is followed by a rapid thermalization between electron and phonon gas. Finally, the entire particle exchanges energy with the surrounding medium. Energy can also be deposited into the electron distribution by exciting the interband transitions instead of directly exciting the plasmonic resonance.[103,104] The threshold energy for interband transitions is about 2.4 eV for Au.

We performed pump-probe measurements of bare gold NRs with λ_{max} at 585 nm. The excitation pulse was set at 400 nm, where the interband transitions of Au bulk occur, and with a power density of 170 $\mu J/cm^2$. Figure 3.10a shows the TA spectra at different delay times after the pump, while in figure 3.10b the corresponding bidimensional representation is illustrated.

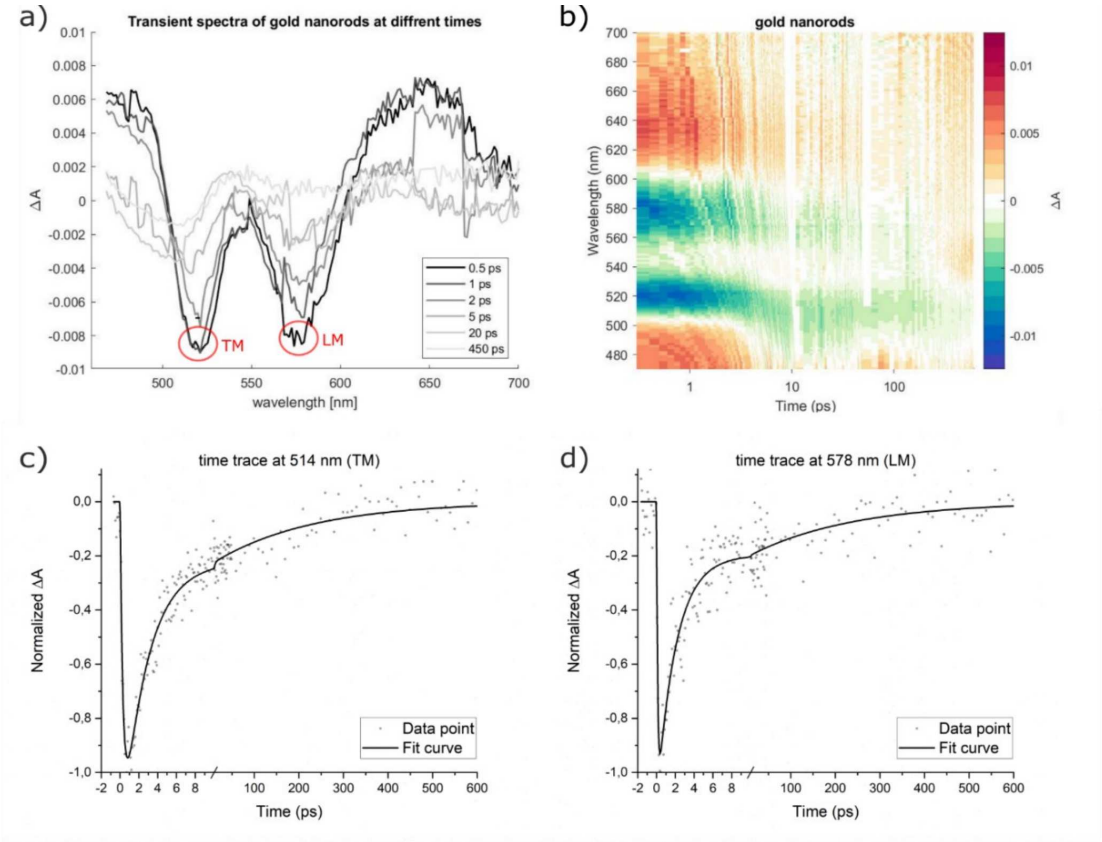

Figure 3.10 *a) TA spectra of bare gold NRs at different delay times. b) Colormap of transient spectra of gold NRs. (c-d) Time traces extracted at wavelengths corresponding to the transverse and longitudinal peaks. Notice the break in the time axis at 10 ps.*

For any delay time, the differential absorption is negative in the spectral range of both plasmon resonances (TM and LM at 514 and 578 nm, respectively). The positive signal at higher wavelengths, around 650 nm, could be a consequence of the excitation at the interband transitions. In fact, this phenomenon is generally observed only in pump-probe experiments with pump energy above the threshold energy for interband transitions.[104] This could also explain the small blue shift observed at the LM signal (figure 3.10b).

When commenting the origin of the signals appearing in the TA spectra of plasmonic NPs, it should be stressed that, strictly speaking, the negative signals at the TM and LM spectral positions are not entirely attributable to GSB. Indeed, plasmons refer to collective oscillations of the conduction electrons and therefore it is not entirely correct to speak about “ground” and “excited states” like for molecular samples. The nonlinearities giving rise to such negative signals has been explained mainly by the increase of the homogeneous linewidth as a consequence of the increase of temperature of the electron gas promoted by the pump excitation.[56]

However, there is an analogy between this nonlinear effect and the GSB of molecular systems. In fact, both phenomena give rise to similar response and are associated to a relaxation phenomenon. In the molecular case the relaxation is a recovery of the ground state population, while, in the metal NP the relaxation is the thermalization of the particle to the equilibrium conditions. Therefore, for simplicity, when we will discuss the nonlinearities of plexcitonic states, which are states with a mixed plasmonic and molecular character, we will adopt the "molecular" terminology, that is GSB, ESA or SE, with the awareness that the phenomena associated could have a different origin.

Figures 3.10c and d represent the time traces extracted at the two different peaks, the TM and the LM, respectively. With little differences, the two dynamics are comparable and show the same trend: the signal rises to its maximum value within the first 500 fs, then it decays with two different time constants of the order of 2-3 ps and 200-300 ps. These dynamics are compatible with the damping mechanism already documented in the literature and discussed above.[12] Therefore, the traces have been fitted with an equation that reflects the nature of this relaxation mechanisms:[103]

$$\Delta A = \Delta A_0 + A_1 \left(1 - e^{-\frac{t}{\tau_{e-e}}}\right) e^{-\frac{t}{\tau_{e-ph}}} + A_2 \left(1 - e^{-\frac{t}{\tau_{e-e}}}\right) e^{-\frac{t}{\tau_{ph-env}}} \qquad (3.3)$$

with ΔA_0 the background value at $t \rightarrow \infty$, and A_i the pre-exponential factors. As described in section 1.2.2.2, the three time constants (i) τ_{e-e}, (ii) τ_{e-ph}, and (iii) τ_{ph-env} are related to: (i) electron-electron scattering,[12] which takes place after the plasmon resonance dephasing, and which enhances the electron gas temperature; (ii) electron-phonon scattering,[105,106] which describes the electron thermalization; (iii) phonon-environment interaction,[105,106] that is the heat dissipation process. This model is called raise-decay-decay (RDD) because a raising exponential is convoluted to the sum of the exponential decays. To obtain more robust results, the fitting was performed with a global procedure, by fitting simultaneously the time traces at wavelengths around the peak position with shared time constants. The results are shown in table 3.3

Table 3.3 *Time constants resulting from the fitting of the traces at the TM and LM peaks of gold NRs (figures 3.10c and d), with the associated errors.*

	τ_{e-e} (ps)	τ_{e-ph} (ps)	τ_{ph-env} (ps)
TM	$0{,}34 \pm 0{,}02$	$2{,}58 \pm 0{,}10$	222 ± 34
LM	$0{,}11 \pm 0{,}02$	$1{,}99 \pm 0{,}10$	233 ± 22

3.3.3 Optical nonlinearities of plexcitons

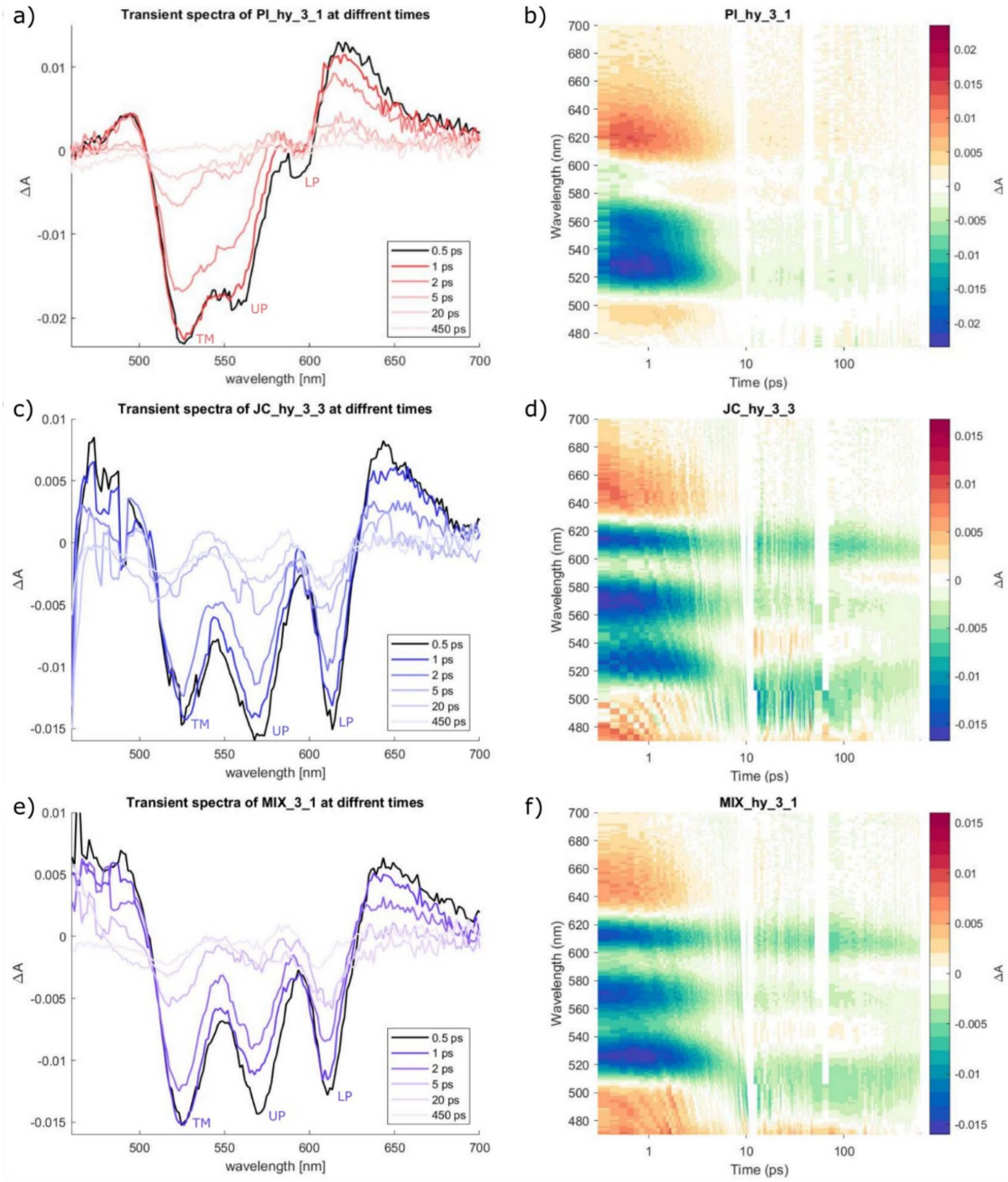

Figure 3.11 *a), c), e) The transient spectra at different delay times of PI_hy_3_1, JC_hy_3_3 and MIX_hy_3_1 respectively, and b), d), f) the associated 2D colormaps.*

We performed pump-probe measurements of PIC, JC-1, and MIX plexcitons. Considering that we prepared different replicas of the same sample and on each of them different repetitions of the pump-probe measurement were recorded, I will refer to these samples with the acronyms PI_hy_n_m, JC_hy_n_m and MIX_hy_n_m, respectively, with n the number of the

sample and m the number of the measure on that sample. For a detailed description of the sample preparation see section 3.2.1, table 3.1. Below we report the result of the more significant samples. All this samples fulfil the SC conditions. JC_hy_3 and MIX_hy_3 were prepared with the same Au NRs used as reference, with the LM nearly resonant with the JC-1 J-band. Instead, PI_hy_3 and PI_hy_4 were prepared with a different Au NR, with the LM nearly resonant with the PIC J-band. The measure was done with a pump pulse power density around 170 μJ/cm^2 (184 μJ/cm^2 for PI_hy_3) and centered at 400 nm. The transient spectra and the respective 2D colormaps of some samples are illustrated in figure 3.11. All the samples show a negative signal in proximity of the TM, UP and LP bands, with some differences in the relative intensity. Using the molecular terminology commented above, these signals can be identified as due to the GSB of the corresponding transitions in the linear extinction spectra. In addition to this, there are two positive signals at wavelength red-shifted from the LP and blue-shifted from the TM.

Firstly, we focused on the GSB signals and their dynamics. At a first sight, these dynamics resemble those of the pristine NRs, i.e., a fast rise with a time constant of the order of 0.1-0.4 picoseconds, a first decay of a few picoseconds and a longer decay with a constant of hundreds of picoseconds. The behavior at early times (<10 ps) is similar to the one found for the NRs samples (see table 3.3). This is not surprising considering that the experiments have been performed in "off-resonance" excitation conditions, where the pump wavelength, set at 400 nm, predominantly directly excites the *sp*-to-*d* bulk interband transition of gold NRs. Therefore, we hypothesized, under the current experimental conditions, that the ultrafast dynamics of plexcitons in the first 10 ps are more "plasmon like", while the response on the longer timescale (>10 ps) is more peculiar of plexcitonic samples.[54] Therefore, as a first attempt, we try fitting the GSB time traces using the same RDD model used for bare NRs, paying most attention to the longest time constant, that we labelled as τ_{plex}. The fitting model becomes:

$$\Delta A = \Delta A_0 + A_1\left(1 - e^{-\frac{t}{\tau_{e-e}}}\right)e^{-\frac{t}{\tau_{e-ph}}} + A_2\left(1 - e^{-\frac{t}{\tau_{e-e}}}\right)e^{-\frac{t}{\tau_{plex}}} \qquad (3.4)$$

Also in this case, to obtain more robust results, the fitting was performed with a global fit of the time traces at wavelengths around the peak position sharing the time constants.

The TM signal falls at around 525 nm for all the samples. From the 2D colormaps (figures 3.11d and f) it seems like the signal blue-shifts up to ca. 500n nm in hundred ps timescale and that

persists for long time. We think that the blue-shift could be an effect caused by the baseline correction, and the fact that data are a bit noisy makes this systematic error more evident. However, TM is the uncoupled plasmon and thus we do expect properties entirely analogue to the uncoupled NRs plasmons. For this reason, we are less interested on that specific spectral region.

Let's now move our attention on the UP dynamics, which lies at about 570 nm for JC_hy and MIX_hy, and about 560 for PI_hy (figure 3.11). Figure 3.12 shows the normalized time traces of three samples PI_hy_4_1, JC_hy_3_3 and MIX_hy_3_1, and their respective fitting curves obtained by using eq. 3.4. The RDD model fits well the UP time traces, and the resulting time constants for all samples are summarized in table 3.4. As we expected, the two early time constants describing the dynamics <10 ps resemble the NP τ_{e-e} and τ_{e-ph}. Interestingly, we found that the τ_{plex} of the mixed hybrid falls between those of JC_hy and PI_hy (table 3.4 and figure 3.13). This is a crucial piece of evidence to assess the microscopic properties of the mixed samples, as anticipated in section 3.2. If the MIX hybrid consisted of isolated domains of JC-hybrid and PI-hybrid, then its time-dependent signal would be just the sum of the two contributions. To rule out this hypothesis, we also tried to fit its UP dynamics by using a sum of two exponentials where we fixed the values of the two τ_{plex} constants at the PI_hy and JC_hy values. In this case the fit did not converge confirming that the signal cannot be expressed as the mere sum of the PI_hy and JC_hy contributions. This suggests that the electronic structure of the mixed hybrid is actually described by plexcitons where both PIC and JC-1 molecules interact together with the plasmonic mode, probably because the NRs is able to template the formation of a mixed aggregate.

These findings prove that plexcitonic nanohybrids are materials that promise a high control over the final optical properties. In this specific case, we found that it is possible to tune an optical property, i.e., the long-time decay constant τ_{plex}, by simply using a mixture of different dyes. This opens possible interesting perspectives for effectively exploit the SC to modify rates of molecular processes and chemically relevant reactions. Indeed, the possibility of control the lifetime of excited states could allow better exploitation of the energy of the excited states to promote relevant photochemical reactions.

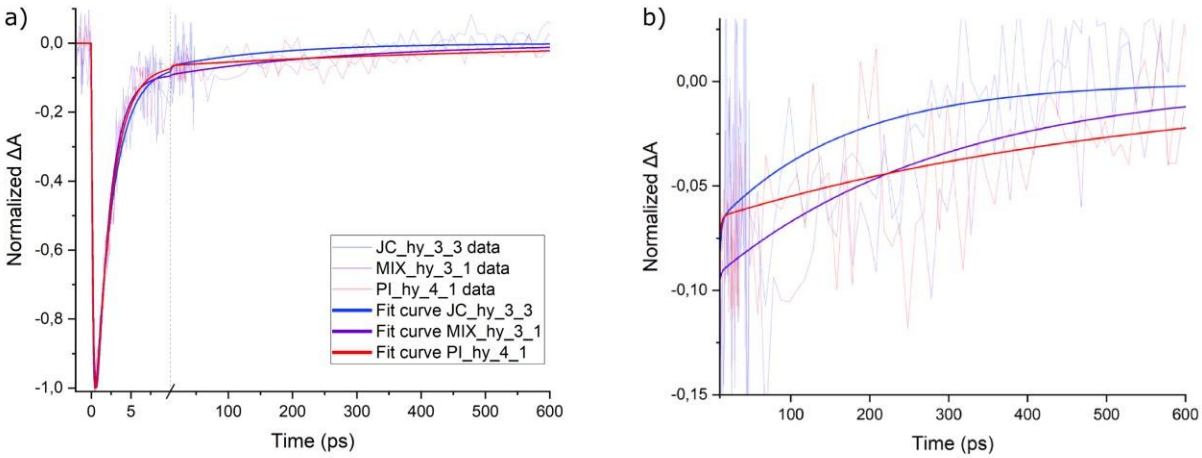

Figure 3.12 *a) Time traces of the UP of JC_hy_3_3 (blue), PI_hy_4_1 (red) and MIX_hy_3_1 (purple) and their respective fit curves. The data are normalized at their maximum. Notice the break in the time axis at 10 ps. B) The time window between 10 ps and 600 ps is zoomed to highlight the long-time decay of the three different hybrids. The fits help to see the differences and show that the mixed hybrid long decay time falls between the long decay time of the other samples.*

	τ_{e-e} (ps)	τ_{e-ph} (ps)	τ_{plex} (ps)
JC_hy_3_1	$0{,}17 \pm 0{,}01$	$2{,}18 \pm 0{,}07$	105 ± 16
JC_hy_3_2	$0{,}16 \pm 0{,}01$	$1{,}69 \pm 0{,}05$	192 ± 28
JC_hy_3_3	$0{,}17 \pm 0{,}01$	$2{,}32 \pm 0{,}05$	166 ± 43
PI_hy_3_1	$0{,}31 \pm 0{,}01$	$1{,}84 \pm 0{,}02$	468 ± 68
PI_hy_4_1	$0{,}24 \pm 0{,}01$	$2{,}03 \pm 0{,}03$	553 ± 82
MIX_hy_3_1	$0{,}32 \pm 0{,}02$	$1{,}66 \pm 0{,}04$	292 ± 39
MIX_hy_3_2	$0{,}29 \pm 0{,}02$	$1{,}69 \pm 0{,}04$	311 ± 34

Table 3.4 *Time constants resulting from the fitting of the UP traces for the different samples. The τ_{plex} constants, with the respective errors, are highlighted in red in the last column.*

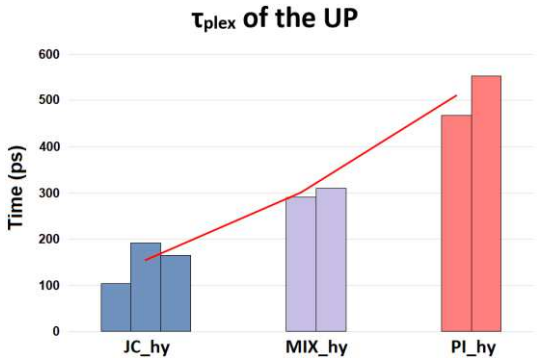

Figure 3.13 *Graphic representation of the τ_{plex} constants obtained for the different nanohybrids. Notice that τ_{plex} of the mixed hybrids have an intermediate value between the τ_{plex} of JC-1 and PIC hybrids.*

Let's now move to the dynamics recorded at the LP position. LP peak falls at about 610 nm for JC_hy and MIX_hy and about 595 nm for PI_hy. The intensity of the LP GSB of the PI_hy samples was in general too weak to allow a quantitative analysis, therefore we will refer to data obtained for the same sample, PI_hy_3, but measured at high pump fluences (820 μJ/cm^2). The time traces are shown in figure 3.14. As for the UP traces, we observed the uncoupled NRs behavior for the first 10 picoseconds, with the characteristic τ_{e-e} and τ_{e-ph} times. However, it is worth noting that the τ_{e-ph} of PI_hy_3_2 assumes a higher value because of its pump fluence dependence.[107] Instead, these dynamics are not well fitted by the RDD model (eq. 3.4) because

of the appearance of an interesting new feature, absent in the control samples. An additional rise time is indeed observed after about 10 ps (highlighted by the arrows in figure 3.14). Therefore, a new fitting model, that consider this new feature, was adopted, and the additional time constant is labelled τ_{rise}:

$$\Delta A = \Delta A_0 + A_1\left(1 - e^{-\frac{t}{\tau_{e-e}}}\right)e^{-\frac{t}{\tau_{e-ph}}} + A_2\left(1 - e^{-\frac{t}{\tau_{rise}}}\right)e^{-\frac{t}{\tau_{plex}}} \qquad (3.5)$$

The resulting fitting curves and the respective time constants extracted are reported in figure 3.14 and table 3.5, respectively. The new τ_{rise} assumes values between 10 and 50 ps. This rise of the LP GSB signal could be related to an increase of the LP population, promoted by an additional new mechanism that transfers energy to the LP state. The simplest hypothesis that the state is populated directly from the UP is not upheld by analyses of the UP dynamics, which

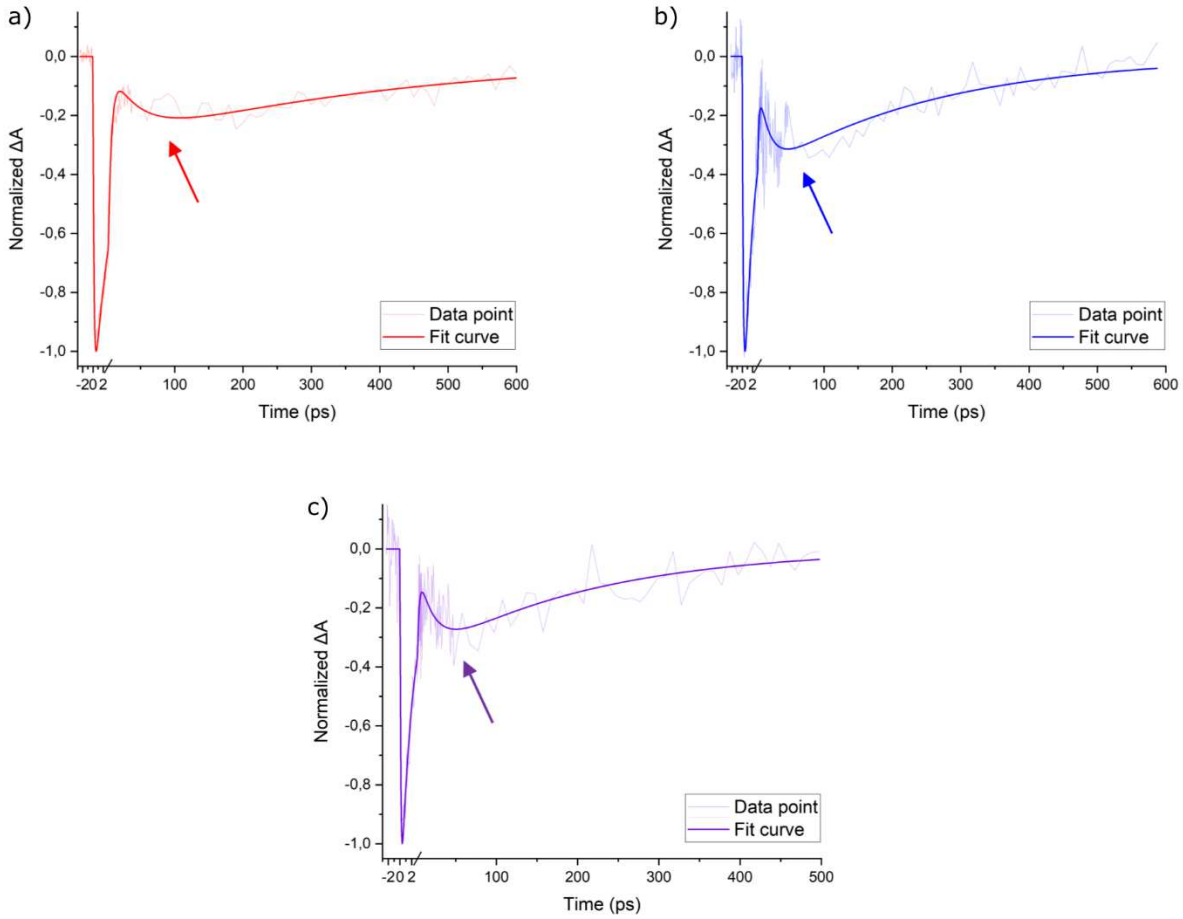

Figure 3.14 *Time traces of the LP of a) PI_hy_3_2 (red), b) JC_hy_3_3 (blue) and MIX_hy_3_1 (purple) and their respective fitting curves. Notice that PI_hy_3_2 measure was performed with a pump fluence of about 820 μJ/cm². The data are normalized at their maximum. The arrows highlight the time rise observed after about 10 ps. Notice the break in the time axis at 2 ps.*

Table 3.5 *Time constants resulting from the fitting of the LP traces for the different samples. The values of the τ_{rise} constants, with the respective errors, are highlighted in red in the last column.*

	τ_{e-e} (ps)	τ_{e-ph} (ps)	τ_{plex} (ps)	τ_{rise} (ps)
JC_hy_3_2	$0{,}12 \pm 0{,}02$	$2{,}11 \pm 0{,}08$	200 ± 17	15 ± 2
JC_hy_3_3	$0{,}23 \pm 0{,}02$	$2{,}04 \pm 0{,}06$	255 ± 20	17 ± 2
PI_hy_3_2	$0{,}19 \pm 0{,}01$	$4{,}80 \pm 0{,}05$	428 ± 25	46 ± 4
MIX_hy_3_1	$0{,}13 \pm 0{,}01$	$2{,}17 \pm 0{,}05$	210 ± 18	21 ± 4
MIX_hy_3_2	$0{,}63 \pm 0{,}09$	$1{,}57 \pm 0{,}09$	142 ± 23	36 ± 10

does not show a corresponding decay time (figure 3.12a). Thus, to explain this phenomenon is necessary to invoke the DSs.[18,27,28,108–111] DSs are optically inactive states, formed in the nanohybrid as a consequence of the various symmetry of the interactions between a large number of molecules and the plasmon mode (section 1.1.3). They are populated from higher energy states (including UP) in an ultrafast timescale (<100 fs)[23] and, because of their high density, they can efficiently act as a sink of excitation from plexcitons, affecting in a significant way the overall dynamics of nanohybrids. The density of DSs (DOS) should be maximum at the dip position opened in the broad plasmon resonance upon plexciton formation (section 1.1.3).[18,23] Based on that evidence, we analyzed the time traces near the dip position to verify the presence of dynamics compatible with the hypothesis of population of LP from the DSs. Let's assume the presence of a relaxation dynamics from DSs to LP. Considering that DSs get populated at early times from higher energy states,[23] an ESA from DSs to higher energy states is possible. This signal would be proportional to the population of DSs, therefore, the signal at dip position would decay following the relaxation of DSs. Thus, if in the DSs ESA dynamics a decay time is observed, which is compatible with the rise time seen in the LP GSB dynamics, then it is reasonable that the energy which populates the LP state come from the DSs.

Coming back to the dip position, in this spectral range there are several contributions to the signal: (i) GSB of UP, (ii) GSB of LP and possibly the (iii) ESA from the DSs to high-energy levels. The first two contributions produce negative signals, while the third one give rise to a positive signal. The sum of these three contributions lead to signal values close to zero, whose characterization is particularly challenging. To simplify the analysis, we selected wavelengths slightly blue-shifted with respect to the dip, where the contribution (ii) can be considered negligible. Also, based on the analyses described before, we expect that the dynamics mainly resemble the UP behavior (contribution (i)) at early (<10ps) and long (>100ps) times, and the

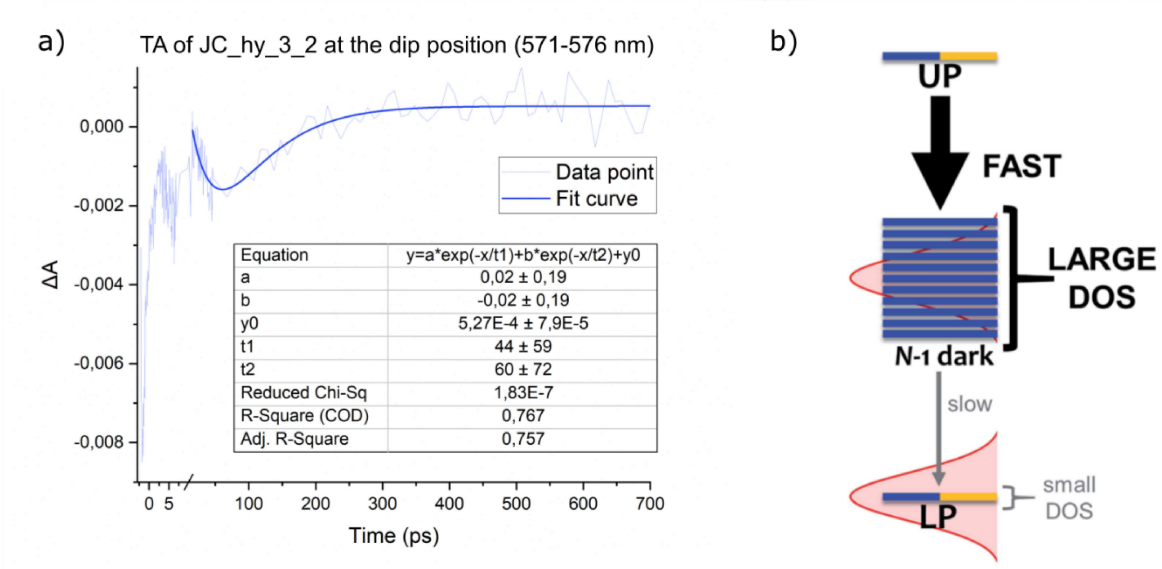

Figure 3.15 *a) Mediated time trace of JC_hy_3_2 at the dip position (571-576 nm), and the respective fitting curve. Notice the break in the time axis at 10 ps. The fitting parameters are reported in the table inset. Given the high level of noise, the associated errors are particularly high, preventing any reliable quantitative discussion; therefore, we consider these values only for a qualitative analysis. b) Graphic representation of the fast decay from UP to DSs, favored by their large DOS, followed by a slower population of LP from the DSs. Reproduced from ref* [23].

ESA decay (contribution (iii)) at intermediate times. We then focused our attention on the dynamic behavior for times >10 ps, and the results of the corresponding fitting are shown in figure 3.15a. We found two times constants, the first one (with a positive pre-exponential factor) can be associated with the ESA decay and the second one (with a negative pre-exponential factor) with the slow decay time (τ_{plex}) already seen in the UP state.

We want to stress that, because of the high level of noise and the fact that the signal is very close to zero, the errors associated with the extracted time constants are particularly high and prevent any reliable quantitative discussion. Nonetheless, a qualitative analysis is possible, and it suggests that the shape of the time trace is consistent with the behavior just described. Thus, we can conclude that, together with other evidence in literature,[18,23,112] these data contribute to support the hypothesis of a population of the LP state from the DSs (figure 3.15b).

The last phenomenon that will be discussed in this section is a time-dependent blue shift observed for the LP signal (figure 3.16). One possible explanation relies on the Rabi contraction upon excitation (section 1.2.3.1). In fact, because of Rabi contraction, the differential absorption signal is expected to assume a derivative-like shape with a positive signal between the two bands (LP and UP). Thus, the respective peaks appear shifted (figure 3.17a). Indeed, if

there is a contraction of the Rabi splitting, then the two peaks associated with UP and LP in the TA spectra (dashed line in figure 3.17a) move away one from each other. When the molecules relax back, the contraction is over and the peaks recover their initial position. Time-dependent Rabi contraction was already observed in plexcitonic nanohybrids based on gold NRs and JC-1.[56] This phenomenon, however, was over within the first ps, i.e., the exciton lifetime. Instead, the blue shift observed in our data lasts for much longer times (>20 ps), suggesting a different origin. It is also worthy highlighting that the reason why we did not observe the Rabi contraction features recorded in ref [56] could be because of our particular experimental conditions. Indeed, our pump excitation was set at 400 nm, in resonance with the plasmon resonance of the NRs

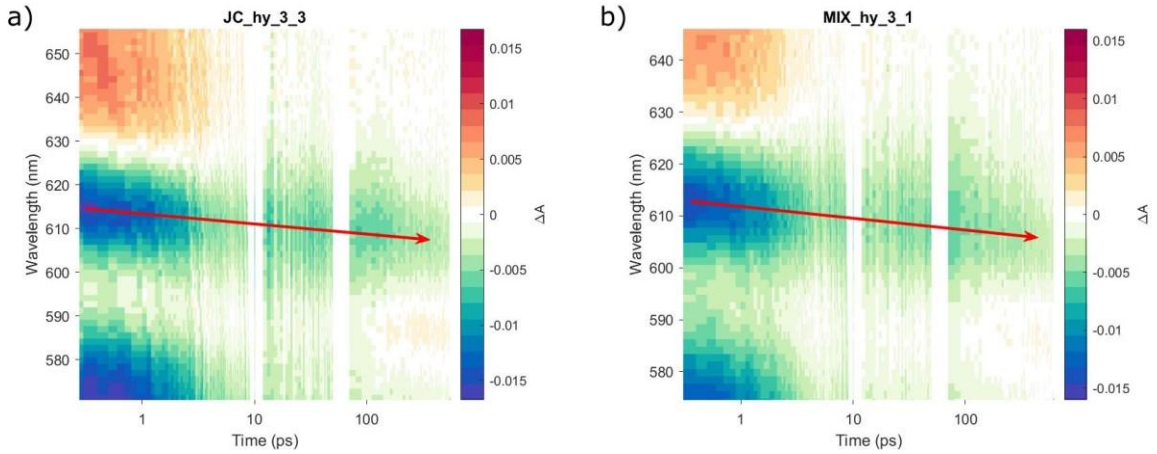

Figure 3.16 *2D colormaps of the TA measure of JC_hy_3_3 and MIX_hy_3_1 respectively, zoomed at the LP signal position. The arrows pinpoint the time-dependent blue shift of the negative GSB signal of LP.*

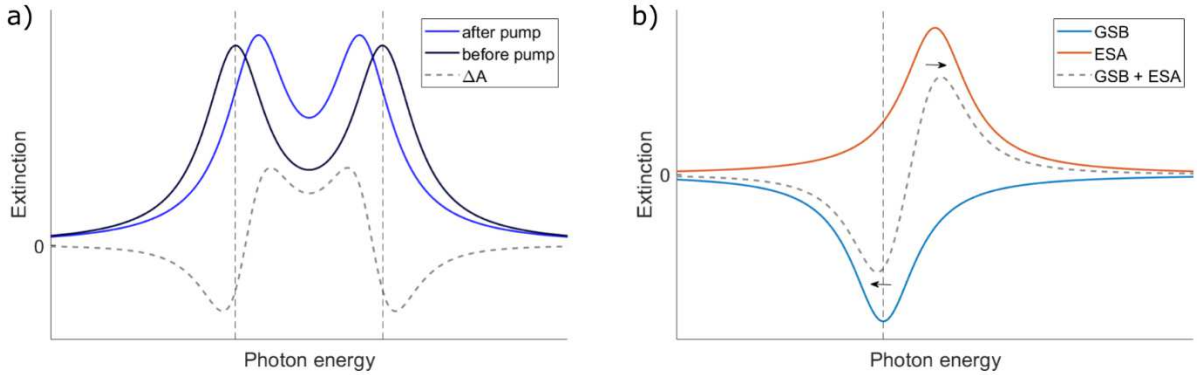

Figure 3.17 *Graphic representation of a) the Rabi contraction after pump excitation, and b) the sum of a negative GSB and a positive ESA signal. Both the effects produce derivative-shaped bands with the peaks that 'apparently' shift. These curves were built using Lorentzian functions.*

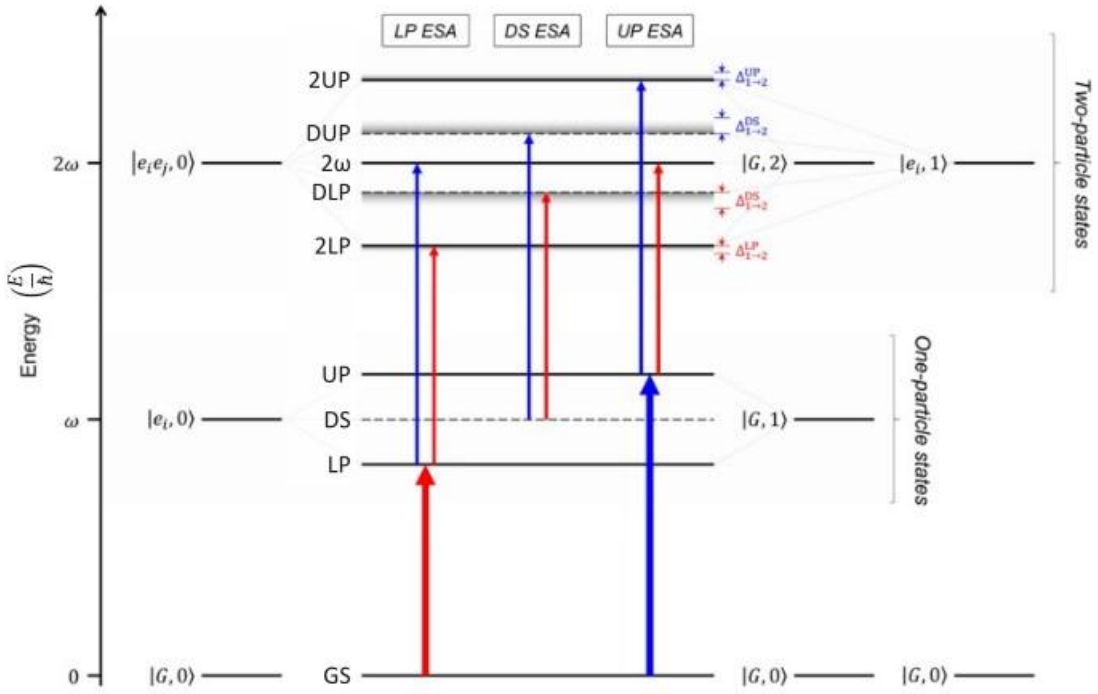

Figure 3.18 *Energy structure of the one- and two-particle states in the TC model for a resonant cavity of frequency ω. Light–matter states with only excitons ($|e_i,0\rangle, |e_ie_j,0\rangle$), only photons ($|G,1\rangle, |G,2\rangle$), and one exciton and one photon ($|e_i,1\rangle$) are plotted at their respective energies. The coupling of states with one exciton and no photon ($E=\hbar\omega$; left) to states containing no exciton and one photon ($E=\hbar\omega$; right) creates one-particle states, and the coupling between states with two excitons and no photon ($E=2\hbar\omega$; left), one exciton and one photon, and no exciton and two photons ($E=2\hbar\omega$; right) give rise to two-particle states. LP (2LP) and UP (2UP) denote lower and upper polaritons in the one(two)-particle manifold. DLP and DUP are two additional states in the two-particle states, which are dark from the one-particle polariton states. Dipole-allowed transitions are shown as arrows (red and blue correspond to transitions at or close to the energy of LP and UP, respectively). Adapted from ref* [18].

and not with the plexciton bands. As already discussed previously, in these conditions phenomena related to the particles dominated the first 10 ps dynamics and likely covered the Rabi contraction response.

A more realistic interpretation of the blue shift could be found considering the contribution of ESA signals. Indeed, when a negative band (GSB) is partially overlapped with a positive band (ESA), the resulting signal consists of a band with a derivative-like shape with the two peaks apparently shifted and separated by a greater distance (figure 3.17b). Therefore, the time-dependent blue-shift of the GSB could be the result of an additional positive signal (ESA), centered at higher wavelength, that is increasing with respect the to negative signal (GSB) over time. Alternatively, the same effect can be produced by an additional positive signal (ESA), at lower wavelength, that is decreasing with respect to the negative signal (GSB). Very

interestingly, the second hypothesis is in agreement with the mechanism of population of LP from the DSs discussed above. In fact, the simultaneous ESA decay of DSs at the dip position, matched by the GSB rise at the LP wavelength, is compatible both with LP blue shift and LP population from DSs. Clearly, because of the complexity of the spectral response, is very hard to identify with certainty the phenomena really responsible of this behavior. In fact, also the NP, which contributes to the positive signal around 650 nm (figure 3.10a), could contribute to induce a blue shift of the LP peak in the same way. Thus, further focused experiments are necessary to support our interpretation.

It is also important to discuss the nature of the higher energy states reached after the ESA. These states can be described by using the many-body polariton theory[18,28] (section 1.1.5) in which also 'two-particles' states are taken into consideration. The illustration taken from ref [18], in figure 3.18, shows a schematic representation of the states generated by light-matter interaction and the possible dynamics developing upon excitation. It is outlined that ESA can involve transitions from UP, LP and DSs to those states originated by two-particle interactions.

In addition to this, also the energetic disorder plays a key role,[55] increasing drastically the overall number of states to the point that it should be more correct speaking about density of states, instead of single states. Obviously, this comprehensive picture makes possible a huge number of energy pathways, which involve a great number of states, and that make us fully aware of the enormous complexity that stands behind these plexcitonic nanosystems.

3.3.4 Final remarks about plexcitons nonlinearities

We analyzed the optical nonlinearities of different plexcitonic nanosystems through pump-probe spectroscopy. We observed dynamics that at early times (<10 ps) resemble the bare NPs' behavior, while in the long scale times show interesting features, typical of plexcitons formation.

The first important result was to find that the kinetics of the MIX hybrids cannot be described as the mere sum of those of JC-1 and PIC based systems, supporting the formation of mixed plexciton resonances. Although further work must be done to support this hypothesis, these are very promising data which show that it is possible to engineering a material with desired

optical properties acting on chemical parameters such as, in this case, the relative concentrations of two different dyes.

Then, we found two particular nonlinear behaviors: (i) a rise of the LP population after about 10 ps and (ii) a blue shift of the LP peak as a function of time. These two phenomena can be rationalized invoking the presence of Dss and two-particle states.

The important final remark is that all the experimental findings suggest that plexcitons' dynamics is much more complicated than what expected based on the easy picture of a downhill energy cascade from UP to DSs and then to LP. When DSs, two-particle states and energetic disorder are taken into consideration, the number of states involved increase drastically. Thus, it is likely that all these states take part in a more complex process of energy redistribution, as recently demonstrated also for porphyrin based nanohybrids.[54] Therefore, the characterization of the dynamics involved in plexcitonic systems is really challenging and remain still largely underexplored in the literature. For this reason, further work is necessary. A way to gain more detailed information is to make on-resonance experiments, or better, to adopt more advanced spectroscopies, such as bidimensional spectroscopy.

Conclusion and future perspectives

The work presented in this Thesis fits in the vast research field of nanomaterials for the exploitation of light-matter coupling. The tremendous potentiality of plexcitonic nanomaterials rises from the possibility of designing their optical properties through coupling with light. Gaining intimate control over this coupling allows engineering materials with different functionality that can have applications in many fields. To attain this control, complete and thorough knowledge of the properties of plexcitonic systems must be preliminarily achieved. However, several fundamental aspects of the design, the dynamics and the structure-properties relationships of these nanohybrids are still unknown.

To fill this gap, in this Thesis we designed different plexcitonic systems in a controlled and reproducible way and characterized their optical and photophysical properties with both linear and nonlinear spectroscopies. The motivations driving this work were to: (i) find the suitable conditions to get strong coupling between plasmonic substrates and different molecular moieties; (ii) prove the high versatility of plexcitonic-based materials by identifying relationships between the structure and the dynamics of these systems; (iii) gain an in-depth knowledge over both linear properties and dynamics of plexcitonic nanosystems. Thus, the results of this Thesis can be classified according to these three main objectives.

We explored the strong coupling conditions between gold nanorods and two classes of organic dyes, porphyrins and cyanines. As regards porphyrins, we tried with TPPS, already known to strongly couple with gold nanospheres. We learned that with nanorods instead, much more efforts are necessary to optimize the supramolecular interactions and maintain the solution stable. In addition, it cannot be fully excluded that the incorrect dipoles' orientation could hamper the interactions. Thus, further work must be done to explore the most suitable chemical conditions to get plexcitonic nanosystems with porphyrins and gold nanorods, and a morphological analysis could also be helpful. The situation was different with cyanines. We verified that PIC and JC-1 molecules easily self-assemble in the form of J-aggregates on the

nanorods' surface and the resulting suspensions are stable. Therefore, strong coupling with both cyanine dyes was reached; in addition, plexcitonic nanohybrids including both dyes simultaneously were also designed and easily obtained.

The UV-Vis characterization confirmed the plexcitons formation by the appearance of a Rabi splitting that fulfilled the SC conditions in all the cases. Then, inspired by recent studies on the optical activity of strongly light-matter coupled systems, we also performed circular dichroism measurements, suggesting that optical chirality could be a powerful tool for better understanding the strong coupling regime. Finally, we analyzed the optical nonlinearities of the plexcitonic nanosystems through pump-probe spectroscopy. We observed two interesting nonlinear features: (i) a rise of the lower polariton population after about 10 ps and (ii) a blue shift of the lower polariton peak as a function of time. Beyond the detailed interpretation of these features, the point we want to underline is that, because of the vast number of states involved when dark states, two-particle states and energetic disorder are taken into consideration, plexcitonic systems have dynamics much more complicated than what expected based on the easy model of a downhill energy cascade from upper polariton to dark states to lower polariton. Therefore, the study of plexcitonic dynamics is really challenging, and much work is still needed. For this purpose, more advanced spectroscopies, such as bidimensional spectroscopy, can be employed for a more in-depth analysis of ultrafast dynamics.

Also the characterization of the MIX plexcitonic nanohybrids provided exciting results. We designed this mixed plexciton to verify if it is possible to tune some properties of the plexcitonic nanosystems by acting on the composition of the organic fraction. Thus, the ensuing characterization was aimed at comparing these mixed systems with the others based on PIC and JC-1 only. For this purpose, it is also necessary to establish the nature of this mixed system. Mainly, we investigated if it consists of i) a new plexciton with different characteristics originating from the mutual interaction of JC-1 and PIC with the nanoparticle; or (ii) the mere coexistence of different domains of non-interacting JC-1 and PIC plexcitons. Interestingly, both the preliminary linear characterizations and the following nonlinear time-resolved measurements are consistent with the first hypothesis. Indeed, we found that the relaxation kinetics of the mixed hybrids cannot be described as the mere sum of those of JC-1 and PIC systems. These are very promising data that show that it is possible to tune an optical property

acting on chemical parameters such as, in this case, the relative concentrations of two different dyes.

To conclude, further work on analogous systems must be done to confirm the results of this Thesis. However, the preliminary results exposed here represent a significant stepping stone towards a more conscious plexcitons design and a better understanding of their photophysical behavior, and they can significantly contribute to the development of innovative devices based on plexcitonic materials.

References

(1) Hertzog, M.; Wang, M.; Mony, J.; Börjesson, K. Strong Light–Matter Interactions: A New Direction within Chemistry. *Chem Soc Rev* **2019**, *48* (3), 937–961. https://doi.org/10.1039/C8CS00193F.

(2) Marquier, F.; Sauvan, C.; Greffet, J.-J. Revisiting Quantum Optics with Surface Plasmons and Plasmonic Resonators. *ACS Photonics* **2017**, *4* (9), 2091–2101. https://doi.org/10.1021/acsphotonics.7b00475.

(3) Baranov, D. G.; Wersäll, M.; Cuadra, J.; Antosiewicz, T. J.; Shegai, T. Novel Nanostructures and Materials for Strong Light–Matter Interactions. *ACS Photonics* **2018**, *5* (1), 24–42. https://doi.org/10.1021/acsphotonics.7b00674.

(4) Dovzhenko, D. S.; Ryabchuk, S. v.; Rakovich, Y. P.; Nabiev, I. R. Light-Matter Interaction in the Strong Coupling Regime: Configurations, Conditions, and Applications. *Nanoscale* **2018**, *10* (8), 3589–3605. https://doi.org/10.1039/c7nr06917k.

(5) Törmä, P.; Barnes, W. L. Strong Coupling between Surface Plasmon Polaritons and Emitters: A Review. *Rep Prog Phys* **2015**, *78* (1), 013901. https://doi.org/10.1088/0034-4885/78/1/013901.

(6) Nan, F.; Ding, S.-J.; Ma, L.; Cheng, Z.-Q.; Zhong, Y.-T.; Zhang, Y.-F.; Qiu, Y.-H.; Li, X.; Zhou, L.; Wang, Q.-Q. Plasmon Resonance Energy Transfer and Plexcitonic Solar Cell. *Nanoscale* **2016**, *8* (32), 15071–15078. https://doi.org/10.1039/C6NR02633H.

(7) Manuel, A. P.; Kirkey, A.; Mahdi, N.; Shankar, K. Plexcitonics – Fundamental Principles and Optoelectronic Applications. *J Mater Chem C Mater* **2019**, *7* (7), 1821–1853. https://doi.org/10.1039/C8TC05054F.

(8) Srivastava, T.; Jha, R. Plexcitonic Nose Based on an Organic Semiconductor. *Appl Phys Lett* **2020**, *117* (9), 093301. https://doi.org/10.1063/5.0019027.

(9) Choi, Y.; Kang, T.; Lee, L. P. Plasmon Resonance Energy Transfer (PRET)-Based Molecular Imaging of Cytochrome c in Living Cells. *Nano Lett* **2009**, *9* (1), 85–90. https://doi.org/10.1021/nl802511z.

(10) Imamoglu, A.; Awschalom, D. D.; Burkard, G.; DiVincenzo, D. P.; Loss, D.; Sherwin, M.; Small, A. Quantum Information Processing Using Quantum Dot Spins and Cavity QED. *Phys Rev Lett* **1999**, *83* (20), 4204–4207. https://doi.org/10.1103/PhysRevLett.83.4204.

(11) Serrera, G.; González-Colsa, J.; Giannini, V.; Saiz, J. M.; Albella, P. Enhanced Optical Chirality with Directional Emission of Surface Plasmon Polaritons for Chiral Sensing Applications. *J Quant Spectrosc Radiat Transf* **2022**, *284*, 108166. https://doi.org/https://doi.org/10.1016/j.jqsrt.2022.108166.

(12) Hartland, G. v. Optical Studies of Dynamics in Noble Metal Nanostructures. *Chem Rev* **2011**, *111* (6), 3858–3887. https://doi.org/10.1021/cr1002547.

(13) Amendola, V.; Pilot, R.; Frasconi, M.; Maragò, O. M.; Iatì, M. A. Surface Plasmon Resonance in Gold Nanoparticles: A Review. *J Phys Condens Matter* **2017**, *29* (20), 203002. https://doi.org/10.1088/1361-648X/aa60f3.

(14) Ebbesen, T. W. Hybrid Light-Matter States in a Molecular and Material Science Perspective. *Acc Chem Res* **2016**, *49* (11), 2403–2412. https://doi.org/10.1021/acs.accounts.6b00295.

(15) Pelton, M.; Storm, S. D.; Leng, H. Strong Coupling of Emitters to Single Plasmonic Nanoparticles: Exciton-Induced Transparency and Rabi Splitting. *Nanoscale* **2019**, *11* (31), 14540–14552. https://doi.org/10.1039/c9nr05044b.

(16) Chikkaraddy, R.; de Nijs, B.; Benz, F.; Barrow, S. J.; Scherman, O. A.; Rosta, E.; Demetriadou, A.; Fox, P.; Hess, O.; Baumberg, J. J. Single-Molecule Strong Coupling at Room Temperature in Plasmonic Nanocavities. *Nature* **2016**, *535* (7610), 127–130. https://doi.org/10.1038/nature17974.

(17) Grynberg, G.; Aspect, A.; Fabre, C.; Cohen-Tannoudji, C. *Introduction to Quantum Optics*; Cambridge University Press, 2010. https://doi.org/10.1017/CBO9780511778261.

(18) Fassioli, F.; Park, K. H.; Bard, S. E.; Scholes, G. D. Femtosecond Photophysics of Molecular Polaritons. *J Phys Chem Lett* **2021**, *12* (46), 11444–11459. https://doi.org/10.1021/acs.jpclett.1c03183.

(19) Fujii, K. Introduction to the Rotating Wave Approximation (RWA): Two Coherent Oscillations. *Journal of Modern Physics* **2017**, *8* (12), 2042–2058. https://doi.org/10.4236/jmp.2017.812124.

(20) Koenderink, A. F. On the Use of Purcell Factors for Plasmon Antennas. *Opt Lett* **2010**, *35* (24), 4208–4210. https://doi.org/10.1364/OL.35.004208.

(21) Sauvan, C.; Hugonin, J. P.; Maksymov, I. S.; Lalanne, P. Theory of the Spontaneous Optical Emission of Nanosize Photonic and Plasmon Resonators. *Phys Rev Lett* **2013**, *110* (23), 237401. https://doi.org/10.1103/PhysRevLett.110.237401.

(22) Kristensen, P. T.; Hughes, S. Modes and Mode Volumes of Leaky Optical Cavities and Plasmonic Nanoresonators. *ACS Photonics* **2014**, *1* (1), 2–10. https://doi.org/10.1021/ph400114e.

(23) Ribeiro, R. F.; Martínez-Martínez, L. A.; Du, M.; Campos-Gonzalez-Angulo, J.; Yuen-Zhou, J. Polariton Chemistry: Controlling Molecular Dynamics with Optical Cavities. *Chem Sci* **2018**, *9* (30), 6325–6339. https://doi.org/10.1039/C8SC01043A.

(24) Hugall, J. T.; Singh, A.; van Hulst, N. F. Plasmonic Cavity Coupling. *ACS Photonics* **2018**, *5* (1), 43–53. https://doi.org/10.1021/acsphotonics.7b01139.

(25) Garraway, B. M. The Dicke Model in Quantum Optics: Dicke Model Revisited. *Philosophical Transactions of the Royal Society A: Mathematical, Physical and Engineering Sciences* **2011**, *369* (1939), 1137–1155. https://doi.org/10.1098/RSTA.2010.0333.

(26) Fleischhauer, M.; Lukin, M. D. Quantum Memory for Photons: Dark-State Polaritons. *Phys Rev A (Coll Park)* **2002**, *65* (2), 022314. https://doi.org/10.1103/PhysRevA.65.022314.

(27) Gonzalez-Ballestero, C.; Feist, J.; Gonzalo Badía, E.; Moreno, E.; Garcia-Vidal, F. J. Uncoupled Dark States Can Inherit Polaritonic Properties. *Phys Rev Lett* **2016**, *117* (15), 156402. https://doi.org/10.1103/PhysRevLett.117.156402.

(28) DelPo, C. A.; Kudisch, B.; Park, K. H.; Khan, S.-U.-Z.; Fassioli, F.; Fausti, D.; Rand, B. P.; Scholes, G. D. Polariton Transitions in Femtosecond Transient Absorption Studies of Ultrastrong Light-Molecule Coupling. *J Phys Chem Lett* **2020**, *11* (7), 2667–2674. https://doi.org/10.1021/acs.jpclett.0c00247.

(29) Scholes, G. D. Polaritons and Excitons: Hamiltonian Design for Enhanced Coherence. *Proceedings of the Royal Society A: Mathematical, Physical and Engineering Sciences* **2020**, *476* (2242), 20200278. https://doi.org/10.1098/rspa.2020.0278.

(30) Kubo, R. A Stochastic Theory of Line Shape. In *Advances in Chemical Physics*; Advances in Chemical Physics; 2007; pp 101–127. https://doi.org/10.1002/9780470143605.ch6.

(31) Kasha, M. Energy Transfer Mechanisms and the Molecular Exciton Model for Molecular Aggregates. *Radiat Res* **1963**, *20* (1), 55–70. https://doi.org/10.2307/3571331.

(32) Davydov, A. S. *Theory of Molecular Excitons*; Springer US: New York, NY, 1971. https://doi.org/10.1007/978-1-4899-5169-4/COVER.

(33) Kasha, M.; Rawls, H. R.; Ashraf El-Bayoumi, M. The Exciton Model in Molecular Spectroscopy. *Pure and Applied Chemistry* **1965**, *11* (3–4), 371–392. https://doi.org/10.1351/pac196511030371.

(34) Takeno, S.; Mabuchi, M. A Theory of Frenkel Excitons Using a Two-Level-Atom Model. *Progress of Theoretical Physics* **1973**, *50* (6), 1848–1866. https://doi.org/10.1143/PTP.50.1848.

(35) Knapp, E. W. Lineshapes of Molecular Aggregates, Exchange Narrowing and Intersite Correlation. *Chem Phys* **1984**, *85* (1), 73–82. https://doi.org/10.1016/S0301-0104(84)85174-5.

(36) Han, J.; Zhang, H.; Abramavicius, D. Exchange Narrowing and Exciton Delocalization in Disordered J Aggregates: Simulated Peak Shapes in the Two Dimensional Spectra. *J Chem Phys* **2013**, *139* (3), 034313. https://doi.org/10.1063/1.4812927.

(37) Spano, F. C.; Mukamel, S. Superradiance in Molecular Aggregates. *J Chem Phys* **1998**, *91* (2), 683. https://doi.org/10.1063/1.457174.

(38) Potma, E. O.; Wiersma, D. A. Exciton Superradiance in Aggregates: The Effect of Disorder, Higher Order Exciton-Phonon Coupling and Dimensionality. *J Chem Phys* **1998**, *108* (12), 4894. https://doi.org/10.1063/1.475898.

(39) Maiti, N. C.; Mazumdar, S.; Periasamy, N. J- and H-Aggregates of Porphyrin−Surfactant Complexes: Time-Resolved Fluorescence and Other Spectroscopic Studies. *J Phys Chem B* **1998**, *102* (9), 1528–1538. https://doi.org/10.1021/jp9723372.

(40) MAITI, N. C.; MAZUMDAR, S.; PERIASAMY, N. J- and H-Aggregates of Porphyrins with Surfactants: Fluorescence, Stopped Flow and Electron Microscopy Studies. *J Porphyr Phthalocyanines* **1998**, *02* (05), 369–376. https://doi.org/10.1002/(SICI)1099-1409(199807/10)2:4/5<369::AID-JPP92>3.0.CO;2-3.

(41) Bricks, J. L.; Slominskii, Y. L.; Panas, I. D.; Demchenko, A. P. Fluorescent J-Aggregates of Cyanine Dyes: Basic Research and Applications Review. *Methods Appl Fluoresc* **2018**, *6* (1), 012001. https://doi.org/10.1088/2050-6120/aa8d0d.

(42) Maier, S. A. *Plasmonics: Fundamentals and Applications*; Springer US: New York, NY, 2007. https://doi.org/10.1007/0-387-37825-1.

(43) Simon, T. Coherent Lifetimes of Excitons and Plexcitons in Organic-Inorganic Nanostructures, Ludwig Maximilian University Munich, 2017.

(44) Wokaun, A.; Gordon, J. P.; Liao, P. F. Radiation Damping in Surface-Enhanced Raman Scattering. *Phys Rev Lett* **1982**, *48* (14), 957–960. https://doi.org/10.1103/PhysRevLett.48.957.

(45) Meng, L.; Zhang, J.; Li, H.; Zhao, W.; Zhao, T. Preparation and Progress in Application of Gold Nanorods. *J Nanomater* **2019**, *2019*, 1–11. https://doi.org/10.1155/2019/4925702.

(46) Kreibig, U.; Vollmer, M. *Optical Properties of Metal Clusters*; Springer Series in Materials Science; Springer Berlin Heidelberg: Berlin, Heidelberg, 1995; Vol. 25. https://doi.org/10.1007/978-3-662-09109-8.

(47) Voisin, C.; del Fatti, N.; Christofilos, D.; Vallée, F. Ultrafast Electron Dynamics and Optical Nonlinearities in Metal Nanoparticles. *J Phys Chem B* **2001**, *105* (12), 2264–2280. https://doi.org/10.1021/jp0038153.

(48) Link, S.; El-Sayed, M. A. Optical Properties and Ultrafast Dynamics of Metallic Nanocrystals. *Annu Rev Phys Chem* **2003**, *54* (1), 331–366. https://doi.org/10.1146/annurev.physchem.54.011002.103759.

(49) Kats, M. A.; Yu, N.; Genevet, P.; Gaburro, Z.; Capasso, F. Effect of Radiation Damping on the Spectral Response of Plasmonic Components. *Opt Express* **2011**, *19* (22), 21748–21735. https://doi.org/10.1364/OE.19.021748.

(50) Brongersma, M. L.; Halas, N. J.; Nordlander, P. Plasmon-Induced Hot Carrier Science and Technology. *Nat Nanotechnol* **2015**, *10* (1), 25–34. https://doi.org/10.1038/nnano.2014.311.

(51) Li, X.; Xiao, D.; Zhang, Z. Landau Damping of Quantum Plasmons in Metal Nanostructures. *New J Phys* **2013**, *15* (2), 023011. https://doi.org/10.1088/1367-2630/15/2/023011.

(52) Alabastri, A.; Tuccio, S.; Giugni, A.; Toma, A.; Liberale, C.; Das, G.; Angelis, F.; Fabrizio, E.; Zaccaria, R. Molding of Plasmonic Resonances in Metallic Nanostructures: Dependence of the Non-Linear Electric Permittivity on System Size and Temperature. *Materials* **2013**, *6* (11), 4879–4910. https://doi.org/10.3390/ma6114879.

(53) Vasa, P.; Wang, W.; Pomraenke, R.; Lammers, M.; Maiuri, M.; Manzoni, C.; Cerullo, G.; Lienau, C. Real-Time Observation of Ultrafast Rabi Oscillations between Excitons and Plasmons in Metal Nanostructures with J-Aggregates. *Nat Photonics* **2013**, *7* (2), 128–132. https://doi.org/10.1038/nphoton.2012.340.

(54) Peruffo, N.; Mancin, F.; Collini, E. Ultrafast Dynamics of Multiple Plexcitons in Colloidal Nanomaterials : The Mediating Action of Plasmon Resonances and Dark States. *J Phys Chem Lett* **2022**, *13* (28), 6412–6419. https://doi.org/10.1021/acs.jpclett.2c01750.

(55) Son, M.; Armstrong, Z.; Allen, R.; Arnold, M. Energy Cascades in Polaritonic Systems with Energetic Disorder Observed by Ultrafast Two- Dimensional White-Light Spectroscopy. **2022**.

(56) Simon, T.; Melnikau, D.; Sánchez-Iglesias, A.; Grzelczak, M.; Liz-Marzán, L. M.; Rakovich, Y.; Feldmann, J.; Urban, A. S. Exploring the Optical Nonlinearities of Plasmon-Exciton Hybrid Resonances in Coupled Colloidal Nanostructures. *The Journal of Physical Chemistry C* **2016**, *120* (22), 12226–12233. https://doi.org/10.1021/acs.jpcc.6b04658.

(57) Swinehart, D. F. The Beer-Lambert Law. *J Chem Educ* **1962**, *39* (7), 333–335. https://doi.org/10.1021/ED039P333.

(58) Woody, R. W. B. T.-M. in E. [4] Circular Dichroism. In *Biochemical Spectroscopy*; Academic Press, 1995; Vol. 246, pp 34–71. https://doi.org/https://doi.org/10.1016/0076-6879(95)46006-3.

(59) Boyd, R. W. *Nonlinear Optics, Third Edition*, 3rd ed.; Academic Press, Inc.: USA, 2008.

(60) Mukamel, S. *Principles of Nonlinear Optical Spectroscopy*; Oxford series in optical and imaging sciences; Oxford University Press, 1995.

(61) Jonas, D. M. Two-Dimensional Femtosecond Spectroscopy. *Annu Rev Phys Chem* **2003**, *54* (1), 425–463. https://doi.org/10.1146/annurev.physchem.54.011002.103907.

(62) Collini, E. 2D Electronic Spectroscopic Techniques for Quantum Technology Applications. *The Journal of Physical Chemistry C* **2021**, *125* (24), 13096–13108. https://doi.org/10.1021/acs.jpcc.1c02693.

(63) Beeby, A. Pump-Probe Laser Spectroscopy. In *An Introduction to Laser Spectroscopy: Second Edition*; Andrews, D. L., Demidov, A. A., Eds.; Springer US: Boston, MA, 2002; pp 105–137. https://doi.org/10.1007/978-1-4615-0727-7_4.

(64) Scarabelli, L.; Sánchez-Iglesias, A.; Pérez-Juste, J.; Liz-Marzán, L. M. A "Tips and Tricks" Practical Guide to the Synthesis of Gold Nanorods. *J Phys Chem Lett* **2015**, *6* (21), 4270–4279. https://doi.org/10.1021/acs.jpclett.5b02123.

(65) Isago, H. *Optical Spectra of Phthalocyanines and Related Compounds*, 1st ed.; NIMS Monographs; Springer Tokyo: Tokyo, 2015. https://doi.org/10.1007/978-4-431-55102-7.

(66) Gouterman, M. Spectra of Porphyrins. *J Mol Spectrosc* **1961**, *6* (C), 138–163. https://doi.org/10.1016/0022-2852(61)90236-3.

(67) Gouterman, M.; Wagnière, G. H.; Snyder, L. C. Spectra of Porphyrins: Part II. Four Orbital Model. *J Mol Spectrosc* **1963**, *11* (1–6), 108–127. https://doi.org/10.1016/0022-2852(63)90011-0.

(68) Peruffo, N.; Gil, G.; Corni, S.; Mancin, F.; Collini, E. Selective Switching of Multiple Plexcitons in Colloidal Materials: Directing the Energy Flow at the Nanoscale. *Nanoscale* **2021**, *13* (12), 6005–6015. https://doi.org/10.1039/d1nr00775k.

(69) Kim, Y.; Bertagna, F.; D'Souza, E. M.; Heyes, D. J.; Johannissen, L. O.; Nery, E. T.; Pantelias, A.; Sanchez-Pedreño Jimenez, A.; Slocombe, L.; Spencer, M. G.; Al-Khalili, J.; Engel, G. S.; Hay, S.; Hingley-Wilson, S. M.; Jeevaratnam, K.; Jones, A. R.; Kattnig, D. R.; Lewis, R.; Sacchi, M.; Scrutton, N. S.; Silva, S. R. P.; McFadden, J. Quantum Biology: An Update and Perspective. *Quantum Reports* **2021**, *3* (1), 80–126. https://doi.org/10.3390/quantum3010006.

(70) Ohno, O.; Kaizu, Y.; Kobayashi, H. J-aggregate Formation of a Water-soluble Porphyrin in Acidic Aqueous Media. *J Chem Phys* **1993**, *99* (5), 4128–4139. https://doi.org/10.1063/1.466109.

(71) Kano, H.; Kobayashi, T. Time-Resolved Fluorescence and Absorption Spectroscopies of Porphyrin J-Aggregates. *J Chem Phys* **2001**, *116* (1), 184–195. https://doi.org/10.1063/1.1421073.

(72) Bolzonello, L.; Albertini, M.; Collini, E.; di Valentin, M. Delocalized Triplet State in Porphyrin J-Aggregates Revealed by EPR Spectroscopy. *Physical Chemistry Chemical Physics* **2017**, *19* (40), 27173–27177. https://doi.org/10.1039/C7CP02968C.

(73) Collini, E.; Ferrante, C.; Bozio, R. Strong Enhancement of the Two-Photon Absorption of Tetrakis(4-Sulfonatophenyl)Porphyrin Diacid in Water upon Aggregation. *Journal of Physical Chemistry B* **2005**, *109* (1), 2–5. https://doi.org/10.1021/JP045652E/SUPPL_FILE/JP045652E_S.PDF.

(74) Peruffo, N.; Mancin, F.; Collini, E. Plexcitonic Nanohybrids Based on Gold Nanourchins: The Role of the Capping Layer. *The Journal of Physical Chemistry C* **2021**, *125* (36), 19897–19905. https://doi.org/10.1021/acs.jpcc.1c05862.

(75) Thomas, R.; Thomas, A.; Pullanchery, S.; Joseph, L.; Somasundaran, S. M.; Swathi, R. S.; Gray, S. K.; Thomas, K. G. Plexcitons: The Role of Oscillator Strengths and Spectral Widths in Determining Strong Coupling. *ACS Nano* **2018**, *12* (1), 402–415. https://doi.org/10.1021/acsnano.7b06589.

(76) Li, N.; Han, Z.; Huang, Y.; Liang, K.; Wang, X.; Wu, F.; Qi, X.; Shang, Y.; Yu, L.; Ding, B. Strong Plasmon–Exciton Coupling in Bimetallic Nanorings and Nanocuboids. *J Mater Chem C Mater* **2020**, *8* (23), 7672–7678. https://doi.org/10.1039/D0TC01837F.

(77) Melnikau, D.; Govyadinov, A. A.; Sánchez-Iglesias, A.; Grzelczak, M.; Nabiev, I. R.; Liz-Marzán, L. M.; Rakovich, Y. P. Double Rabi Splitting in a Strongly Coupled System of Core–Shell Au@Ag Nanorods and J-Aggregates of Multiple Fluorophores. *J Phys Chem Lett* **2019**, *10* (20), 6137–6143. https://doi.org/10.1021/acs.jpclett.9b01988.

(78) Guo, J.; Wu, F.; Song, G.; Huang, Y.; Jiao, R.; Yu, L. Diverse Axial Chiral Assemblies of J-Aggregates in Plexcitonic Nanoparticles. *Nanoscale* **2021**, *13* (37), 15812–15818. https://doi.org/10.1039/D1NR02634H.

(79) Wu, F.; Guo, J.; Huang, Y.; Liang, K.; Jin, L.; Li, J.; Deng, X.; Jiao, R.; Liu, Y.; Zhang, J.; Zhang, W.; Yu, L. Plexcitonic Optical Chirality: Strong Exciton–Plasmon Coupling in Chiral J-Aggregate-Metal Nanoparticle Complexes. *ACS Nano* **2021**, *15* (2), 2292–2300. https://doi.org/10.1021/acsnano.0c08274.

(80) Zhu, J.; Wu, F.; Han, Z.; Shang, Y.; Liu, F.; Yu, H.; Yu, L.; Li, N.; Ding, B. Strong Light-Matter Interactions in Chiral Plasmonic-Excitonic Systems Assembled on DNA Origami. *Nano Lett* **2021**, *21* (8), 3573–3580. https://doi.org/10.1021/acs.nanolett.1c00596.

(81) Govorov, A. O.; Fan, Z.; Hernandez, P.; Slocik, J. M.; Naik, R. R. Theory of Circular Dichroism of Nanomaterials Comprising Chiral Molecules and Nanocrystals: Plasmon Enhancement, Dipole Interactions, and Dielectric Effects. *Nano Lett* **2010**, *10* (4), 1374–1382. https://doi.org/10.1021/nl100010v.

(82) Feng, W.; Kim, J.-Y.; Wang, X.; Calcaterra, H. A.; Qu, Z.; Meshi, L.; Kotov, N. A. Assembly of Mesoscale Helices with Near-Unity Enantiomeric Excess and Light-Matter Interactions for Chiral Semiconductors. *Sci Adv* **2017**, *3* (3), e1601159. https://doi.org/10.1126/sciadv.1601159.

(83) Lodahl, P.; Mahmoodian, S.; Stobbe, S.; Rauschenbeutel, A.; Schneeweiss, P.; Volz, J.; Pichler, H.; Zoller, P. Chiral Quantum Optics. *Nature* **2017**, *541* (7638), 473–480. https://doi.org/10.1038/nature21037.

(84) Voronin, K.; Taradin, A. S.; Gorkunov, M. v.; Baranov, D. G. Single-Handedness Chiral Optical Cavities. *ACS Photonics Article ASAP* **2022**, 1–20. https://doi.org/10.1021/acsphotonics.2c00134.

(85) Melnikau, D.; Savateeva, D.; Gun'ko, Y. K.; Rakovich, Y. P. Strong Enhancement of Circular Dichroism in a Hybrid Material Consisting of J-Aggregates and Silver Nanoparticles. *The Journal of Physical Chemistry C* **2013**, *117* (26), 13708–13712. https://doi.org/10.1021/jp4037777.

(86) Yan, X.; Wang, Q.; Chen, X.; Jiang, Y.-B. Supramolecular Chiral Aggregates Exhibiting Nonlinear CD–Ee Dependence. *Advanced Materials* **2020**, *32* (41), 1905667. https://doi.org/https://doi.org/10.1002/adma.201905667.

(87) Palmans, A. R. A.; Meijer, E. W. Amplification of Chirality in Dynamic Supramolecular Aggregates. *Angewandte Chemie International Edition* **2007**, *46* (47), 8948–8968. https://doi.org/https://doi.org/10.1002/anie.200701285.

(88) Kirstein, S.; Daehne, S. J-Aggregates of Amphiphilic Cyanine Dyes: Self-Organization of Artificial Light Harvesting Complexes. *International Journal of Photoenergy* **2006**, *2006*, 020363. https://doi.org/10.1155/IJP/2006/20363.

(89) Wang, M.; Silva, G. L.; Armitage, B. A. DNA-Templated Formation of a Helical Cyanine Dye J-Aggregate. *J Am Chem Soc* **2000**, *122* (41), 9977–9986. https://doi.org/10.1021/ja002184n.

(90) Norden, B. Linear and Circular Dichroism of Polymeric Pseudoisocyanine. *J Phys Chem* **1977**, *81* (2), 151–159. https://doi.org/10.1021/j100517a011.

(91) Zhang, Y.; Xiang, J.; Tang, Y.; Xu, G.; Yan, W. Chiral Transformation of Achiral J-Aggregates of a Cyanine Dye Templated by Human Serum Albumin. *ChemPhysChem* **2007**, *8* (2), 224–226. https://doi.org/https://doi.org/10.1002/cphc.200600548.

(92) von Berlepsch, H.; Böttcher, C.; Dähne, L. Structure of J-Aggregates of Pseudoisocyanine Dye in Aqueous Solution. *J Phys Chem B* **2000**, *104* (37), 8792–8799. https://doi.org/10.1021/jp000085q.

(93) Berova, N.; Nakanishi, K.; Woody, R. W. *Circular Dichroism: Principles and Applications*; John Wiley & Sons, 2000.

(94) Parson, W. W. *Modern Optical Spectroscopy*; Springer: Berlin, 2007; Vol. 2.

(95) de Rossi, U.; Dähne, S.; Meskers, S. C. J.; Dekkers, H. P. J. M. Spontaneous Formation of Chirality in J-Aggregates Showing Davydov Splitting. *Angewandte Chemie International Edition in English* **1996**, *35* (7), 760–763. https://doi.org/https://doi.org/10.1002/anie.199607601.

(96) Fidder, H.; Knoester, J.; Wiersma, D. A. Observation of the One-exciton to Two-exciton Transition in a J Aggregate. *J Chem Phys* **1993**, *98* (8), 6564–6566. https://doi.org/10.1063/1.464797.

(97) Virgili, T.; Lüer, L.; Cerullo, G.; Lanzani, G.; Stagira, S.; Coles, D.; Meijer, A. J. H. M.; Lidzey, D. G. Role of Intramolecular Dynamics on Intermolecular Coupling in Cyanine Dye. *Phys Rev B* **2010**, *81* (12), 125317. https://doi.org/10.1103/PhysRevB.81.125317.

(98) Yağlioğlu, G.; Dorsinville, R.; Özçelik, S. Femtosecond Response of J Aggregates Adsorbed onto Silver Colloid Surfaces. *J Appl Phys* **2003**, *94* (5), 3143–3146. https://doi.org/10.1063/1.1597941.

(99) Sundström, V.; Gillbro, T.; Gadonas, R. A.; Piskarskas, A. Annihilation of Singlet Excitons in J Aggregates of Pseudoisocyanine (PIC) Studied by Pico- and Subpicosecond Spectroscopy. *J Chem Phys* **1988**, *89* (5), 2754–2762. https://doi.org/10.1063/1.455027.

(100) Horng, M. L.; Quitevis, E. L. Excited-State Dynamics of Polymer-Bound J-Aggregates. *Journal of Physical Chemistry* **1993**, *97* (47), 12408–12415. https://doi.org/10.1021/J100149A049/ASSET/J100149A049.FP.PNG_V03.

(101) Kobayashi, S.; Sasaki, F. Dynamical Properties of Large Coherence Length Excitons in Pic J Aggregates. *Jpn J Appl Phys* **1995**, *34* (S1), 279–281. https://doi.org/10.7567/JJAPS.34S1.279/XML.

(102) Kopainsky, B.; Kaiser, W. Ultrafast Transient Processes of Monomers, Dimers, and Aggregates of Pseudoisocyanine Chloride (PIC). *Chem Phys Lett* **1982**, *88* (4), 357–361. https://doi.org/10.1016/0009-2614(82)83025-X.

(103) del Fatti, N.; Voisin, C.; Achermann, M.; Tzortzakis, S.; Christofilos, D.; Vallée, F. Nonequilibrium Electron Dynamics in Noble Metals. *Phys Rev B* **2000**, *61* (24), 16956–16966. https://doi.org/10.1103/PhysRevB.61.16956.

(104) Zhang, X.; Huang, C.; Wang, M.; Huang, P.; He, X.; Wei, Z. Transient Localized Surface Plasmon Induced by Femtosecond Interband Excitation in Gold Nanoparticles. *Sci Rep* **2018**, *8* (1), 10499. https://doi.org/10.1038/s41598-018-28909-6.

(105) Link, S.; Burda, C.; Mohamed, M. B.; Nikoobakht, B.; El-Sayed, M. A. Femtosecond Transient-Absorption Dynamics of Colloidal Gold Nanorods: Shape Independence of the Electron-Phonon Relaxation Time. *Phys Rev B* **2000**, *61* (9), 6086–6090. https://doi.org/10.1103/PhysRevB.61.6086.

(106) Link, S.; El-Sayed, M. A. Shape and Size Dependence of Radiative, Non-Radiative and Photothermal Properties of Gold Nanocrystals. *Int Rev Phys Chem* **2000**, *19* (3), 409–453. https://doi.org/10.1080/01442350050034180.

(107) Hodak, J.; Martini, I.; Hartland, G. v. Ultrafast Study of Electron–Phonon Coupling in Colloidal Gold Particles. *Chem Phys Lett* **1998**, *284* (1–2), 135–141. https://doi.org/10.1016/S0009-2614(97)01369-9.

(108) Finkelstein-Shapiro, D.; Mante, P.-A.; Sarisozen, S.; Wittenbecher, L.; Minda, I.; Balci, S.; Pullerits, T.; Zigmantas, D. Understanding Radiative Transitions and Relaxation Pathways in Plexcitons. *Chem* **2021**, *7* (4), 1092–1107. https://doi.org/10.1016/j.chempr.2021.02.028.

(109) Botzung, T.; Hagenmüller, D.; Schütz, S.; Dubail, J.; Pupillo, G.; Schachenmayer, J. Dark State Semilocalization of Quantum Emitters in a Cavity. *Phys Rev B* **2020**, *102* (14), 144202. https://doi.org/10.1103/PhysRevB.102.144202.

(110) Wang, H.; Wang, H.; Sun, H.; Cerea, A.; Toma, A.; Angelis, F.; Jin, X.; Razzari, L.; Cojoc, D.; Catone, D.; Huang, F.; Proietti Zaccaria, R. Dynamics of Strongly Coupled Hybrid States by Transient Absorption Spectroscopy. *Adv Funct Mater* **2018**, *28* (48), 1801761. https://doi.org/10.1002/adfm.201801761.

(111) Xiang, B.; Ribeiro, R. F.; Chen, L.; Wang, J.; Du, M.; Yuen-Zhou, J.; Xiong, W. State-Selective Polariton to Dark State Relaxation Dynamics. *J Phys Chem A* **2019**, *123* (28), 5918–5927. https://doi.org/10.1021/acs.jpca.9b04601.

(112) Litinskaya, M.; Reineker, P.; Agranovich, V. M. Fast Polariton Relaxation in Strongly Coupled Organic Microcavities. *J Lumin* **2004**, *110* (4), 364–372. https://doi.org/10.1016/j.jlumin.2004.08.033.